TÉCNICO LISBOA

Characterization of heat transfer in nanofluid spray cooling of a solid heated surface

Miguel Patrik Jyllilä Sanches

Thesis to obtain the Master of Science Degree in

Mechanical Engineering

Supervisors: Prof. Ana Sofia Oliveira Henriques Moita
Prof. António Luís Nobre Moreira

Examination Committee

Chairperson: Prof. Edgar Caetano Fernandes
Supervisor: Prof. Ana Sofia Oliveira Henriques Moita
Member of the Committee: Prof. André Resende Rodrigues da Silva

January 2021

Acknowledgments

My first words go to Professor Ana Moita, who introduced me to research and, specifically, the high-tech field of sprays and droplets. Thank you for inviting me to assist to LIDESP (International Advanced Course on Liquid Interfaces, Drops and Sprays) and ICLASS (International Conference on Liquid Atomization and Spray Systems). I am also thankful for your trust in my work to be submitted for ICLASS 2021. Without your knowledge and feedback, this work would not have been possible.

I would also like to thank Professor António Moreira for integrating me in his research team, Professor Ana Paula Ribeiro for preparing and characterizing the nanofluids, Professor André Silva for the insights on numerical modelling of sprays and Professor Sandra Dias for managing the laboratory and providing answers to my questions.

Thank you to all my laboratory mates: Miguel Figueiredo, Pedro Pontes, Lourenço Martins, Ricardo Cautela and Leonardo Manetti, for introducing me to the different experimental techniques, helping me with my doubts and for your overall companionship.

My friends and colleagues also deserve a thank you note, for having accompanied me during these five years at Instituto Superior Técnico and making this journey inspiring and even more enjoyable.

Last but not least, I would like to thank my family for their endless support on the good and bad days, and my girlfriend Alexandra for her patience and love.

This would not have been possible without you all. I am grateful for having experienced this journey with you.

Abstract

The interest in spray cooling has been increasing as an efficient thermal management technique for high power load systems such as electronics. The aim of this work was to study the use of nanofluids as a way of improving thermal performance of sprays. Nanofluids were prepared using as base solution distilled water with 0.05% (m/m) cetyltrimethylammonium bromide. Nanoparticles of alumina were mixed with the base fluid at different concentrations: 0.5%, 1% and 2% (m/m). Two different silver nanofluids were also prepared, using 1% (m/m) concentration, one using spherical and the other using triangular particles. These nanofluids were sprayed using a hollow-cone atomizer, at two different heights from an AISI 304 stainless steel foil. This foil was heated by Joule effect, with two imposed currents, delivering approximately 915 and 2100 $\mathrm{W/m^2}$. Thermal footprints of the sprays were acquired using infrared thermography and dissipated heat fluxes were calculated. In steady-state, the lowest obtained temperatures at the surface occurred for the 0.5% (m/m) alumina nanofluid. Increasing alumina nanoparticle concentration resulted in the increase of radial foil temperatures. When comparing the silver nanofluids, the one with spherical particles resulted in slightly lower surface temperatures than the fluid with triangular particles. Heat transfer coefficients decreased with increasing thermal conductivity and dynamic viscosity of the nanofluids. On the other hand, it revealed a strong positive correlation with the specific heat capacity of the nanofluids. For the range of experimental conditions covered in this work, nanofluids have proven to increase the thermal performance of the spray.

Keywords: Spray cooling, Nanofluids, Heat transfer, Thermophysical properties, High-speed infrared thermography

Resumo

O interesse por arrefecimento usando *sprays* tem aumentado, como forma eficiente de dissipar calor, em sistemas com elevadas cargas térmicas. O objetivo deste trabalho foi estudar o uso de nanofluidos para aumentar o desempenho térmico dos *sprays*. As nanopartículas foram adicionadas a um fluido base composto por água destilada e 0.05% (m/m) de brometo cetiltrimetilamónio. Nanopartículas de alumina em concentrações de 0.5%, 1% e 2% (m/m) foram misturadas no fluido base. Foram também preparados dois nanofluidos de prata, a uma concentração de 1% (m/m), um deles com partículas esféricas e outro com partículas triangulares. Estes nanofluidos foram atomizados por um atomizador de cone-oco, colocado a duas alturas distintas de uma folha de aço inoxidável AISI 304. Esta folha foi aquecida por efeito de Joule, usando duas correntes impostas diferentes, resultando em 915 e $2100\ \mathrm{W/m^2}$. Uma câmara termográfica de infravermelhos foi usada para obter os mapas térmicos da folha resultantes do impacto dos *sprays* e depois calcularam-se os calores dissipados. Em regime estacionário, verificou-se que o nanofluido de 0.5% (m/m) alumina resultou num perfil de temperaturas mais baixas na superfície. Ao aumentar a concentração de alumina, as temperaturas aumentaram. Quando comparados os dois nanofluidos de prata, o de partículas esféricas apresentou, de um modo geral, temperaturas mais baixas na superfície de aço do que o de partículas triangulares. Observou-se ainda uma diminuição dos coeficientes de calor com o aumento de condutividade térmica e viscosidade dinâmica, e por outro lado, uma correlação positiva forte com o calor específico dos nanofluidos.

Palavras-chave: Arrefecimento por *spray*, Nanofluidos, Transferência de calor, Propriedades termofísicas, Termografia de infravermelhos

Contents

List of Tables

List of Figures

Nomenclature

α	Thermal diffusivity.	$[\mathrm{m}^2/\mathrm{s}]$
β	Expansion coefficient.	$[^\circ\mathrm{C}^{-1}]$
Δ	Difference.	$[-]$
δ	Thickness.	$[\mathrm{m}]$
λ_R	Roughness fundamental wavelength.	$[\mathrm{nm}]$
μ	Dynamic viscosity.	$[\mathrm{mPa.s}]$
ν	Kinematic viscosity.	$[\mathrm{m}^2/\mathrm{s}]$
$\overline{\Delta T}$	Mean foil temperature relative to initial fluid temperature.	$[^\circ\mathrm{C}]$
ϕ	Volume fraction.	$[-]$
ρ	Specific mass.	$[\mathrm{kg}/\mathrm{m}^3]$
σ	Surface tension.	$[\mathrm{mN}/\mathrm{m}]$
σ_{BC}	Covariance between variables B and C.	$[-]$
σ_{SB}	Stefan–Boltzmann constant.	$[5.6703 \times 10^{-8}\ \mathrm{kg}/(\mathrm{s}^3.^\circ\mathrm{C}^4)]$
θ	Contact angle.	$[^\circ]$
ε	Emissivity.	$[-]$
A	Area.	$[\mathrm{m}^2]$
A	Disintegration criteria constant.	$[-]$
a	Disintegration criteria constant.	$[-]$
B	Generic variable.	$[-]$
b	Deterministic constant which multiplies variable B.	$[-]$

b	Disintegration criteria constant.	[$-$]
Bi	Biot number.	[$-$]
Bo_{m}	Modified boiling number.	[$-$]
C	Generic variable.	[$-$]
c	Deterministic constant which multiplies variable C.	[$-$]
Ca	Capillary number.	[$-$]
c_p	Isobaric specific heat coefficient.	[$\mathrm{kJ/(kg.K)}$]
D	Droplet diameter.	[m]
d_{32}	Sauter Mean Diameter (SMD).	[m]
g	Gravitational acceleration.	[$9.81\ \mathrm{m/s^2}$]
h	Heat transfer coefficient.	[$\mathrm{W/(m^2.^\circ C}$]
h_{fg}	Specific enthalpy of vaporization.	[$\mathrm{J/kg}$]
h_c	Convective heat transfer coefficient.	[$\mathrm{W/(m^2.^\circ C}$]
I	Electrical current.	[A]
Ja	Jakob number.	[$-$]
K	Splashing threshold dimensionless number.	[$-$]
k	Thermal conductivity coefficient.	[$\mathrm{W/(m.K)}$]
L	Length.	[m]
La	Laplace number.	[$-$]
L^*	Adapted characteristic length.	[m]
m	Mass.	[kg]
n	Shape factor.	[$-$]
Nu	Nusselt number.	[$-$]
Oh	Ohnesorge number.	[$-$]
P	Perimeter.	[m]
p	Pressure.	[Pa]
Pr	Prandtl number.	[$-$]
Q	Heat.	[J]

Q''	Volumetric fluid flow rate per unit rate.	$[\mathrm{m}]$
q''	Heat flux.	$[\mathrm{W/m^2}]$
R	Electrical resistance.	$[\Omega]$
r	Radial coordinate.	$[\mathrm{m}]$
R_a	Surface mean roughness.	$[\mathrm{nm}]$
Ra	Rayleigh number.	$[-]$
Re	Reynolds number.	$[-]$
S	Surface area of nanoparticle.	$[\mathrm{m^2}]$
T	Temperature.	$[^\circ\mathrm{C}]$
t	Time.	$[\mathrm{s}]$
U	Droplet velocity.	$[\mathrm{m/s}]$
V	Difference of electric potential.	$[\mathrm{V}]$
W	Energy.	$[\mathrm{J}]$
w	Width.	$[\mathrm{m}]$
We	Weber number.	$[-]$
x	Cartesian coordinate.	$[\mathrm{m}]$
y	Cartesian coordinate.	$[\mathrm{m}]$
Z	Axial coordinate.	$[\mathrm{m}]$

0	Initial condition.
∞	Quiescent air.
atm	Atmosphere.
bf	Base fluid.
cond	Conduction.
conv	Convective.
diss	Dissipated.
f	Liquid.
g	Vapor.

h	Heater.
in	Input.
Joule	By Joule effect.
Leid	Leidenfrost point.
low	Lower surface.
lv	Liquid-vapor.
max	Maximum.
nf	Nanofluid.
np	Nanoparticle.
obj	Object.
rad	Radiative.
ref	Reference.
refl	Reflected.
sat	Saturation condition.
sl	Solid-liquid.
spray	To the spray droplets.
sv	Solid-vapor.
tot	Total.
up	Upper surface.
w	Wall.

*	Dimensionless.

Acronyms

ADU Analog to Digital unit. xv, 25, 27, 28, 30, 31, 79, 81

CHF critical heat flux. 4, 14

CTAB cetyltrimethylammonium bromide. xiii, 3, 34–38, 50–52, 55, 56, 63, 64

FPS frames per second. 30, 36, 75, 77–79, 82

IR infrared thermography. 25, 65

LED light emitting diode. 23, 24

PDI Phase Doppler Interferometry. xv, 32, 33

SMD Sauter Mean Diameter. xx, 14

TEM Transmission Electron Microscopy. 4, 66

Chapter 1

Introduction

1.1 Motivation

Spray cooling of solid surfaces has proven to be very efficient, with many interesting application in electronics cooling, metal production, aeronautics and space industries. Other studies have shown that introduction of some types of nanoscale particles in a base fluid to form a nanofluid, enhances the thermal performance. The objective of this dissertation is to combine both these high-tech engineering solutions and study their interaction.

The mechanisms behind spray atomization, droplet impact and the resulting heat transfer on a solid surface are very complex. The level of complexity is highly increased by the addition of nanoparticles and by the fact that the surface is wet. Contrarily to what is found in literature, where studies in this field are made with thermocouples, this project takes advantage of a high spatial and temporal resolution infrared thermography camera.

Moreover, the thermal enhancement by using nanofluids is very controversial in literature. The nanoparticles interact at molecular scale between each other, changing the dynamic and thermal properties of the fluid, which may or may not be enough to deteriorate the overall performance of the fluid. Due to the complex interactions between nanoparticles and even with the base fluid, the heat transfer mechanisms of nanofluid spray cooling remain unexplained.

1.2 Topic Overview

1.2.1 Spray cooling

The increasing use of electronic systems and power electronics will require better and more efficient cooling mechanisms. The accumulation of heat leads to higher operating temperatures which have a negative impact on the lifetime and stability of equipment.

In Table 1.1, different cooling techniques are compared in terms of heat transfer coefficient and highest obtained heat flux.

Table 1.1: Comparison of heat transfer coefficient and highest heat flux for different cooling techniques (adapted from Glassman [1]).

Mechanism	Cooling method	Heat transfer coefficient $[\mathrm{W/(cm^2K)}]$	Highest heat flux $[\mathrm{W/(cm^2)}]$	Reference
Single-phase	Free air convection	$0.0005 - 0.0025$	15	Mudawar [2], Azar [3]
Single-phase	Forced air convection	$0.001 - 0.025$	35	Mudawar [2]
Single-phase	Natural convection with water	$0.08 - 0.2$	$5 - 90$	Mudawar [2]
Two-phase	Pool boiling with porous media	3.7	140	Rainey et al. [4]
Two-phase	Spray cooling	$20 - 40$	1200	Pais et al. [5]
Two-phase	Jet impingement	28	1820	Overholt et al. [6]

Table 1.1 shows that, in general, single-phase cooling methods reach much smaller heat transfer coefficients and heat fluxes than two-phase methods. Moreover, spray cooling and jet impingement have achieved heat fluxes greater than $1000\ \mathrm{W/cm^2}$. Spray cooling is a technique which is based on the impingement of small droplets of a spray on a heated surface. This technique can be used in a single-phase or two-phase regime depending on the heat flux delivered by the surface and on the properties of the spray. On the other hand, jet impingement is an extreme situation of spray cooling where, instead of having small droplets of fluid impinging the surface, there is a continuous jet. In practical applications, selecting between one and the other has to do with the required flow rates.

Yan [7] has identified many applications for spray cooling, such as: dermatological operations, metal production and processing industry and mainly for cooling high performance electronic devices. In dermatological surgeries, cryogenic spray cooling is used to cool human skin before laser treatments. Spray cooling plays an important role in steel strip casting and optimizing the microstructure after hot rolling. In recent years the cooling of electronics has been of great interest and spray cooling systems have been developed in this area, Bar-Cohen et al. [8] and Tilton et al. [9].

The heat transfer in spray cooling is a complex combination of different heat transfer mechanisms, Pais et al. [5], Yang et al. [10] and Rini et al. [11]. This overall complex mechanism has not only to do with the heat transfer phenomena after droplet impact, but also has a strong relationship with the spray before impact, Moreira et al. [12]. Spray dynamics are dependent on atomizer type, injection pressure, type of fluid and even surrounding air velocities. These variables impact the atomization process, which is the progressive transformation of a continuous body of liquid into small droplets.

Moreover, heat transfer between the fluid and the surface is dependent on the impact of the fluid droplets. Different studies have been performed to understand the possible outcomes of a droplet impact on to a solid surface, Moita and Moreira [13], Moita [14], Moreira et al. [12] and Mundo et al. [15]. However, these studies focus mainly in individual droplet collision with a solid body, as the study of single droplets in a spray is a big experimental challenge. As explained by Moreira et al. [12], the extrapolation of these results for individual droplet impact outputs to sprays must be made carefully, as the droplet-droplet, droplet-film and other kind of interactions existing in sprays are neglected.

1.2.2 Nanofluids

The need for better cooling systems has not only resulted in the design of new cooling methods, but the use of different and more sophisticated cooling fluids has also been explored. In fact, cooling performance is a property of the overall system, which includes the cooling fluid. Given the abundance and cost of water and air, they are by far the most used cooling agents. Nevertheless, other refrigeration fluids are also found in some applications. In some cases, the thermal performance of these fluid may not be enough, thus emerged the idea of combining the properties of a base fluid and solid particles.

Nanofluids are suspensions of nanoparticles in a base fluid. These nanoparticles are typically in the range of $10-100\,\mathrm{nm}$ and are usually metallic, however different materials may be found depending on the specific application, such as: ceramics, metallic oxides or carbonic particles. The term nanofluids was introduced by Choi and Eastman [16]. Yet, the idea of scattering solid particles into liquids is not new, and may be related to as early as 1873 with the work of Maxwell. Maxwell [17] explored the properties of fluid with micrometre and millimetre level particles. However, this scale particles have limited application in heat transfer enhancement, due to settling, abrasion and clogging (Xuan and Li [18]).

Heat transfer enhancement by the use of nanofluids is an ongoing research field. The mechanisms behind heat transfer in nanofluids are very complex, resulting of liquid-particle and particle-particle interactions. Nanofluids show significant enhancement of thermal conductivity when compared to the base fluid. This has not only to do with the higher thermal conductivity of the solid particles but also with the high specific surface area of the nanoparticles (Aybar et al. [19]). Due to the different interactions inside the nanofluid, many different models have been established to estimate the thermal conductivity of nanofluids. Aybar et al. [19] has listed the models and describes which the conditions of applicability for each one.

In the past two decades the research work in nanoscale science has increased substantially. However, these studies are not consensual. Some have presented increases of heat transfer coefficients of more than 30% for alumina (Al_2O_3) under forced convection (Heris et al. [20]) and deterioration for Al_2O_3 under natural convection (Putra et al. [21]). A field of extensive research using nanofluids is pool boiling (Taylor and Phelan [22]). Research in this area has also revealed great disagreement but, as explained by Taylor and Phelan [22] in their review, this is to be expected given the large dependence on the test conditions.

One of the sources of changes in testing conditions is the selection of the surfactant. Due to the natural tendency of aggregation of the nanoparticles, a surfactant is added to the base fluid, with the objective of reducing surface tension, resulting in a homogeneous emulsion. These surfactants usually reduce the thermal conductivity, thus having the contrary effect of nanoparticles. However, surfactants are important to maintain the stability of nanofluids and Al-Waeli et al. [23] have achieved a maximum 93 day stability window of nano-silicon carbide nanofluids, with the addition of cetyltrimethylammonium bromide (CTAB).

Sekhar et al. [24] studied the heat transfer enhancement with alumina nanofluids, for concentrations of 0.02, 0.1 and 0.5% (m/m), in a pipe under low Reynolds number. The results showed an $8-12$% increase in the heat transfer coefficient for the nanofluids when compared to water. Moreover, the

Nusselt number and friction factor increased with the increase of particle concentration.

Apart from the inconsistent results of literature, under certain conditions, nanofluids will play a vital role in next generation engineering and medical equipment (Devendiran and Amirtham [25]). These applications cover different areas such as: automobile, solar energy, magnetic sealing and electronics cooling. However, these applications will only be greatly accepted once the following issues and challenges have been overcome (Saidur et al. [26]):

- The disagreement between experimental data and theoretical estimations;
- Poor characterization of nanofluid properties;
- Lack of explanations for some behaviors of nanofluids.
- Stability of the nanofluids.

1.2.3 Nanofluid spray cooling

Spray cooling, as mentioned earlier, is a very effective way to remove high amounts of heat from hot surfaces with a low surface super-heat and low mass flux. The enhancement for larger heat removals comes with higher convective heat transfer coefficients and it is currently a challenge in many industrial applications. The demands on heat dissipation are increasing and so strategies have been adopted in order to achieve these results – this includes surface modification to enhance these processes and/or the use of nanofluids to reach the same goal (Mudawar [2]).

Available results indicate that nanofluids made from metal particles and water can improve heat transfer by up to 40%. Chen et al. [27] experiment resulted in a 250% improvement for multiwalled carbon nanotubes (with a mean diameter and length of $25\ \mathrm{nm}$ and $50\ \mathrm{nm}$, respectively).

Hsieh et al. [28] studied the performance of silver and carbon nanotubes in sprays of deionized water nanofluids. These researchers obtained an 2.4 enhancement ratio of critical heat flux (CHF) for the 0.0075% (V/V) silver nanofluid when compared to plain water. Moreover, this result was obtained with a very low mass flux of only $11.9 \times 10^{-4}\ \mathrm{kg/(cm^2 s)}$. According to them, the heat transfer enhancement is attributed to increased mixing rater than higher thermal conductivity. In addition, given the higher thermal conductivity of the carbon nanotubes when compared to silver, the authors were expecting that the nanofluids with nanotubes would have higher thermal performance. This was not verified and a possible reason could have been the lack of homogeneity in the emulsions.

Ravikumar et al. [29] used an air-atomizer to spray a water with 0.1% (V/V) Alumina nanofluid to cool a pre-heated steel specimen. The initial temperature of the plate was registered as $900\ ^\circ\mathrm{C}$. Their study showed a significant enhancement of critical heat flux (CHF) (of the order of 21.5%) and of the heat transfer coefficients with the addition of nanoparticles. The authors attributed this enhancements to the deposition of nanoparticles on the heated surface, by performing Transmission Electron Microscopy (TEM) imaging, and increase in thermal conductivity. Finally, they concluded that the results obtained in the study are consistent with the requirements of cooling a hot strip mill in steel industry.

The majority of nanofluid spray cooling studies have been performed using thermocouples placed at different radial distances from the spray axis. However, due to complexity of the physical phenomena taking place during spray cooling, this discrete data collection adopted in these experiments is very limited and may be one of the reasons for the disagreement observed when comparing data reported in the literature.

1.3 Objectives

The main objective of this work is to determine the potential enhancement of using nanofluids in spray cooling and identify the most relevant parameters. To do so, spray cooling of a solid heated surface was studied using different nanofluids, by changing particle material, concentration and shape. Furthermore, the cooling performance of the fluids was compared for different working conditions, in terms of height of the atomizer relative to the surface and imposed heat flux. The spray impingement was evaluated using a high temporal and spatial resolution thermographic camera to acquire the thermal footprints of the different sprays on the heated surface, as well as a laterally placed high-speed camera that allowed to characterize the dynamics of the spray droplets.

With the data obtained from the thermal images, radial temperature profiles were determined, dissipated heat fluxes were calculated and the thermal performance of the different fluids was compared using the heat transfer coefficient. Thermal maps were also used to understand the mechanisms responsible for the observed differences. Moreover, these results were related with the thermophysical properties of the fluids.

1.4 Thesis Outline

This dissertation is divided into five chapters: this Introduction, Background, Implementation, Results and Conclusions. In this first chapter the motivation, contextualization and objectives of this work are presented. Then, in the Background chapter, the current state of the art is explored and the theoretical background required to understand the underlying phenomena of spray cooling are introduced. In Chapter 3 the experimental setup and procedures applied to answer the objectives of this work are presented. Details on material and fluid selection are also given. Chapter 4 is where the results are presented, discussed and related with the data reported in literature. Finally, the main conclusions of this dissertation and suggestions for future work are made in Chapter 5. At the end of this dissertation four Appendixes can be found: Appendix A about high-speed camera setup and recording procedures, Appendix B about thermographic camera setup and recording procedures, Appendix C about the MATLAB code used to process the thermographic videos and Appendix D about the preparation of the study surface.

Chapter 2

Background

2.1 Spray atomization and propagation

A spray is a dynamic mass of fine liquid droplets. The process of transformation of a continuous body of liquid into successively smaller droplets is called spray atomization, Figure 2.1.

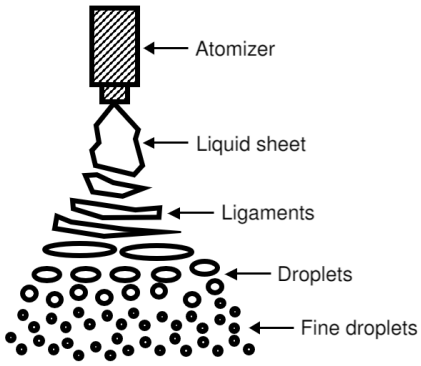

Figure 2.1: Spray atomization process (adapted from Sankaralingam et al. [30]).

As suggested by Figure 2.1, atomization is a progressive transformation of a liquid sheet into successively smaller bodies of fluid. Due to hydrodynamic internal forces, instabilities are generated in this sheet. These perturbations grow due to aerodynamic forces and the sheet breaks up into ligaments (first break-up moment). Due to the difference of velocities between the liquid and the surrounding air, the ligaments further divide into droplets (second break-up moment), Bertola [31].

Atomizers can be classified in terms of their energy source in four groups: centrifuge, pressure, kinetic and sonic.

2.2 Droplet impact on a surface

The impact of the spray droplets is a complex physical process which can result in different outcomes, depending on the properties of the liquid, surface and dynamics of the droplet. Several studies have been made to understand the interaction between a single droplet and a surface. However, one must

be careful when extrapolating these results to sprays, due to neglection of droplet-droplet interactions (Moreira et al. [12]).

2.2.1 Wettability

Wettability is a thermodynamic property of a solid-liquid-vapor system. It quantifies how well a liquid spreads over a surface. It is an important parameter when studying the impact of droplets on surfaces. At equilibrium, the balance of the interfacial tensions at the boundaries between solid-liquid σ_{sl}, solid-vapor σ_{sv} and liquid-vapor σ_{lv}, is given by the Young's equation:

$$\sigma_{\mathrm{lv}} \cos\theta + \sigma_{\mathrm{sl}} = \sigma_{\mathrm{sv}} \tag{2.1}$$

Where θ is the static contact angle, defined as in Figure 2.2. The contact angle can be seen as a ratio between adhesive and cohesive forces and is therefore used to quantify wettability. As the contact angle decreases, wettability increases. The contact angle depends on the properties of the liquid and surface. The contact angle depends on the surface chemistry and topography Moreira et al. [12]. However, details on this topic will not be advanced as the surface used in the present surface is smooth.

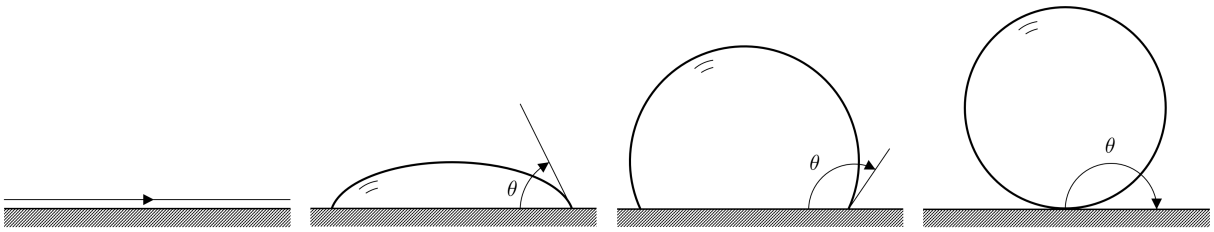

(a) Complete wetting, $\theta = 0°$. (b) Partial wetting, $0° < \theta < 90°$. (c) Partial non-wetting, $90° < \theta < 180°$. (d) Non-wetting, $\theta = 180°$.

Figure 2.2: Wetting and static contact angle θ (adapted from Moita [14]).

2.2.2 Droplet impact outcomes

Extensive experimental work has been performed to understand the possible outcomes from a droplet impact on a surface, Moreira et al. [12], Moita [14], Naber and Farrell [32]. The behavior of the droplet after impact is different when the surface is dry or wet. It has also a complex dependence on droplet size, velocity, impact angle and surface topography, Moita and Moreira [13], Rioboo et al. [33].

Droplet impact on a dry surface

When a droplet impacts on a dry surface it can:

- Deposit and spread, Figure 2.3;

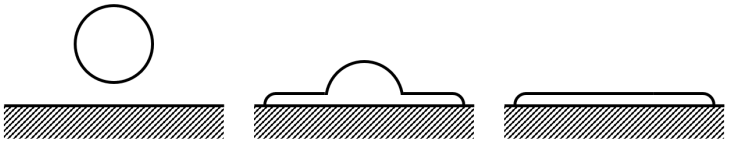

Figure 2.3: Droplet deposition and spread mechanism, Mundo et al. [15].

- Disintegrate into numerous smaller droplets. Moita and Moreira [13], Rioboo et al. [33] identified five disintegration mechanisms and studied the effect of various parameters on each one of them, as summarized in Table 2.1.

Table 2.1: Disintegration mechanisms and effect of various parameters. ↑ means an increase and ↓ is a decrease (Moreira et al. [12]).

Increase of...	Disintegration mechanisms				
	Prompt splash (Figure 2.4)	Corona splash (Figure 2.5)	Receding breakup (Figure 2.6)	Finger breakup (Figure 2.7)	Partial rebound (Figure 2.8)
U	↑	↑	↑	↑	↑
D	↑				
σ	↓	↓	↑		↑
μ	↓	↓	↓	↓	
R_a	↑	↓		↑	↓
λ_R	↓	↓			
θ		↓	↑	↓	↑

Where U is the droplet velocity, D is the droplet diameter, σ is surface tension, μ is dynamic viscosity, R_a is the surface mean roughness, λ_R is the roughness fundamental wavelength and θ is the equilibrium contact angle.

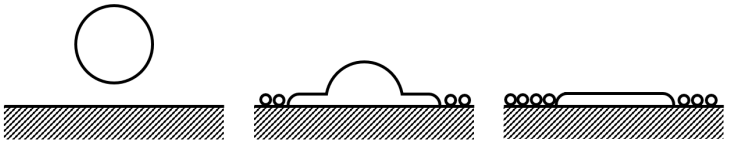

Figure 2.4: Prompt splash disintegration mechanism.

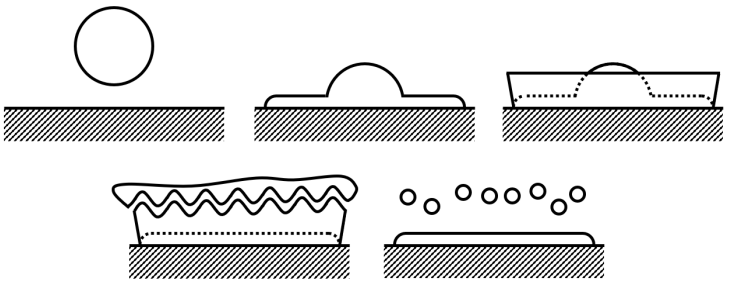

Figure 2.5: Corona splash disintegration mechanism, Mundo et al. [15].

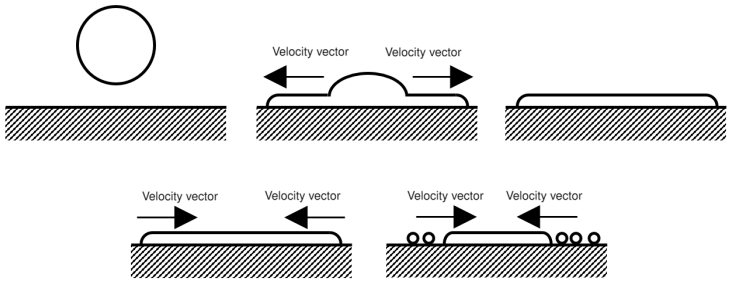

Figure 2.6: Receding breakup mechanism.

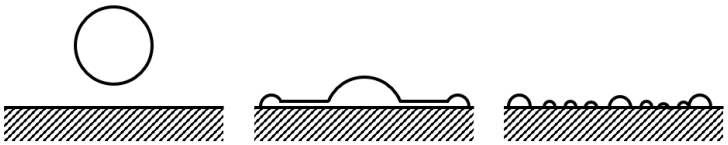

Figure 2.7: Finger breakup mechanism.

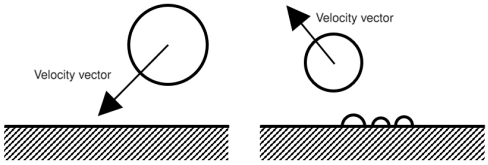

Figure 2.8: Partial rebound disintegration mechanism.

- Completely rebound, Figure 2.9.

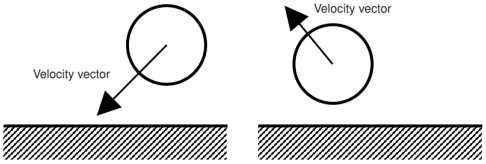

Figure 2.9: Droplet complete rebound after impact with surface.

Moreira et al. [12] summarizes disintegration criteria developed by Mundo et al. [15], Stow and Hadfield [34], Wu [35], Bai and Gosman [36] and Gavaises et al. [37], Randy et al. [38]. These criteria define the threshold for disintegration and are based on the dimensionless numbers presented in Table 2.2.

Table 2.2: Most common dimensionless numbers used in droplet-surface interactions.

Dimensionless number	Meaning	Formula	Relations	
Reynolds, Re	Inertial *vs.* viscous forces	$\frac{\rho DU}{\mu}$	$Re = \frac{\sqrt{We}}{Oh}$	$Re = CaLa$
Weber, We	Inertial *vs.* surface tension forces	$\frac{\rho DU^2}{\sigma}$	$We = Oh^2Re^2$	$We = Ca^2La$
Ohnesorge, Oh	Viscous *vs.* surface tension forces	$\frac{\mu}{\sqrt{\rho\sigma D}}$	$Oh = \frac{\sqrt{We}}{Re}$	$Oh = \frac{1}{\sqrt{La}}$
Laplace, La	Dimensionless diameter	$\frac{\rho\sigma D}{\mu^2}$	$La = \frac{We}{Ca^2}$	$La = \frac{Re}{Ca}$
Capillary, Ca	Dimensionless velocity	$\frac{\mu U}{\sigma}$	$Ca = \sqrt{\frac{We}{La}}$	$Ca = \frac{Re}{La}$

Where ρ is the density of the fluid, D is the droplet diameter, U is the droplet velocity, σ is surface tension and μ is dynamic viscosity.

These disintegration criteria are of the following general form:

$$K = AOh^a We^b \tag{2.2}$$

Where K is the splashing threshold dimensionless number, A, a and b are constants, which vary depending on the impact conditions, Table 2.3.

Table 2.3: Disintegration criteria for droplet impact onto dry surface (adapted from Moreira et al. [12]).

Reference	A	a	b	Condition
Stow and Hadfield [34]	1	-0.37	1	Surfaces with different roughness
Wu [35]	1	0	1	Surfaces with different roughness
Bai and Gosman [36]	Depends on surface roughness	0.36	0	–
Gavaises et al. [37]	1	0	1	–
Randy et al. [38]	1	0.4	-0.3	Smooth surface

Droplet impact on wet surface

When the surface is wet, the impact phenomena are much more complex, as different disintegration mechanisms arise, Moreira et al. [12]. Roisman et al. [39] identified six possible outcomes of droplet impact onto a wetted surface:

- Deposition and coalescence with the film;
- Droplet forms a crater on the liquid film;
- Corona splash;
- Splashing crown destruction by film fluctuations;
- Uprising central jet breakup;
- Film jet with breakup.

The empirical correlations for wet and non-heated surface impact are of the following form:

$$K = Re^a We^{0.8} \tag{2.3}$$

Where a is a constant.

Table 2.4 summarizes the criteria found in literature for droplet impact on a wetted surface, in terms of constant a and value of K from Equation 2.3, Ribeiro et al. [40].

Table 2.4: Disintegration criteria for droplet impact onto a wet surface (adapted from Ribeiro et al. [40]).

Reference	a	K
Bai and Gosman [36]	0.3584	1136.7
Wal et al. [41]	0.272	756.7

2.3 Heat transfer mechanism of spray cooling

Heat transfer in spray cooling is a complex combination of different heat transfer mechanisms. Pais et al. [5], Yang et al. [10], Rini et al. [11], Mesler and Mailen [42] identified four heat transfer mechanisms in spray cooling:

- Evaporation of surface of the liquid film;
- Forced convection from droplet impinging on the liquid film;
- Surface nucleation;
- Secondary nucleation.

A fifth mechanism was considered by Zhao et al. [43], which is environment heat transfer by convection and radiation.

Spray cooling can occur in two different regimes: single-phase regime or two-phase regime. The relationship between the temperature of the heated surface T_{w}, and the saturation temperature of the fluid T_{sat}, determine in which regime the system is operating:

- Single-phase regime, $T_{\mathrm{w}} < T_{\mathrm{sat}}$;
- Two-phase regime, $T_{\mathrm{w}} \geq T_{\mathrm{sat}}$.

Figure 2.10 shows the heat flux in a spray cooling system as a function of the wall temperature, T_{w}. This is actually the equivalent of the boiling curve, for a spray.

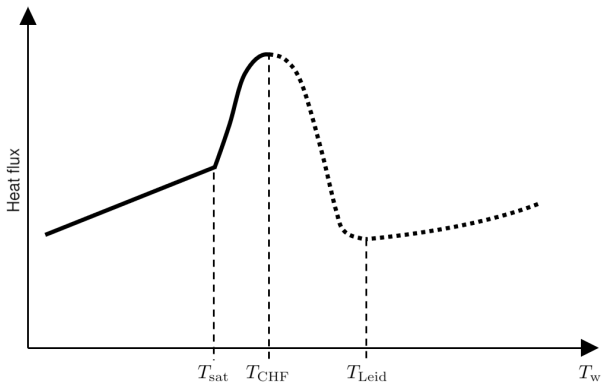

Figure 2.10: Heat flux in spray cooling as a function of wall temperature. Where T_{w} is the wall temperature, T_{sat} is the saturation temperature of the liquid, T_{CHF} is the critical heat flux temperature and T_{Leid} is the Leidenfrost temperature.

The observed heat flux variations, for temperatures higher than saturation, define four heat transfer sub-regimes in the two-phase regime:

- Nucleate boiling, $T_{\mathrm{sat}} \leq T_{\mathrm{w}} < T_{\mathrm{CHF}}$;
- Critical heat flux (CHF), $T_{\mathrm{w}} = T_{\mathrm{CHF}}$;
- Transition boiling, $T_{\mathrm{CHF}} < T_{\mathrm{w}} < T_{\mathrm{Leid}}$;

- Film boiling, $T_{\mathrm{Leid}} \leq T_{\mathrm{w}}$.

The thermal behavior of a cooling system may be evaluated in different ways. One possible way is calculating the heat transfer coefficient h, Equation 2.4, for which higher values correspond to higher thermal performance.

$$h = \frac{q''_{\mathrm{diss}}}{\Delta T} \tag{2.4}$$

Where q''_{diss} is the dissipated heat flux from the solid to the cooling fluid, T_{w} is the wall temperature, T_{f} is the fluid temperature and $\Delta T = T_{\mathrm{w}} - T_{\mathrm{f}}$.

Single-phase regime

The linear part of the curve corresponds to the single-phase regime. It occurs for wall temperatures bellow saturation ($T_{\mathrm{w}} < T_{\mathrm{sat}}$). Heat transfer in this regime is dominated by forced convection in the liquid film.

Cheng et al. [44] suggest the following heat transfer correlation in single-phase regime for pure water and single-nozzle:

$$Nu = 0.036 Re^{1.04} We^{0.28} Pr^{0.51} \left[3.02 + (T^*)^{1.53}\right] \tag{2.5}$$

Where Nu is the Nusselt number (ratio between heat transferred by convection and heat transferred by conduction), Pr is the Prandtl number and $T^* = \frac{T_{\mathrm{w}} - T_{\mathrm{f}}}{T_{\mathrm{sat}}}$ is the dimensionless temperature (T_{f} is the liquid temperature). Equation 2.5 is valid for $2.1 \leq Pr \leq 6.8$.

Nucleate boiling

Nucleate boiling is the first of the two-phase regimes. Heat flux increases rapidly with the wall temperature. Latent heat is absorbed in the generation of boiling bubbles and evaporation of the liquid. The originated bubbles move in the liquid film due to buoyancy, which mix the liquid, enhancing the heat transfer by convection.

The bubble nucleation can be divided into two types, depending on the site:

- Surface nucleation, Figure 2.11 – the nucleation centers appear on the heating surface;

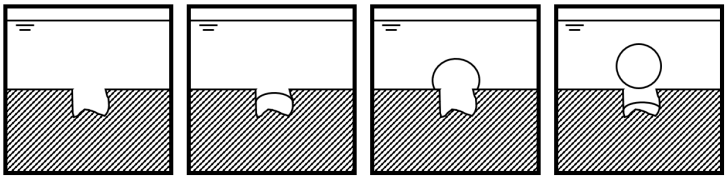

Figure 2.11: Surface nucleation bubble formation (adapted from Cheng et al. [45]).

- Secondary nucleation, Figure 2.12 – the nucleation centers appear on droplet surface.

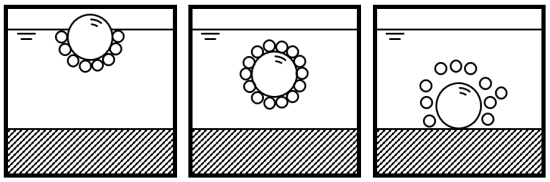

Figure 2.12: Secondary nucleation bubble formation (adapted from Cheng et al. [45]).

Hsieh et al. [46, 47] suggests, for pure water, the following heat transfer correlation of spray cooling in two-phase regime:

$$Bo_{\mathrm{m}} = 15.6We^{0.59}Ja^{1.68} \tag{2.6}$$

Where $Bo_{\mathrm{m}} = (q''_{\mathrm{diss}}Z)/(\mu_{\mathrm{f}}h_{\mathrm{fg}})$ is the modified boiling number, Z is the distance from the nozzle to the surface, μ_{f} is the fluid dynamic viscosity, h_{fg} is the specific enthalpy of vaporization of the fluid and Ja is the Jakob number.

Critical heat flux

The peak of the boiling curve, Figure 2.10, is the critical heat flux (CHF). Lin and Ponnappan [48] have obtained CHF values for different fluids: $90\ \mathrm{W/cm^2}$ with FC-87/FC-72, $490\ \mathrm{W/cm^2}$ with methanol and $500\ \mathrm{W/cm^2}$ with pure water. Pais et al. [5] achieved the highest CHF: $1200\ \mathrm{W/cm^2}$ in the laboratory with an air-water atomizing nozzle and ultra-smooth surface. Although water has achieved higher CHF, due to its high electrical conductivity, fluids such as FC-72 and FC-87 are preferred in cooling of electronic devices.

Visaria and Mudawar [49, 50] have proposed the following correlation to predict CHF:

$$\frac{q''_{\mathrm{CHF}}}{\rho_{\mathrm{g}}h_{\mathrm{fg}}Q''} = 2.3\left(\frac{\rho_{\mathrm{f}}}{\rho_{\mathrm{g}}}\right)^{0.3}\left(\frac{\rho_{\mathrm{f}}Q''^2d_{32}}{\sigma}\right)^{-0.35}\left(1+0.0019\frac{\rho_{\mathrm{f}}c_p\Delta T_{\mathrm{sub}}}{\rho_{\mathrm{g}}h_{\mathrm{fg}}}\right) \tag{2.7}$$

Where q''_{CHF} is CHF, Q'' is the volumetric fluid flow rate per unit area, ρ_{f} and ρ_{g} are the densities of the liquid and vapor phases, respectively, d_{32} is the Sauter Mean Diameter (SMD), σ is surface tension, c_p is the isobaric specific heat capacity of the fluid and $\Delta T_{\mathrm{sub}} = T_{\mathrm{sat}} - T_{\mathrm{in}}$ is in degrees of subcooling.

Transition and film boiling

After CHF, a vapor film starts to cover the surface and acts as an insulator (due to low thermal conductivity of the vapor relative to that of the liquid). This reduces drastically the heat flux, Figure 2.10. As the temperature of the surface increases, the amount of vapor covering the surface also increases. Once the surface is completely covered by the vapor film ($T_{\mathrm{w}} = T_{\mathrm{Leid}}$, where T_{Leid} is the Leidenfrost temperature), the film boiling regime starts. The heat transfer rates in the film boiling region are very low and the slight increase in heat transfer rate is given by radiation.

Both transition and film boiling are unstable regimes, which is why they are avoided in practice.

2.4 Nanofluids

Nanofluids are suspensions of solid nanoparticles (particles of sizes typically in the range of $10 - 100\ \mathrm{nm}$) in a base fluid. The interest for nanofluids has been increasing as a way of increasing thermal performance of the base fluids. Nanoparticles are usually of metallic materials, however other types are also used, such as: nonmetallic oxides, carbide, carbonic, or even combinations of different nanoparticles. Different nanofluids can also be prepared by changing particle shape, concentration or the base fluid.

2.4.1 Nanofluid preparation

There are two main methods of preparing nanofluids as explained by Babita et al. [51]:

- One-step preparation method – Combines the production of nanoparticles with the synthesis of nanofluids. Some preparation techniques are: physical vapor deposition (PVD), vacuum evaporation onto a running oil substrate (VEROS), direct evaporation condensation, submerged arc nanoparticle synthesis system (SANSS);
- Two-step preparation method – Nanoparticles are first prepared in a form of dry powder and are then dissolved into a base fluid. The nanoparticles are then dispersed with the help of a magnetic stirrer, homogenizer or ultrasonic devices. This method is not suitable for metallic nanoparticles and works very well with oxide nanoparticles.

Nanoparticles have attraction forces between each other, which naturally cause agglomerations. These clusters of nanoparticles are not desirable and may even cause clogging of the cooling systems. For this reason, usually the base fluid where the nanoparticles are mixed contains a surfactant. Surfactants lower the surface tension of the fluid, which disperses the mixture and promotes homogeneity.

2.4.2 Nanofluid properties

Properties of the nanofluids are a combination of the base fluid properties and of the properties of the nanoparticles. Properties of the nanofluids are not only a function of the particle material, but also of their shape and concentration. Correlations for thermophysical properties of nanofluids are usually given using volume fraction of nanoparticles, ϕ_{np}:

$$\phi_{\mathrm{np}} = \frac{\frac{m_{\mathrm{np}}}{\rho_{\mathrm{np}}}}{\frac{m_{\mathrm{np}}}{\rho_{\mathrm{np}}} + \frac{m_{\mathrm{bf}}}{\rho_{\mathrm{bf}}}} \tag{2.8}$$

Where m_{np} and ρ_{np} are the mass and specific mass of nanoparticles, respectively, and m_{bf} and ρ_{bf} are the mass and specific mass of base fluid, respectively.

The expressions to calculate nanofluid specific mass ρ_{nf} and specific heat capacity $c_{p,\mathrm{nf}}$ are the following, according to Sharma et al. [52]:

$$\rho_{\mathrm{nf}} = \phi_{\mathrm{np}}\rho_{\mathrm{np}} + (1 - \phi_{\mathrm{np}})\rho_{\mathrm{bf}} \tag{2.9}$$

$$c_{p,\mathrm{nf}} = \frac{\phi_{\mathrm{np}}(\rho c_p)_{\mathrm{np}} + (1-\phi_{\mathrm{np}})(\rho c_p)_{\mathrm{bf}}}{\rho_{\mathrm{nf}}} \tag{2.10}$$

Aybar et al. [19] have compiled the different models which have been developed to calculate thermal conductivity of nanofluids k_{nf}. According to Wasp [53], the thermal conductivity of a nanofluid of spherical nanoparticles is given by:

$$k_{\mathrm{nf}} = k_{\mathrm{bf}} \frac{2k_{\mathrm{bf}} + k_{\mathrm{np}} + 2\phi_{\mathrm{np}}(k_{\mathrm{np}} - k_{\mathrm{bf}})}{2k_{\mathrm{bf}} + k_{\mathrm{np}} - \phi_{\mathrm{np}}(k_{\mathrm{np}} - k_{\mathrm{bf}})} \tag{2.11}$$

For non-spherical nanoparticles, Hamilton and Crosser [54] have found the following correlation for nanofluid conductivity:

$$k_{\mathrm{nf}} = k_{\mathrm{bf}} \frac{k_{\mathrm{np}} + (n-1)k_{\mathrm{bf}} - (n-1)\phi_{\mathrm{np}}(k_{\mathrm{bf}} - k_{\mathrm{np}})}{k_{\mathrm{np}} + (n-1)k_{\mathrm{bf}} + \phi_{\mathrm{np}}(k_{\mathrm{bf}} - k_{\mathrm{np}})} \tag{2.12}$$

Where n is an empirical shape factor related to the particle sphericity. Qi et al. [55] describes shape factor of a nanoparticle as the ratio of the surface area of the nanoparticle S to that of an equivalent spherical nanoparticle with the same volume S', thus $n = S/S'$.

2.4.3 Nanofluids in spray cooling

Nanofluids have proven to enhance heat transfer by:

- Conduction, due to their resulting higher thermal conductivity;
- Convection, as nanoparticles break the hydrodynamic and thermal boundary layers.

Nanofluid spray cooling with boiling can cause the build-up of a thin porous layer of nanoparticles on the heater's surface, which may significantly improve the surface wettability, thus resulting in an increased heat flux, Chen et al. [27].

Chapter 3

Implementation

3.1 Introduction

In this Chapter the experimental setup, as well as, main methods and techniques applied in this work are presented. Furthermore, the study system is characterized in terms of conservation equations and the thermal equilibrium with quiescent air is determined experimentally and compared with some well established correlations reported in the literature.

The data analysis and processing procedures are explained in great detail, including an uncertainty analysis. Finally, the fluid selection is discussed and main thermophysical properties of these fluids are presented.

The methods presented in this Chapter are complemented by four Appendixes: Appendix A for the setup and recording procedures of the high-speed camera; Appendix B for the setup and recording procedures of the thermographic camera; Appendix C which presents the MATLAB routines used to process the data obtained with the thermographic camera; and Appendix D which shows the preparation of the study surface.

3.2 Solid surface selection and characterization

3.2.1 Material selection

In the selection of the study surface material many restrictions were considered, such as:

- Should be stable with liquids and air, to maintain its thermophysical properties constant throughout the experiments;
- Should have high electrical resistivity, as it was going to be heated by Joule effect;
- Should have low thermal expansion coefficient, to avoid wrinkles as much as possible;
- Should have well characterized thermophysical properties in literature.

Keeping these restrictions in mind and considering that the IN+ laboratory had already great experience with this material, AISI 304 stainless steel was selected. This metal was available as a very thin foil (thickness of $20\ \mu\mathrm{m}$), which allowed for convenient handling and preparation. The preparation procedure of the foil is explained in detail in Appendix D.

3.2.2 Metal sheet properties

The surface used in the present study was cut from an $20\ \mu\mathrm{m}$ AISI 304 stainless steel foil in the dimensions presented in Table 3.1.

Table 3.1: Metal foil dimensions.

Property	Value	Unit
Width, w	0.06	m
Length, L	0.09	m
Thickness, δ	20×10^{-6}	m

Figueiredo [56] and Pontes [57] have previously shown that the foil is smooth, using a profilometer with $20\ \mathrm{nm}$ resolution. For this work, density ρ_h and specific heat capacity $c_{p,\mathrm{h}}$ of AISI 304 stainless steel are assumed constant with temperature and these values are presented in Table 3.2.

Table 3.2: AISI 304 stainless steel properties (Figueiredo [56], Pontes [57]).

Property	Value	Unit
Density, ρ_h	7880	$\mathrm{kg/m^3}$
Specific heat capacity, $c_{p,\mathrm{h}}$	477	$\mathrm{J/(kg.K)}$

As will be presented later in this document, the temperature range to which the foil will be exposed is very high ($T_\mathrm{w} \in [20, 142]\ ^\circ\mathrm{C}$). Thermal conductivity k_h and electrical resistance R are strongly temperature related. In Table 3.3 the thermal conductivity of the stainless steel is presented for different temperatures.

Table 3.3: AISI 304 stainless steel thermal conductivity for different temperatures (Ho and Chu [58]).

Temperature, T_w [$^\circ\mathrm{C}$]	Thermal conductivity, k_h [$\mathrm{W/(m.K)}$]
0	14.39
20	14.76
27	14.89
77	15.79
127	16.61
227	18.28

The data from Table 3.3 is used to find the following linear fitting of the thermal conductivity k_{h} in $\mathrm{W/(m.K)}$ (with a coefficient of determination $\mathrm{R}^2 = 0.9996$):

$$k_{\mathrm{h}} = 0.0171 \times T_{\mathrm{w}} + 14.425 \tag{3.1}$$

T_{w} is the foil temperature in $^{\circ}\mathrm{C}$.

Similarly, from the currents and voltages presented in Table 3.4, one can determine the following linear fitting of the electrical resistance, R in Ω (with a coefficient of determination $\mathrm{R}^2 = 0.9822$):

$$R = 2 \times 10^{-5} \times T_{\mathrm{w}} + 0.0477 \tag{3.2}$$

The relations found in Equations 3.1 and 3.2 will be used to compute heat fluxes. The details of these calculations can be found in Section 3.4.1.

3.2.3 Characterization of the thermodynamic system

Figure 3.1 shows the control volume of the system which will be considered in this analysis, as well as, the heat exchanges through the system boundary. The system is defined with the boundary on the surface of the metallic foil.

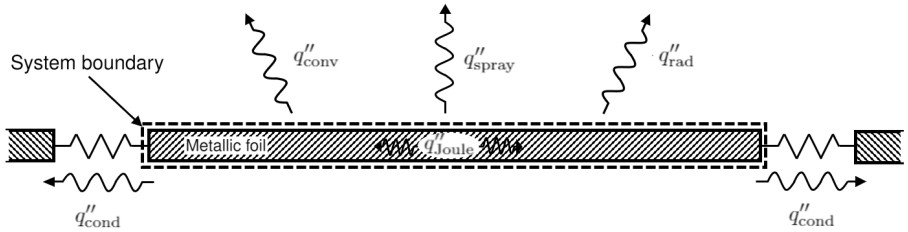

Figure 3.1: Thermodynamic system and heat exchanges with the exterior. Where q''_{cond} is heat exchanged by conduction with surrounding parts, q''_{conv} is heat exchanged by convection with quiescent air, q''_{spray} is heat exchanged with the spray and q''_{rad} is heat exchanged by radiation.

Mass balance

The control volume, as considered in Figure 3.1, is closed, thus doesn't exchange mass with the exterior.

Energy balance

The steady-state energy balance to the system has five terms:

- Heat generated in the system by Joule effect, q''_{Joule}, obtained from Equation 3.3:

$$q''_{\mathrm{Joule}} = R \times I^2 \tag{3.3}$$

  Where R is the electrical resistance and I is the imposed electrical current.

- Heat exchanged between the foil and the spray fluid, q''_{spray};

- Heat exchanged by conduction with the surrounding parts, q''_{cond};
- Heat exchanged by convection with air, q''_{conv};
- Heat exchanged by radiation, q''_{rad}.

Mathematically, the steady-state energy balance of the system can be written as:

$$q''_{\mathrm{Joule}} = q''_{\mathrm{spray}} + q''_{\mathrm{cond}} + q''_{\mathrm{conv}} + q''_{\mathrm{rad}} \tag{3.4}$$

3.2.4 Convection with air: thermal equilibrium

In this Section, a theoretical estimation of the thermal equilibrium with air is performed using some well-known correlations and these results are then compared to experimental measurements. The terms to be estimated are: convection with air and radiation. Conduction is neglected as the contact area is small and well insulated.

Estimation of the convection term

For the convection term, correlations suggested by McAdams [59] for horizontal heated plates are used, with the adapted characteristic length L^*, based on Goldstein et al. [60], Lloyd and Moran [61]:

$$L^* \equiv \frac{A_{\mathrm{w}}}{P} \tag{3.5}$$

Where A_{w} and P are the plate surface area and perimeter, respectively. In the present case, $A_{\mathrm{w}} = 0.0054\ \mathrm{m}^2$ and $P = 0.3\ \mathrm{m}$, which result in $L^* = 0.018\ \mathrm{m}$. The suggested average Nusselt number correlations $\overline{Nu}_{L^*}$ are, for the upper surface of the hot plate:

$$\overline{Nu}_{L^*} = \begin{cases} 0.54{Ra_{L^*}}^{1/4} \text{ (valid for } 10^4 \leq Ra_{L^*} \leq 10^7\text{)} \\ 0.15{Ra_{L^*}}^{1/3} \text{ (valid for } 10^7 \leq Ra_{L^*} \leq 10^{11}\text{)} \end{cases} \tag{3.6}$$

And for the lower surface of the hot plate:

$$\overline{Nu}_{L^*} = 0.27{Ra_{L^*}}^{1/4} \text{ (valid for } 10^5 \leq Ra_{L^*} \leq 10^{10}\text{)} \tag{3.7}$$

With the Rayleigh number based on the characteristic length, Ra_{L^*}:

$$Ra_{L^*} = \frac{g\beta(T_{\mathrm{w}} - T_\infty){L^*}^3}{\nu\alpha} \tag{3.8}$$

Where g is the gravitational acceleration, β is the expansion coefficient of air, T_{w} is the surface temperature, T_∞ is the quiescent air temperature, ν is the kinematic viscosity of air and α is the thermal diffusivity of air. All air properties are evaluated at $T_{\mathrm{f}} = \frac{T_{\mathrm{w}}+T_\infty}{2}$.

In Figure 3.2, the Nusselt and Rayleigh numbers are presented, for a quiescent air temperature, $T_\infty = 26\ ^\circ\mathrm{C}$ and wall temperatures in the range, $T_{\mathrm{w}} \in [26, 150]\ ^\circ\mathrm{C}$.

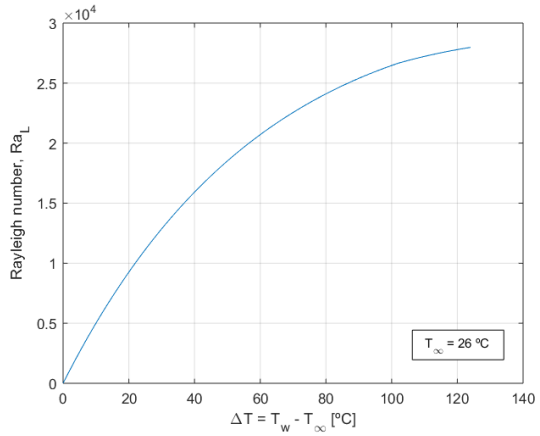

(a) Rayleigh number, Ra_L.

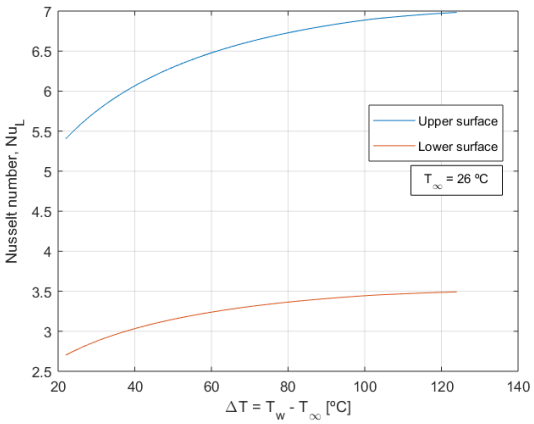

(b) Nusselt number, $\overline{Nu}_L$.

Figure 3.2: Variation of Rayleigh and Nusselt number with wall temperature T_{w} relative to quiescent air temperature $T_\infty = 26\ ^\circ\mathrm{C}$.

The convection coefficient $\overline{h}_s$ can be written as a function of the Nusselt number $\overline{Nu}_L$, the thermal conductivity k and the characteristic length L^* as:

$$\overline{h}_s = \frac{k}{L^*}\overline{Nu}_{L^*} \tag{3.9}$$

Finally, the heat loss by convection, q''_{conv}, can be computed from:

$$q''_{\mathrm{conv}} = \overline{h}_s A_{\mathrm{w}} \Delta T \tag{3.10}$$

Where $\Delta T = T_{\mathrm{w}} - T_\infty$.

Convective contributions of the lower and upper surfaces, $(q''_{\mathrm{conv}})_{\mathrm{low}}$ and $(q''_{\mathrm{conv}})_{\mathrm{up}}$ respectively, for the total heat losses are presented in Figure 3.3.

Estimation of the radiation term

The estimation of the radiation component q''_{rad} is obtained directly from Stephan-Boltzmann equation:

$$q''_{\mathrm{rad}} = \varepsilon \sigma_{\mathrm{SB}} (\Delta T)^4 \tag{3.11}$$

Where ε is the emissivity (assumed to be equal to $\varepsilon = 0.96$), $\sigma_{\mathrm{SB}} = 5.6703 \times 10^{-8}\ \mathrm{kg/(s^3.K^4)}$ is the Stefan-Boltzmann constant and $\Delta T = T_{\mathrm{w}} - T_\infty$.

Comparison of correlations with experimental values

Experimental measurements of the dissipated heat flux were performed using six different electrical currents, $I \in \{5, 7, 9, 10, 12, 15\}\ \mathrm{A}$, and the results are presented in Table 3.4 as mean and standard deviation for five consecutive measurements. The generated heat flux q''_{Joule} is calculate for each imposed current, using Equation 3.3.

Table 3.4: Experimental measurements of dissipated heat for different imposed currents.

Current, I [A]	Voltage, V [mV]	q''_{Joule} [W/m^2]	T_{w} [°C]	Experimental dissipated heat [W/m^2]
5	244	224.85	43.41 ± 0.02	224.35 ± 2.42
7	343	443.23	57.29 ± 0.13	438.84 ± 3.24
9	443	737.77	74.24 ± 0.09	731.09 ± 3.69
10	497	914.50	84.14 ± 0.18	913.42 ± 7.40
12	603	1328.16	105.30 ± 0.19	1320.81 ± 8.57
15	765	2104.98	140.97 ± 0.12	2099.05 ± 9.97

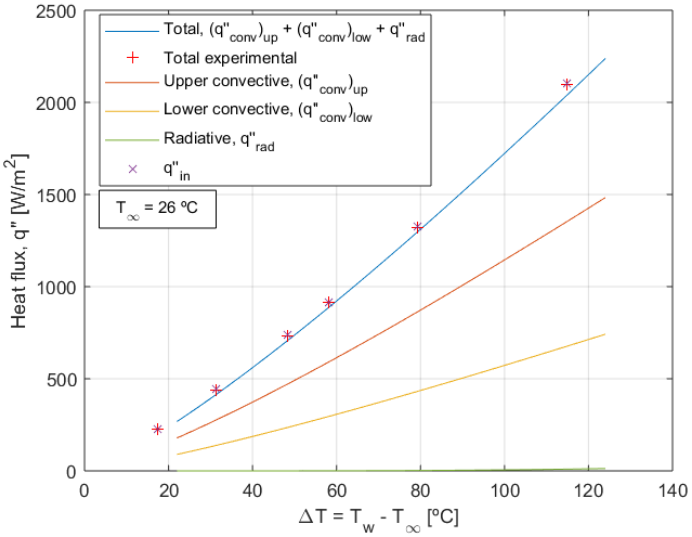

Figure 3.3: Comparison of correlations with experimental values of heat transfer with quiescent air.

Without the contribution of the spray ($q''_{\text{spray}} = 0$), the energy balance presented in Equation 3.4 shows that the heat flux generated by Joule effect is equal to the dissipated heat flux by convection to the air, conduction to the surrounding parts and radiation. Table 3.4 shows very good agreement between these two values, with a maximum deviation of 1%. Furthermore, the experimental values always underestimate the value of generated heat flux.

When comparing the experimental values with those obtained using the correlations, these are also very close. The correlations slightly underestimate the value of dissipated heat flux. This may be related with the fact that heat transfer by conduction was not considered in the calculations. That being the case, this small difference difference is a good prove of how the heat conduction to the surroundings is negligible.

The different contributions to the total heat flux are plotted in Figure 3.3. This plot shows that, according to the correlations, the largest contribution is the one of convection in the upper surface, accounting for almost two-thirds of the total. The contribution of convection in the lower surface is half the one at the upper surface. Moreover, the contribution of radiative heat transfer is the smallest,

contributing less than 0.6% to the total, thus could have been neglected.

When the spray is on, the upper surface of the foil will be covered in fluid, thus does not exchange any heat by convection with air. This means that the only contributions to heat transfer will be convection in the lower surface with quiescent air, radiation, conduction and, of course, the heat exchanged with the spray fluid.

3.3 Experimental setup and method

3.3.1 Experimental setup

Figure 3.4 shows the experimental setup used in this work. The main acquisition systems consist of a *Xenics' Onca-MWIR-InSb-320* thermographic camera and a *Vision Research Phantom v4.2* high-speed camera. Moreover, a type K thermocouple was used to determine the ambient temperature during each experiment T_{amb}, as well as the temperature of the fluid before spraying T_{f}. The spray nozzle position can be adjusted in all three directions of space using knobs. The test fluid is placed inside a $3\ \mathrm{L}$ high pressure vessel which is pressurized using compressed air. The pressure inside the vessel can be regulated using a pressure regulator which is located upstream in the feeding duct. The atomizer and the vessel are separated by a normally closed solenoid valve. The test surface is placed horizontally over the thermographic and the high-speed camera is placed laterally with a LED lamp on the opposite side. The test foil is heated by Joule effect and the power is supplied by a *HP 6274B DC Power Supply*.

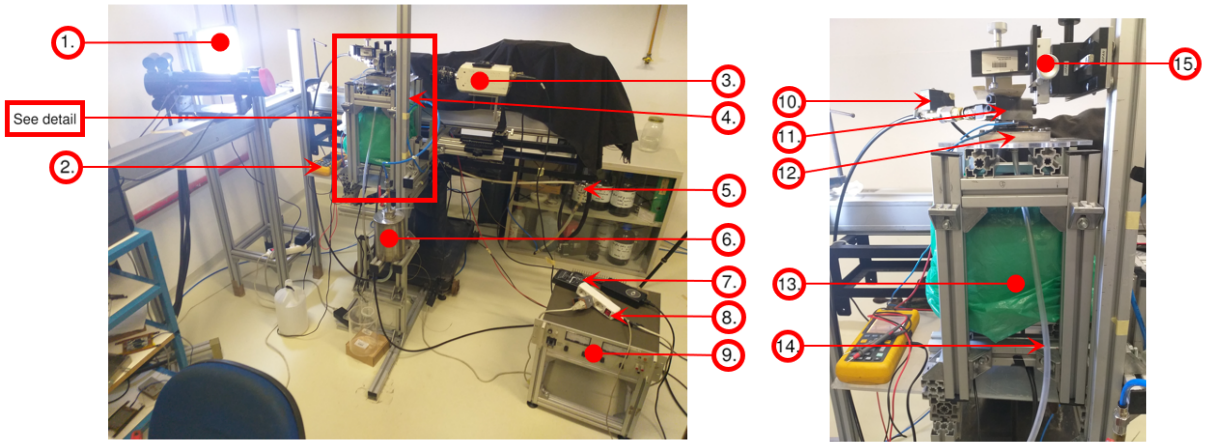

(a) Setup main. (b) Setup detail.

Figure 3.4: Experimental setup: (1) LED lamp, (2) *FLUKE 123 SCOPEMETER* multimeter, (3) *Vision Research Phantom v4.2* high-speed camera, (4) Type K thermocouple, (5) Analogue pressure gauge, (6) $3\ \mathrm{L}$ pressurized vessel, (7) *DATA TRANSLATION DT9828* acquisition system, (8) Button to open solenoid valve, (9) *HP 6274B DC Power Supply*, (10) Normally closed solenoid valve, (11) Hollow-cone pressure-swirl atomizer, (12) Metallic surface and corresponding support, (13) *Xenics' Onca-MWIR-InSb-320* thermographic camera, (14) Fluid collector tube, (15) Atomizer position adjustment knobs.

The detailed list of all the elements composing the setup represented in Figure 3.4 can be found in Table 3.5. This Table includes the uncertainties of each measurement equipment used in the experimental setup of this work.

Table 3.5: Equipment list with uncertainties.

Legend of Figure 3.4	Description	Uncertainty
1	LED lamp	–
2	*FLUKE 123 SCOPEMETER* multimeter	Voltmeter: ± 1 mV
3	*Vision Research Phantom v4.2* high-speed camera	–
4	Thermocouple	± 0.03 °C
5	Analogue pressure gauge	± 1 psi
6	3 L pressurized vessel	–
7	*DATA TRANSLATION DT9828* acquisition system	–
8	Button to open solenoid valve	–
9	*HP 6274B DC Power Supply*	Current gauge: ± 0.5 A
10	Normally closed solenoid valve	–
11	Hollow-cone pressure-swirl atomizer	–
12	Metallic surface and corresponding support	–
13	*Xenics' Onca-MWIR-InSb-320* thermographic camera	–
14	Fluid collector tube	–
15	Atomizer position adjustment knobs	± 0.5 mm

3.3.2 Experimental method

Two input currents ($I = 10$ A and $I = 15$ A) and two atomizer heights ($Z = 10$ mm and $Z = 20$ mm) were selected for this study, which combined, result in four different working conditions. All fluids were analysed for these four conditions. From Table 3.4 can be seen that the selected input currents result in: for $I = 10$ A an input heat flux of approximately $q''_{\text{Joule}} = 914.50$ W/m^2 and an initial surface temperature of $T_0 = 84.14$ °C; whereas, for $I = 15$ A the heat flux is $q''_{\text{Joule}} = 2104.98$ W/m^2 and the initial surface temperature of $T_0 = 140.97$ °C.

After measuring the temperature of the fluid to be tested, the fluid is placed in the high pressure vessel. High-speed and thermographic cameras are setup, following the procedures presented in Appendixes A and B, respectively. The nozzle height relative to the foil is adjusted as necessary. Then, the compressed air valve is open to pressurize the vessel. A thermographic video with 5 frames of the foil before heating is recorded. Thereafter, the power source is turned on and set to the desired current. While the foil temperature increases, the ambient temperature and the difference of electric potential between the contacts are checked using the multimeter and are registered. Once the temperature of the foil has stabilized, the thermographic and high-speed recordings are initiated. The solenoid valve is only opened once the thermographic camera instantaneous recording rate has stabilized. When the recordings are finished, the surface is cleaned using acetone and distilled water. For each experimental condition, three identical tests were performed in a row. When changing the test fluid, all wet parts are cleaned with distilled water and dried.

3.4 Infrared thermography

Infrared thermography (IR) is an optical technique used to obtain thermal maps. It is based on the Stefan-Boltzmann law, which states that: any object at a temperature higher than absolute zero, $0\ \mathrm{K}$, emits radiation proportional to the power four of the temperature. The Stefan-Boltzmann law is mathematically expressed as, Equation 3.12:

$$W_{\mathrm{obj}} = \varepsilon \sigma_{\mathrm{SB}} {T_{\mathrm{obj}}}^4 \tag{3.12}$$

Where W_{obj} is the energy emitted by the object, ε is the emissivity, σ_{SB} is the Stefan-Boltzmann constant and T_{obj} is the temperature of the object.

The thermographic camera sensor captures the total transmitted energy W_{tot}. This value is different from the radiation emitted by the object of study W_{obj}, as surrounding atmosphere also emits radiation W_{atm} and the object also reflects some radiation W_{refl}. Thus, the total transmitted energy W_{tot} may be written as:

$$W_{\mathrm{tot}} = W_{\mathrm{obj}} + W_{\mathrm{refl}} + W_{\mathrm{atm}} \tag{3.13}$$

This total transmitted energy W_{tot} is captured by the camera sensor and is converted to a value of Analog to Digital unit (ADU). The output of the camera measurement is therefore a cube of ADU values, where one of the dimensions is time and the other two dimensions correspond to the two directions of the camera sensor.

These cubes of ADU values are then processed using an updated version of a MATLAB script initially developed by Pontes [57]. The updated code is presented in Appendix C. The high-level algorithm of this routine is presented in Figure 3.5.

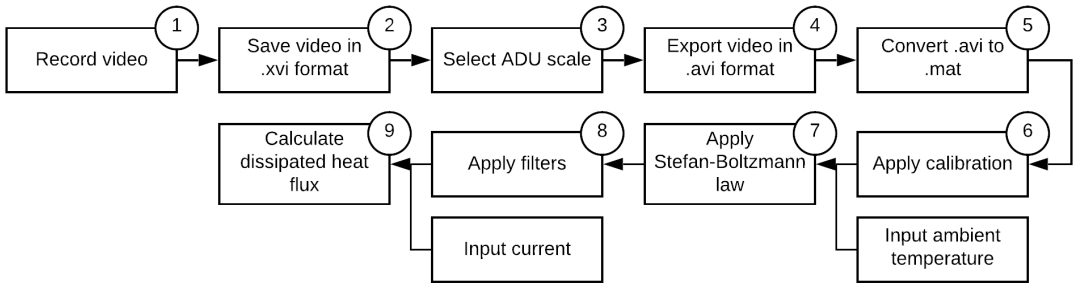

Figure 3.5: Thermographic video processing algorithm.

The conversion of ADU to temperatures starts with the calibration proposed by Pontes [57] and is described by the following polynomial:

$$\mathrm{ADU} = -1.49 \times 10^{-6} {W_{\mathrm{tot}}}^3 + 8.47 \times 10^{-3} {W_{\mathrm{tot}}}^2 - 3.27 W_{\mathrm{tot}} + 1570 \tag{3.14}$$

Where W_{tot} is in $\mathrm{W/m^2}$. The obtained W_{tot} is then used to compute the object temperature T_{obj}

from combining Equations 3.12, 3.13 and the ambient temperature.

3.4.1 Heat flux computation

Temporal evolution of the dissipated heat flux q''_{diss} may be computed from the cubes of temperatures. This is done by applying the pixel energy balance method, suggested by Sielaff [62], which is presented in Figure 3.6.

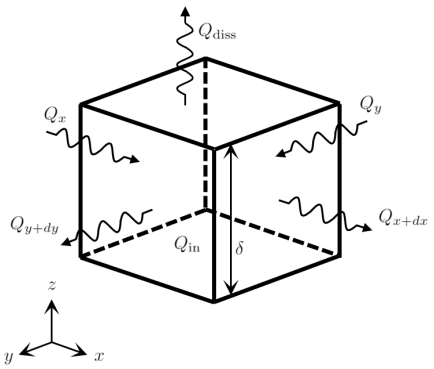

Figure 3.6: Pixel energy exchanges with the surroundings.

The energy balance to the pixel is mathematically written as:

$$q''_{\text{diss}} = q''_{\text{in}} + k_h \delta \left(\frac{\partial^2 T}{\partial x^2} + \frac{\partial^2 T}{\partial y^2} \right) - \rho_h c_{p,h} \delta \frac{\partial T}{\partial t} \tag{3.15}$$

Where q''_{diss} is the dissipated heat flux through the upper and lower surfaces, q''_{in} is the input heat flux (in this case, $q''_{\text{in}} = q''_{\text{Joule}}$), k_h is the thermal conductivity of the material, δ is the foil thickness, ρ_h is the density of the material and $c_{p,h}$ is the specific heat capacity of the material. As explained in Section 3.2.3, the input heat flux is the heat resulting by Joule effect which is estimated using Equation 3.3.

The temperature across the foil is assumed to be constant. This can be confirmed as a good assumption by doing the Biot number analysis Bi. Biot number is the ratio between the temperature difference in the solid relative to the temperature difference between the solid and the fluid. Mathematically, Biot number is given by:

$$Bi = \frac{h_c \times \delta}{k_h} \tag{3.16}$$

Where h_c is the convection heat transfer coefficient between the study solid and fluid.

According to Incropera et al. [63], if the Biot number is much smaller than one ($Bi << 1$), the resistance to thermal conductivity inside the solid is much smaller than the resistance of convection between the fluid and the solid. Therefore, the assumption of constant temperature across the solid is acceptable.

In the present case, $\delta = O(10^{-5})$ m, $k_h = O(10^{1})$ W/(m.K) and $h_c = O(10^{3})$ W/(m^2.K). By applying Equation 3.16, $Bi = O(10^{-3}) << 1$. The condition is met, thus the approximation is valid.

The space and time derivatives are approximated using finite differences. The results of this method can be seen in Equations 3.17 and 3.18.

$$\frac{\partial^2 T}{\partial x^2} \approx \frac{T(x+1,y,t) - 2T(x,y,t) + T(x-1,y,t)}{\Delta x^2} \tag{3.17}$$

$$\frac{\partial T}{\partial t} \approx \frac{T(x,y,t) - T(x,y,t-1)}{\Delta t} \tag{3.18}$$

The second derivative in the y direction is similar to the one in the x direction, presented in Equation 3.17.

Uncertainty analysis

The calculation of dissipated heat flux q''_{diss} is, as seen in Equation 3.15, a pixel energy balance. This expression takes into account the imposed heat flux q''_{in} by Joule effect and partial derivatives of temperature weighted by foil properties. As this study intends to be mainly comparative between fluids, instead of determining the absolute values of dissipated heat flux, for purposes of estimating the uncertainty in the q''_{diss} calculation, only parameters which differ between each test and directly impact this calculation are considered.

The first term q''_{in} is calculated using Equation 3.3, which includes the input current. Therefore, measurement of the input current directly impacts the calculation of dissipated heat flux. From Table 3.5, the uncertainty in the measurement of current I is $\delta I = \pm 0.5$ A.

The measurement of the temperatures using thermography is also subject to uncertainty, which comes from the camera sensibility. In Figure 3.7, the temperature T is presented in blue as a function of Analog to Digital unit (ADU). These values were obtained using Equation 3.14, assuming an ambient temperature of $T_{\text{amb}} = 26\ ^{\circ}\text{C}$ and an emissivity of $\varepsilon = 0.96$. The orange line presented in this Figure is a measure of the camera sensibility ΔT and corresponds to the difference between the corresponding temperature for one ADU and the temperature of the previous ADU (or $\Delta T = T_i - T_{i-1}$, where T_i is the temperature corresponding to ADU i).

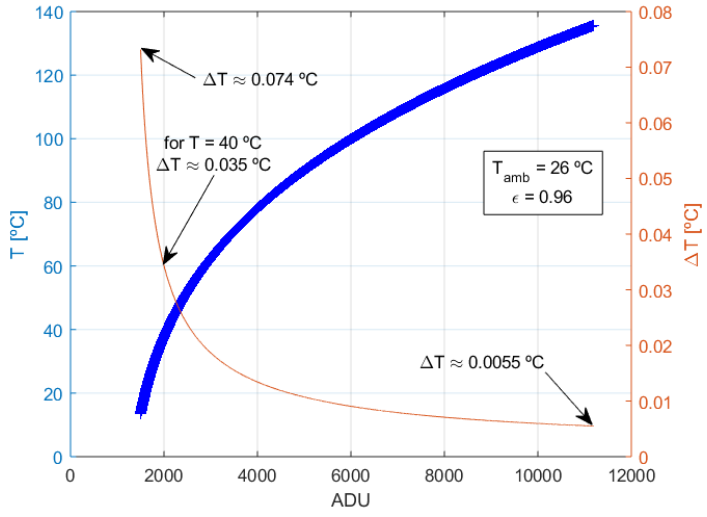

Figure 3.7: Temperature T (blue line) and $\Delta T = T_i - T_{i-1}$ (orange line) as a function of ADU.

The orange line shows clearly that the sensibility of the camera is one order of magnitude higher for the highest temperatures (or highest values of ADU) when compared to lowest temperatures (or lowest values of ADU). Hence, the calibration is coarser for smaller temperatures and finer for higher temperatures. For the conditions in which this project was performed, the steady-state regime temperatures are of the order of $40\ ^{\circ}\mathrm{C}$, which corresponds to the coarser spectrum of the calibration. As a result, keeping in mind that the analysis is performed for the worse case scenario, i.e. for the maximum uncertainty in the dissipated heat flux calculation, an uncertainty of $\delta T = \pm 0.035/2\ ^{\circ}\mathrm{C} = \pm 0.0175\ ^{\circ}\mathrm{C}$ is selected for temperature measurement.

Thus, the variables from combining Equations 3.3, 3.15, 3.17 and 3.18 which will be considered in this uncertainty are: I, $T(x,y,t)$, $T(x{+}1,y,t)$, $T(x{-}1,y,t)$, $T(x,y{+}1,t)$, $T(x,y{-}1,t)$ and $T(x,y,t{-}1)$. As proposed by Palmer [64], the rule to calculate the uncertainty of a multi-non-correlated-variable function f is:

$$\delta f(x_i,...,x_N) \approx \sqrt{\sum_{i=1}^{N}\left(\frac{\partial f}{\partial x_i}\delta x_i\right)^2} \tag{3.19}$$

Where δf is the uncertainty of the function output, x_i is variable i of f, N is the number of variables and δx_i is the uncertainty of x_i variable. In the present case, the partial derivative of q''_{diss} with respect to the imposed current I is:

$$\frac{\partial q''_{\mathrm{diss}}}{\partial I} = \frac{2R}{A}I \tag{3.20}$$

Where R is the electrical resistance and A is the foil area. The partial derivative with respect to $T(x,y,t)$ is:

$$\frac{\partial q''_{\mathrm{diss}}}{\partial T(x,y,t)} = -4\frac{k_h\delta}{\Delta x^2} - \frac{\rho_h c_{p,h}\delta}{\Delta t} \tag{3.21}$$

The partial derivatives with respect to $T(x+1,y,t)$, $T(x-1,y,t)$, $T(x,y+1,t)$ and $T(x,y-1,t)$ are the same and equal to:

$$\frac{\partial q''_{\mathrm{diss}}}{\partial T(x+1,y,t)} = \frac{\partial q''_{\mathrm{diss}}}{\partial T(x-1,y,t)} = \frac{\partial q''_{\mathrm{diss}}}{\partial T(x,y+1,t)} = \frac{\partial q''_{\mathrm{diss}}}{\partial T(x,y-1,t)} = \frac{k_h\delta}{\Delta x^2} \tag{3.22}$$

The partial derivative with respect to $T(x,y,t-1)$ is:

$$\frac{\partial q''_{\mathrm{diss}}}{\partial T(x,y,t-1)} = \frac{\rho_h c_{p,h}\delta}{\Delta t} \tag{3.23}$$

Finally, by applying equation 3.19, the uncertainty of the dissipated heat flux q''_{diss} is given by:

$$\delta q''_{\mathrm{diss}} \approx \sqrt{\left(\frac{2R}{A}I\times\delta I\right)^2 + \left[\left(-4\frac{k_h\delta}{\Delta x^2} - \frac{\rho_h c_{p,h}\delta}{\Delta t}\right)\delta T\right]^2 + 4\left(\frac{k_h\delta}{\Delta x^2}\delta T\right)^2 + \left(\frac{\rho_h c_{p,h}\delta}{\Delta t}\delta T\right)^2} \tag{3.24}$$

To perform an estimation of the uncertainty in the q''_{diss} calculation, the following constants are con-

sidered: $R = 0.0483\ \Omega$, $A = 0.0054\ \mathrm{m}^2$, $k_h = 14.9380\ \mathrm{W/mK}$, $\delta = 20 \times 10^{-6}\ \mathrm{m}$, $\Delta x = 0.22 \times 10^{-3}\ \mathrm{m/px}$, $\Delta t = 0.025\ \mathrm{s/px}$, $\rho_h = 7880\ \mathrm{kg/m^3}$, $c_{p,h} = 477\ \mathrm{J/kgK}$ and $I = 15\ \mathrm{A}$. Replacing all these constants and the measurement uncertainties in Equation 3.24, the uncertainty of the calculated dissipated heat flux is $\delta q''_{\mathrm{diss}} \approx 561.2\ \mathrm{W/m^2}$ ($\delta q''_{\mathrm{diss}} \approx 552.2\ \mathrm{W/m^2}$ for $I = 10\ \mathrm{A}$).

The obtained values for the uncertainty are in fact very high, corresponding to 61% and 28% of the dissipated heat flux for $I = 10\ \mathrm{A}$ and $I = 15\ \mathrm{A}$, respectively, as will be seen in Chapter 4. However, this estimation was performed admitting that the temperature in one pixel at given instant $T(x, y, t)$ is not correlated with the temperatures of neighbor pixels $T(x+1, y, t)\ T(x-1, y, t)\ T(x, y+1, t)\ T(x, y-1, t)$, with the temperature in the previous instant $T(x, y, t-1)$ nor with the input current I. This can not happen in reality and the values are expected to have high positive correlation. The covariance term, related with variable correlations, which appears in the uncertainty of a two-variable function are of the form $2bc\sigma_{BC}$. Where σ_{BC} is the covariance between the variables B and C, b and c are the deterministic constant which multiply variables B and C, respectively. Given that there is only one negative constant (the one which multiplies $T(x, y, t)$), which is in fact the largest in absolute value, and that the variables are positively correlated ($\sigma_{BC} > 0$), sum of the covariance terms is expected to be negative, thus reducing the estimation of the uncertainty. For this reason, the results obtained in this Section are in fact upper bounds of the uncertainties and the real values are expected to be much lower.

3.4.2 Optimization of the recording methodology

Due to the limited recording system of the *Xenics' Onca-MWIR-InSb-320* thermographic camera, some oscillations of the recording rate were experienced. As seen in Equation 3.15, the recording rate enters in the calculation of dissipated heat flux and therefore is also a source of uncertainty. It was observed that these oscillations were higher for higher recording rates, thus this work had to take advantage of the maximization of recording rate option in the camera software. When this option is disabled, the camera maintains the recording rate at the instantaneous maximum, consequently resulting in severe oscillations as the number of acquired frames increases. When enabled and set to a much lower value than that observed without restrictions, the instantaneous recording rate becomes much more constant with smaller oscillations. Moreover, was observed that with the increase of video length, the recording rate tends to decrease.

As it will be explained later in Chapter 4, the cooling curve associated with this spray atomizer has two regimes: a transient regime lasting approximately $3\ \mathrm{s}$, followed by a steady-state regime. These regimes are characterized by significant variations and no significant variations in mean foil temperature, respectively. The transient regime occurs very fast (lasting a maximum of 3 seconds). Hence, given the fluctuations in recording rates, the transient regime will not be analysed in great detail. For the steady-state regime, given that, by definition, no large variations of temperature and consequently dissipated heat flux are to be expected, the mean values will be considered.

To find the optimal recording settings, many different combinations of maximized recording rate and video length were tested. The best configuration, which resulted in a reasonable recording rate and

allowed to capture at least $12\ \mathrm{s}$ of the steady-state regime, was found to be a recording rate of 40 frames per second (FPS) and a length of 1000 frames. Moreover, the solenoid valve which connects the pressurized vessel containing the fluid and the atomizer, was only opened once the instantaneous frame rate would stabilize. The zoom function of the camera software was also tested and increases significantly the recording rate. However, it introduced large noise patterns in the images, which compromised the post-processing of the video, and was the reason why this option was not used.

Moreover, as explained before, the cooling curve has a regime of high temperature variations and a steady-state. The first regime corresponds to a temperature decrease from 80 or $140\ ^{\circ}\mathrm{C}$, depending on the input current, to as low as $40\ ^{\circ}\mathrm{C}$. The thermographic videos are exported in 8 bit format, resulting in a spectrum of 256 different Analog to Digital unit (ADU) values. Therefore, to take full advantage of the camera sensitivity in the steady-state regime, where no more than 256 different values of temperature can be read due to camera sensitivity limit, the thermographic video is exported in two parts. The first one, of the transient regime, is exported with the required ADU scale to cover all values from the highest to the lowest temperature in the end of this regime. Whereas, the second part of the video, corresponding to the steady-state regime, is exported with a 256 consecutive ADU scale which covers the full temperature spectrum. These technique allows for the best possible sensitivity in the transient regime and the highest sensitivity of 256 consecutive ADU scale in the steady-state regime.

3.4.3 Image noise and background

When talking about imaging measurement techniques, noise is a great concern. Noise is random and may have different sources: in the surroundings, camera sensor, electronics or analog-to-digital converter. Depending on the characteristics and the origin of the noise, Farooque and Rohankar [65] have established the following classifications:

- Gaussian noise – Arise during acquisition in the sensor. Gaussian noise is additive, independent at each pixel and independent of the signal intensity;
- Salt-and-pepper noise – Impulsive noise. As a result, the image will have dark pixels in bright regions and bright pixels in dark regions. Salt-and-pepper noise is originated in analog-to-digital converter or bit errors in transmission;
- Anisotropic noise – Noise patterns with well defined orientation in images;
- And others...

To reduce the noise of images, noise removing filters have been developed. However, one noise filter does not work well for all the noise types and many times helps reduce only one of the types. These noise filters can be classified using different criteria. Vardasca et al. [66] classified noise removing filters according to linearity of the methods:

- Linear filters – These filters operate by processing the original image with a convolution mask. The trade-off of these methods is a blurring effect on the image. Examples of this type of filters are: mean, Gaussian and homomorphic;

- Non-linear filters – Filters which do not generate an output as a linear function of the original image. Non-linear filters check if the pixel value is valid or noise affected. While these filters produce less or no blurring, they introduce new and not necessarily correct information into the image. Examples of this type of filters are: median, Poisson, Wiener and speckle.

Figure 3.8 shows a non-treated thermographic image of the metallic foil before heating. Figure 3.9 is the corresponding intensity histogram.

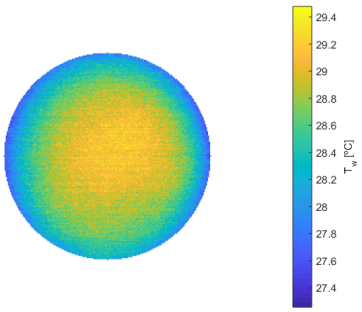

Figure 3.8: Non-treated thermographic image of the metallic foil before heating.

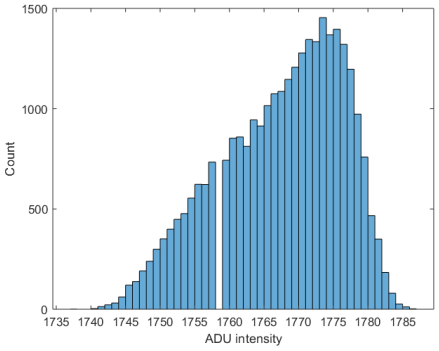

Figure 3.9: Intensity histogram of image presented in Figure 3.8 in ADU scale.

As Figure 3.8 is of the non-heated metallic foil, it is expected to be all at the same temperature. However, it can be seen that the center of the interest area has higher temperature than the surrounding edge. To correct this, the weighted background removal filter developed by Pontes [57] is implemented. This filter will also compensate the present anisotropic noise, which can be seen as horizontal lines.

For the steady-state regime video, where the sensitivity of the thermographic camera is set to the maximum, a frame of the cold non-heated foil is used to compute the background matrix. When analysing the full spray video (including the transient regime), a frame of the heated foil is used.

Figure 3.10 is the thermographic footprint of a spray and Figure 3.11 is the respective intensity histogram. The background removal filter has been applied to the image.

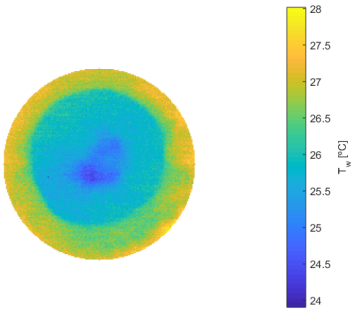

Figure 3.10: Thermographic image after background removal.

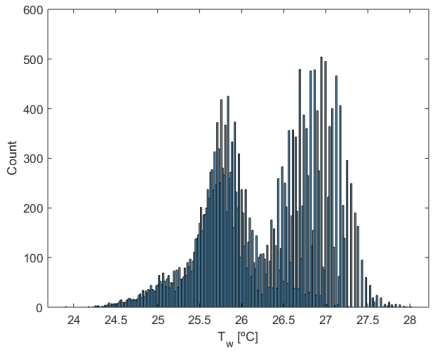

Figure 3.11: Intensity histogram of image presented in Figure 3.10.

It can be seen that not all noise has been removed and that the patterns in the histogram suggests Gaussian noise. The most effective filter to remove Gaussian noise is the Gaussian filter (Farooque

and Rohankar [65] and Vardasca et al. [66]). As a linear filter, the Gaussian filter has the advantage of not introducing new information to the image. Due to the large amount of noise, a Gaussian filter with standard deviation 2 and 9×9 pixel kernel is selected.

Figure 3.12 shows the thermal footprint presented in Figure 3.10, but after applying the Gaussian filter. Figure 3.13 is the respective intensity histogram.

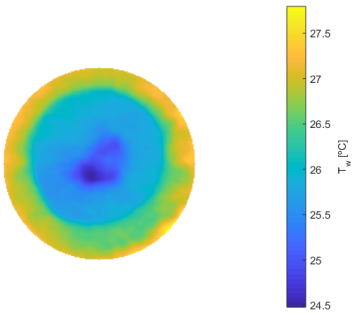

Figure 3.12: Thermographic image with background removal and Gaussian filter.

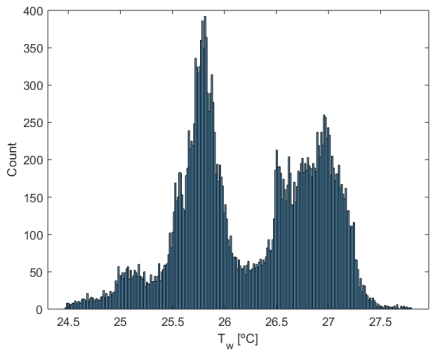

Figure 3.13: Intensity histogram of image presented in Figure 3.12.

When comparing Figures 3.12 with 3.10, it can be observed that now the image is much cleaner. Comparing the intensity histograms of each image also suggests that the Gaussian filter is very effective in reducing this particular noise and results in a much smoother curve.

3.5 Atomizer and PDI characterization

The hollow-cone pressure-swirl atomizer used in this work, which is schematically represented in Figure 3.14, has already been previously characterized in terms of droplet dynamics using Phase Doppler Interferometry (PDI) by Figueiredo [56] and Malý et al. [67]. These studies have analysed the impact of adding nanoparticles on the diameters and velocities of droplets. This atomizer operates at an ejection pressure of 0.5 MPa and delivering a mass flow rate of 7 kg/h.

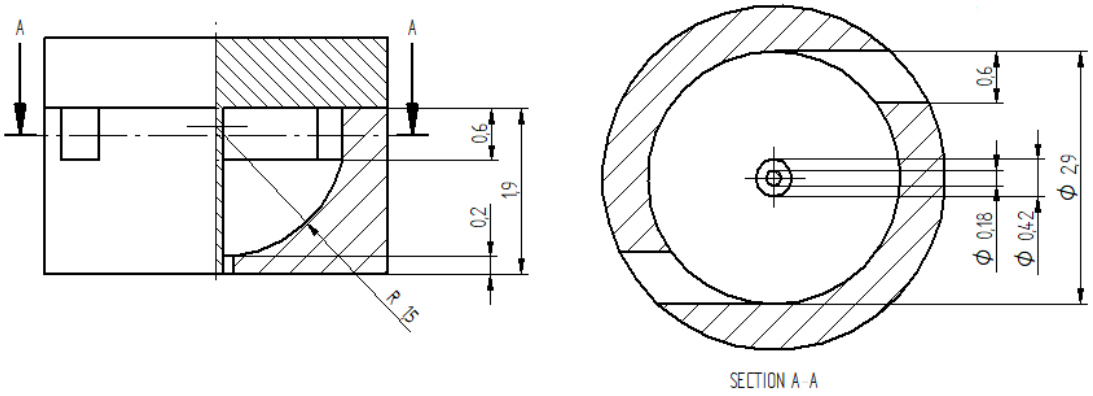

Figure 3.14: Representation of the hollow-cone pressure-swirl atomizer with dimension in millimeters (adapted from Malý et al. [67]).

Figure 3.15 is a compilation of the PDI results obtained by Figueiredo [56] for this particular spray

atomizer using different fluids. This Figure shows the Ohnesorge number Oh, as a function of the Reynolds number Re, for different fluids. The black lines correspond to the limits of the droplet impact criteria for wetted surfaces and $r^* = r/r_{\max}$, where r and $r_{\max}$ are the radial distance and maximum radial distance, respectively. On the left side are the plots for atomizer height relative to the foil of $Z = 10$ mm (corresponding to plots A, C and E) and on the right side are the plots for $Z = 20$ mm (corresponding to plots B, D and F).

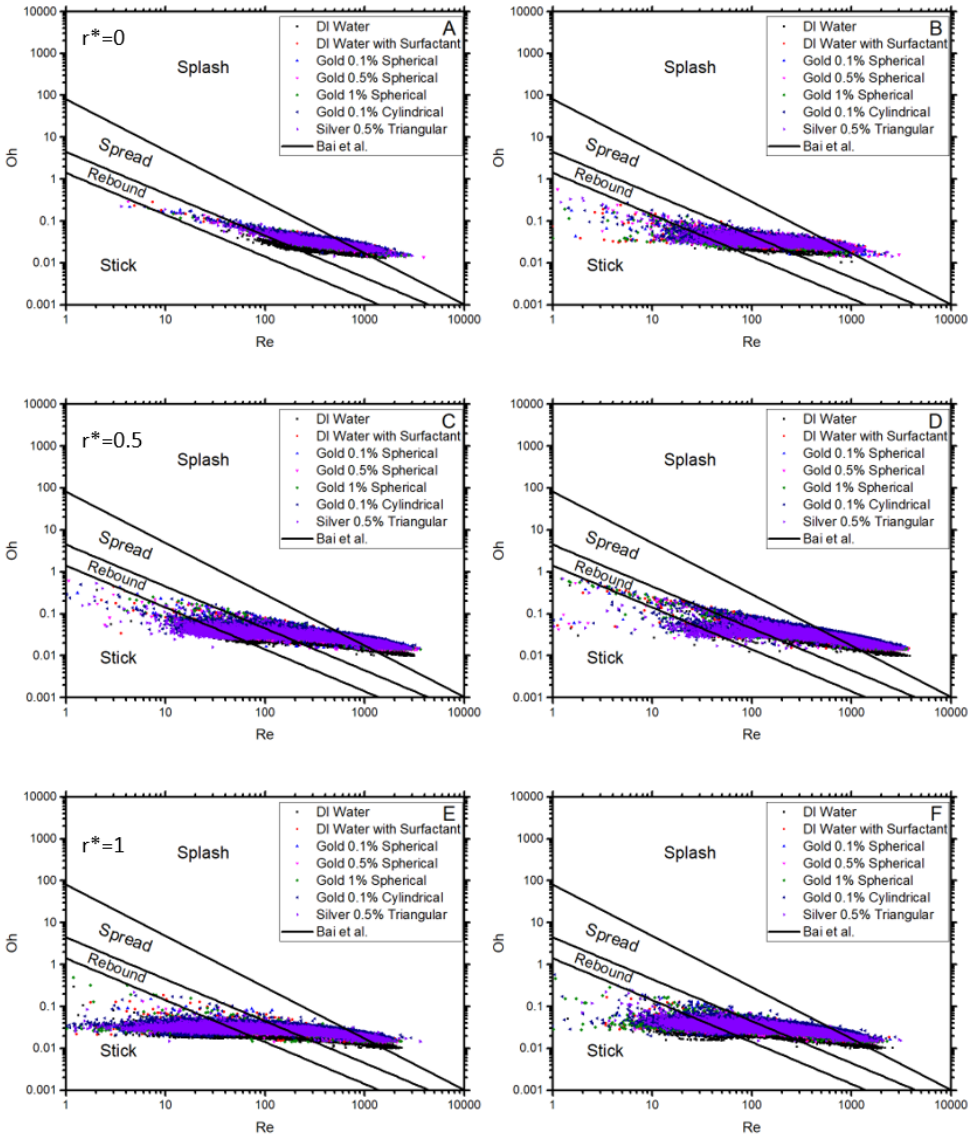

Figure 3.15: Phase Doppler Interferometry (PDI) results, including wetted surface impact criteria, obtained for the spray atomizer by Figueiredo [56].

The work of Figueiredo [56] and Malý et al. [67] did not show any significant changes in atomization nor in the outcomes of droplet impact on the wetted surface for the different nanofluids.

3.6 Fluid selection, preparation and characterization

3.6.1 Fluid selection

As explained previously in Section 3.5, the spray dynamics for the atomizer used in this work have already been characterized for alumina (aluminium oxide), silver and gold nanofluids, in previous studies (Figueiredo [56] and Malý et al. [67]). To take advantage of this work, alumina (Al_2O_3) and silver (Ag) nanoparticles were selected.

On the one hand, alumina is cheap and abundant commercially. For this reason, alumina nanofluids were prepared in different mass concentrations to study the impact of nanoparticles concentration in heat transfer. On the other hand, silver is more expensive and has higher thermal conductivity. Silver nanoparticles can be prepared in different shapes, thus this was used to compare how nanoparticle shape impacts heat transfer.

These nanoparticles were are added to a base solution of 0.05% (m/m) cetyltrimethylammonium bromide (CTAB). This solution was proven to be stable and optimal by Figueiredo [56].

3.6.2 Nanofluid preparation

Alumina nanofluids

The alumina nanofluids were prepared with the mass concentrations of 0.5% (m/m), 1% (m/m) and 2% (m/m) with 0.05% (m/m) of cetyltrimethylammonium bromide (CTAB). The characteristics of the CTAB and alumina powder are presented in Tables 3.6 and 3.7, respectively.

Table 3.6: Characteristics of cetyltrimethylammonium bromide (CTAB).

Characteristic	Value	Unit
Brand	Sigma	–
Purity	99	%
Lot	54H0996	–

Table 3.7: Characteristics of the alumina powder.

Characteristic	Value	Unit
Brand	Alfa Aesar	–
Particle size	$40 - 50$	nm
Purity	99.5	%
Surface ratio	$32 - 40$	$\mathrm{m^2/g}$
Lot	X24E065	–

Alumina nanofluids were prepared using a two-step preparation method (as presented in Section 2.4.1). The procedure used was the following:

1. Necessary CTAB and alumina powder were weighed, using *KERN ABS 80-4N* scale;
2. Necessary distilled water was weighed, using *UWE HGS-1500* scale;
3. CTAB, alumina powder and the water were combined in the same container;
4. The mixture was stirred at $1200\ \mathrm{rpm}$ for 20 minutes, using *Rotilabo MH 15* magnetic stirrer;
5. Finally, the mixture was sonicated with an amplitude of 60% and frequency of 40% for 20 minutes, using *Hielscher UPT200Ht* ultrasonic probe.

Silver nanofluids

Silver nanofluids were prepared by the Structural Chemistry Center of the Chemical Engineering department at Instituto Superior Técnico. The mass concentration of silver nanoparticles was 1% (m/m) with 0.05% (m/m) of cetyltrimethylammonium bromide (CTAB). Two different geometries of silver nanoparticles were prepared: spherical and triangular. The preparation method of the silver nanofluids is described in Suh et al. [68] and Creighton et al. [69].

3.6.3 Nanofluid characterization

Table 3.8 presents theoretical estimations of some nanofluid thermophysical properties at $25\ ^{\circ}\mathrm{C}$, performed using the correlations of Section 2.4.2. The specific mass of the fluids ρ is calculated using Equation 2.9. The specific heat capacity c_p is calculated using Equation 2.10. Thermal conductivity of alumina and spherical silver nanofluids is calculated using Equation 2.11. For the triangular silver nanofluids, the thermal conductivity is estimated using Equation 2.12.

Table 3.8: Properties of the fluids determined theoretically at $25\ ^{\circ}\mathrm{C}$ (* – specific heat capacity and thermal conductivity of CTAB were not found in literature, thus the properties of the base fluid are assumed to be equal to the ones of distilled water, which is a good approximation given the low concentration of CTAB used).

Fluid composition	ρ [$\mathrm{g/cm^3}$]	c_p [$\mathrm{kJ/(kg.K)}$]	k [$\mathrm{W/(m.K)}$]
Water	0.9982	4.22	0.6060
Water, 0.05% (m/m) CTAB	0.9987	*	*
Water, 0.05% (m/m) CTAB, 0.5% (m/m) Alumina	1.0024	4.20	0.6082
Water, 0.05% (m/m) CTAB, 1% (m/m) Alumina	1.0062	4.19	0.6104
Water, 0.05% (m/m) CTAB, 2% (m/m) Alumina	1.0108	4.15	0.6149
Water, 0.05% (m/m) CTAB, 1% (m/m) Spherical Silver	1.0229	4.12	0.6106
Water, 0.05% (m/m) CTAB, 1% (m/m) Triangular Silver	1.0229	4.12	0.6096

Properties of CTAB were not found in literature. For this reason, the properties of the base fluid (distilled water with 0.05% (m/m) CTAB) were considered equal to those of water. This is a good approximation for most of the properties, given the low concentration of CTAB used. However, literature shows that surfactants tend to deteriorate the thermal performance of fluids [23].

The estimations show a decrease of the specific heat capacity and an increase of thermal conductivity with the addition of the nanoparticles. Specific heat of solid alumina and solid silver is one order of magnitude lower than that of the base fluid, whereas the thermal conductivity is three orders of magnitude higher. Thus, resulting in the differences observed in Table 3.8.

Surface tension and static contact angle with the surface were measured for the different fluids using *THETA* optical tensiometer by *Attension*, Figure 3.16. *Pendant drop* method was used to measure surface tension and *Sessile drop* method was used to measure the contact angle with the foil. The parameters used during the measurement are presented in Table 3.9.

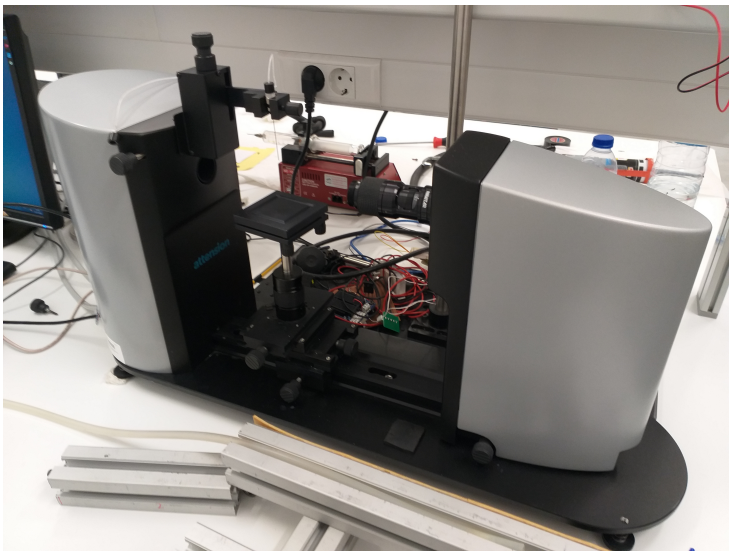

Figure 3.16: *THETA* optical tensiometer by *Attension*.

Table 3.9: Parameters used during measurements with *THETA* optical tensiometer by *Attension*.

Parameter	Value	Unit
Light phase	*(As required.)*	–
Heavy phase	Water	–
Image recording settings	10.0 s at 20% (12 FPS)	–
Drop out size	3.000	μL
Drop in size	5.000	μL
Drop rate	2.000	μL/s
Disp rate	20.000	μL/s
Fill rate	20.000	μL/s

Before each experiment, the room temperature was measured and the system was calibrated using a calibration ball, Figure 3.17. Furthermore, when determining the contact angle using *Sessile drop*, the tensiometer plate was first levelled, Figure 3.18. Detailed description of both methods can be found in Attension [70].

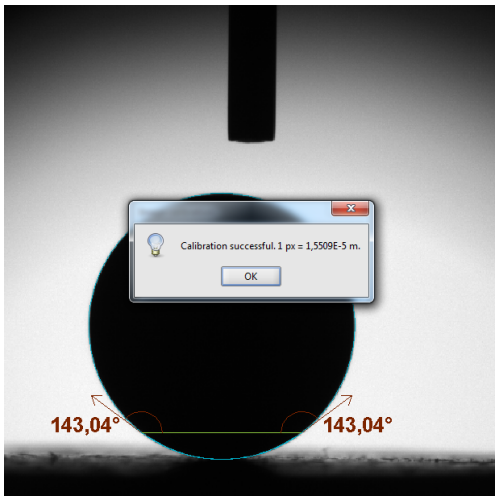

Figure 3.17: Calibration of the tensiometer.

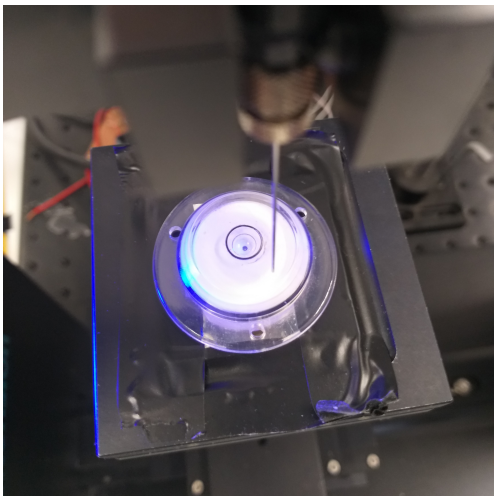

Figure 3.18: Leveling tensiometer plate.

Table 3.10 shows the results of surface tension σ obtained using the *Pendant drop* method, and dynamic viscosity μ for the different fluids. The room temperature when measuring surface tension was $23.98 \pm 0.03\ ^{\circ}\mathrm{C}$. The values of surface tension σ are presented as the mean value and standard deviation of 15 consecutive equal tests. On the other hand, viscosity was measured by the Structural Chemistry Center of the Department of Chemical Engineering in Instituto Superior Técnico, using a *TA instruments ARI 500 ex* rheometer, at ambient temperature $20\ ^{\circ}\mathrm{C}$, with an accuracy of $\pm 5\%$.

Table 3.10: Measured properties of the fluids at $23.98 \pm 0.03\ ^{\circ}\mathrm{C}$.

Fluid composition	Surface tension, σ [$\mathrm{mN/m}$]	Dynamic viscosity, μ [$\mathrm{mPa.s}$]
Distilled water	74.5980 ± 2.2223	1.009
Distilled water, 0.05% (m/m) CTAB	35.9201 ± 0.9189	1.291
Distilled water, 0.05% (m/m) CTAB, 0.5% (m/m) Alumina	39.0268 ± 1.2679	3.572
Distilled water, 0.05% (m/m) CTAB, 1% (m/m) Alumina	40.1761 ± 2.6986	6.815
Distilled water, 0.05% (m/m) CTAB, 2% (m/m) Alumina	40.2364 ± 0.8586	8.835
Distilled water, 0.05% (m/m) CTAB, 1% (m/m) Spherical Silver	40.0111 ± 0.4168	13.175
Distilled water, 0.05% (m/m) CTAB, 1% (m/m) Triangular Silver	43.0687 ± 0.3641	18.903

It can be observed that adding CTAB reduces the surface tension of the base fluid to half of the one of distilled water. Furthermore, the addition of nanoparticles results in a slight increase of surface tension. Comparing the surface tension for the different 1% (m/m) nanofluids, triangular silver nanofluid presents the highest value. Whereas, alumina 1% (m/m) and spherical silver have very similar surface tension values.

In terms of dynamic viscosity μ, Table 3.10 shows that the addition of CTAB, alumina and silver nanoparticles results in a consistent increase of the dynamic viscosity. For the same mass concentration of nanoparticles, silver nanofluids have more than twice the dynamic viscosity of alumina. However, all fluids exhibited Newtonian behavior.

Table 3.11 presents the results of the static contact angle between fluids, the metallic surface and air, obtained using the *Sessile drop* method. As with the *Pendant drop* experiments, the room temperature was $23.98 \pm 0.03\ ^{\circ}\mathrm{C}$. The values of contact angle θ are presented as the mean value and standard deviation of 5 consecutive equal tests.

Table 3.11: Static contact angle between different fluids, the metallic surface and air, at $23.98 \pm 0.03\ ^{\circ}\mathrm{C}$.

Fluid composition	Static contact angle, θ [°]
Distilled water	86.4741 ± 6.4139
Distilled water, 0.05% (m/m) CTAB	53.5818 ± 6.3270
Distilled water, 0.05% (m/m) CTAB, 0.5% (m/m) Alumina	61.8037 ± 2.8827
Distilled water, 0.05% (m/m) CTAB, 1% (m/m) Alumina	59.8934 ± 2.6986
Distilled water, 0.05% (m/m) CTAB, 2% (m/m) Alumina	57.8884 ± 11.2754
Distilled water, 0.05% (m/m) CTAB, 1% (m/m) Spherical Silver	51.0925 ± 3.4547
Distilled water, 0.05% (m/m) CTAB, 1% (m/m) Triangular Silver	47.3165 ± 6.3033

The contact angle measurements depicted in Table 3.11 follow the trend consistent with that of the surface tension shown in Table 3.10, i.e. the contact angles are lower for the base fluid when compared with water, due to the decrease in the surface tension. However, now the increase of nanoparticle concentration results in a decrease of the static contact angle. Moreover, the highest static contact angles are verified for the alumina nanofluids.

Chapter 4

Results

In this Chapter the results obtained in this work will be presented and analysed. The analysis will start with the results obtained for distilled water in Section 4.1. Apart from the objective of comparing thermal performance of nanofluid sprays with plain water, the idea of analysing water spray, in the different working conditions, is to understand the main mechanisms and properties of this specific spray atomizer. Thereafter, in Section 4.2.1, the results obtained when adding only the surfactant will be compared to those obtained with water, with the objective of isolating the effect of the surfactant. Then, in Section 4.2.2, the effect of increasing the nanoparticles concentration in the fluid is inferred, comparing the results obtained with alumina nanofluids. In Section 4.2.3, the objective is to study the influence of nanoparticle shape, by comparing the silver nanofluids. A global comparison of all nanofluids is made in Section 4.2.5. At the end, given the fact that nanofluid stability is an important property in practical applications, the results of a simple visual inspection are presented in Section 4.3.

4.1 Distilled water

Spray cooling curve

As explained in Chapter 3, the solenoid valve connecting the pressurized vessel and the atomizer is only open once the heating of the foil reaches equilibrium. The two heating conditions of the foil were, one for input current of $I = 10$ A, corresponding to a heat flux of $q''_{\text{in}} = 914.50\ \text{W/m}^2$ and an initial foil temperature of $T_0 = 84.14\ ^\circ\text{C}$, and another for input current of $I = 15$ A, corresponding to $q''_{\text{in}} = 2104.58\ \text{W/m}^2$ and $T_0 = 140.97\ ^\circ\text{C}$.

Furthermore, the atomizer was placed at two vertical distances from the foil, at $Z = 10$ mm and at $Z = 20$ mm. Combining the two different input currents and the two different heights of the spray atomizer, resulted in the study of four working conditions.

In Figures 4.1 and 4.2 the plots of mean surface temperature relative to reference temperature ΔT and of dissipated heat flux q''_{diss} are presented, as a function of elapsed time since impact of first liquid on the foil, for the working conditions with imposed current of $I = 10$ A and $I = 15$ A, respectively. The reference temperature T_{ref} is the temperature of the fluid inside the pressurized reservoir, which is the

same for all the experiments and is equal to $T_{\text{ref}} = 21.82 \pm 0.03°\text{C}$.

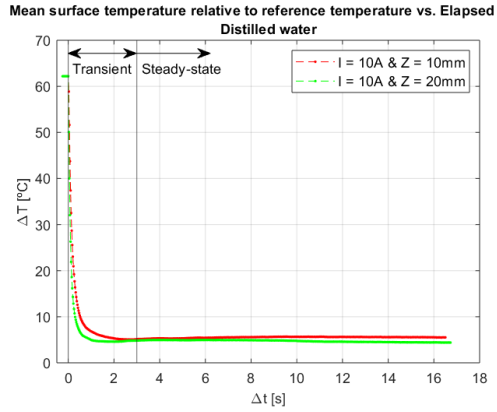

(a) Temporal evolution of mean surface temperature relative to reference temperature, $T_{\text{ref}} = 28.1\ °\text{C}$.

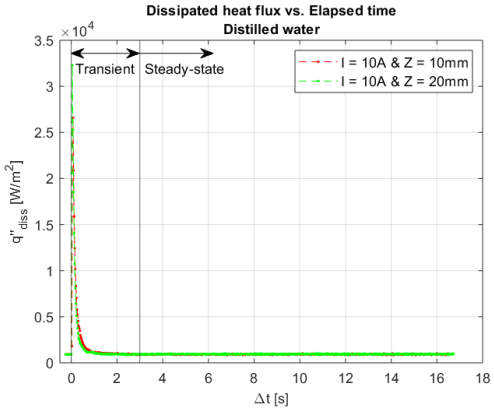

(b) Temporal evolution of dissipated heat flux.

Figure 4.1: Temporal evolution of the difference between mean surface temperature and reference temperature ΔT (Figure 4.1.a) and of the dissipated heat flux q''_{diss} (Figure 4.1.b) for working conditions with imposed current $I = 10\ \text{A}$.

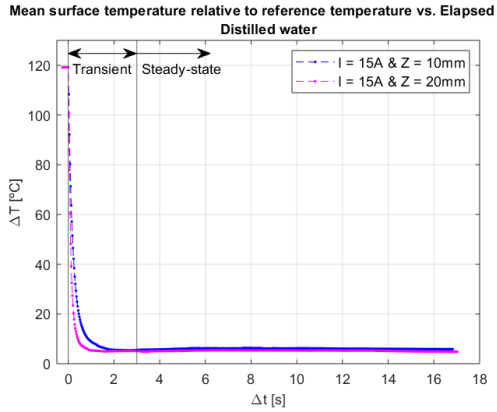

(a) Temporal evolution of mean surface temperature relative to reference temperature, $T_{\text{ref}} = 28.1\ °\text{C}$.

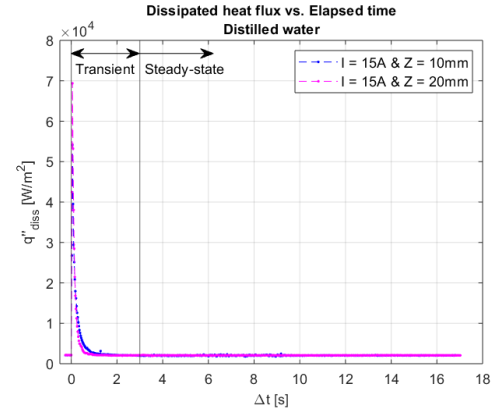

(b) Temporal evolution of dissipated heat flux.

Figure 4.2: Temporal evolution of the difference between mean surface temperature and reference temperature ΔT (Figure 4.2.a) and of the dissipated heat flux q''_{diss} (Figure 4.2.b) for working conditions with imposed current $I = 15\ \text{A}$.

The curves of relative mean surface temperature and dissipated heat flux, presented in Figures 4.1 and 4.2, can be divided into three sections: initial condition (for $\Delta t < 0\ \text{s}$) – the foil temperature is maximum and constant; transient regime (for $0 < \Delta t < 3\ \text{s}$) – sharp decrease in temperature and maximum heat flux is attained; and a steady-state regime (for $\Delta t > 3\ \text{s}$) – temperature and dissipated heat flux no longer vary with time.

Distilled water spray: transient regime

From $\Delta t = 0\ \text{s}$ to $\Delta t \approx 3\ \text{s}$ corresponds to the transient regime of the system. Figures 4.3 and 4.4 are a zoom of the plots presented previously in Figures 4.1 and 4.2, respectively, focusing on the transient

regimes.

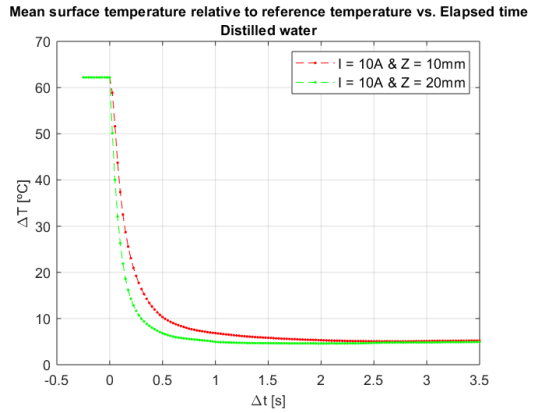

(a) Temporal evolution of mean surface temperature relative to reference temperature.

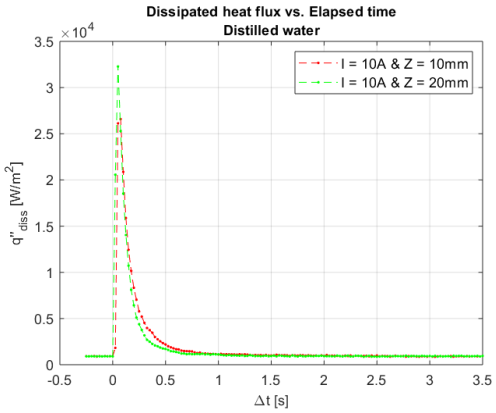

(b) Temporal evolution of dissipated heat flux.

Figure 4.3: Temporal evolution of the difference between mean surface temperature and reference temperature ΔT (Figure 4.3.a) and of the dissipated heat flux (Figure 4.3.b) for working conditions with imposed current $I = 10$ A in transient regime.

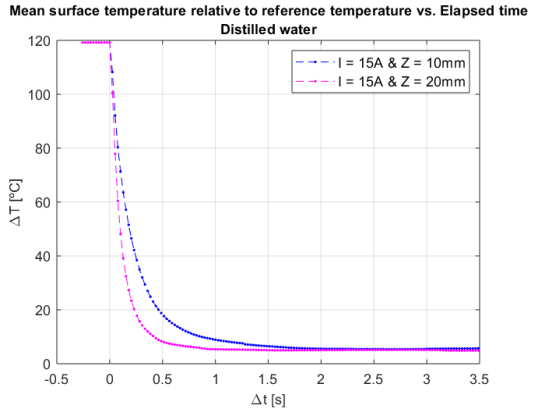

(a) Temporal evolution of mean surface temperature relative to reference temperature.

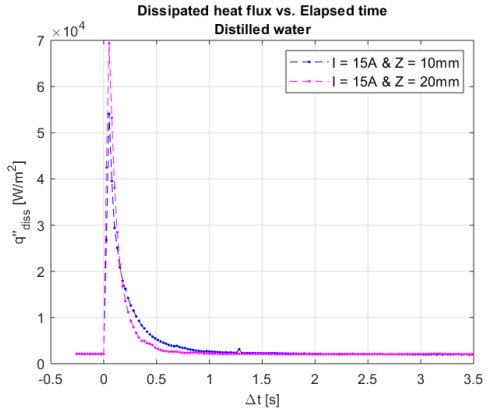

(b) Temporal evolution of dissipated heat flux on the surface.

Figure 4.4: Temporal evolution of the difference between mean surface temperature and reference temperature ΔT (Figure 4.4.a) and of the dissipated heat flux (Figure 4.4.b) for working conditions with imposed current $I = 15$ A in transient regime.

From comparing the plots presented in the previous Figures, it can be observed that when the atomizer is placed at a height of $Z = 20$ mm, the mean surface temperature decreases faster, thus the maximum heat flux is higher. As the temperature decreases faster, the steady-state regime is also reached sooner. Steady-state for $Z = 20$ mm starts approximately 1 second for $I = 10$ A and 1.5 seconds for $I = 15$ A sooner than for $Z = 10$ mm.

To better understand these differences in transient regimes between the two heights Z, the thermographic footprint and high-speed images are presented, for various instants, in Figures 4.5 and 4.6 for an applied current of 10 A and an atomizer height of 10 mm, and in Figures 4.7 and 4.8 for the same applied current and an atomizer height of 20 mm.

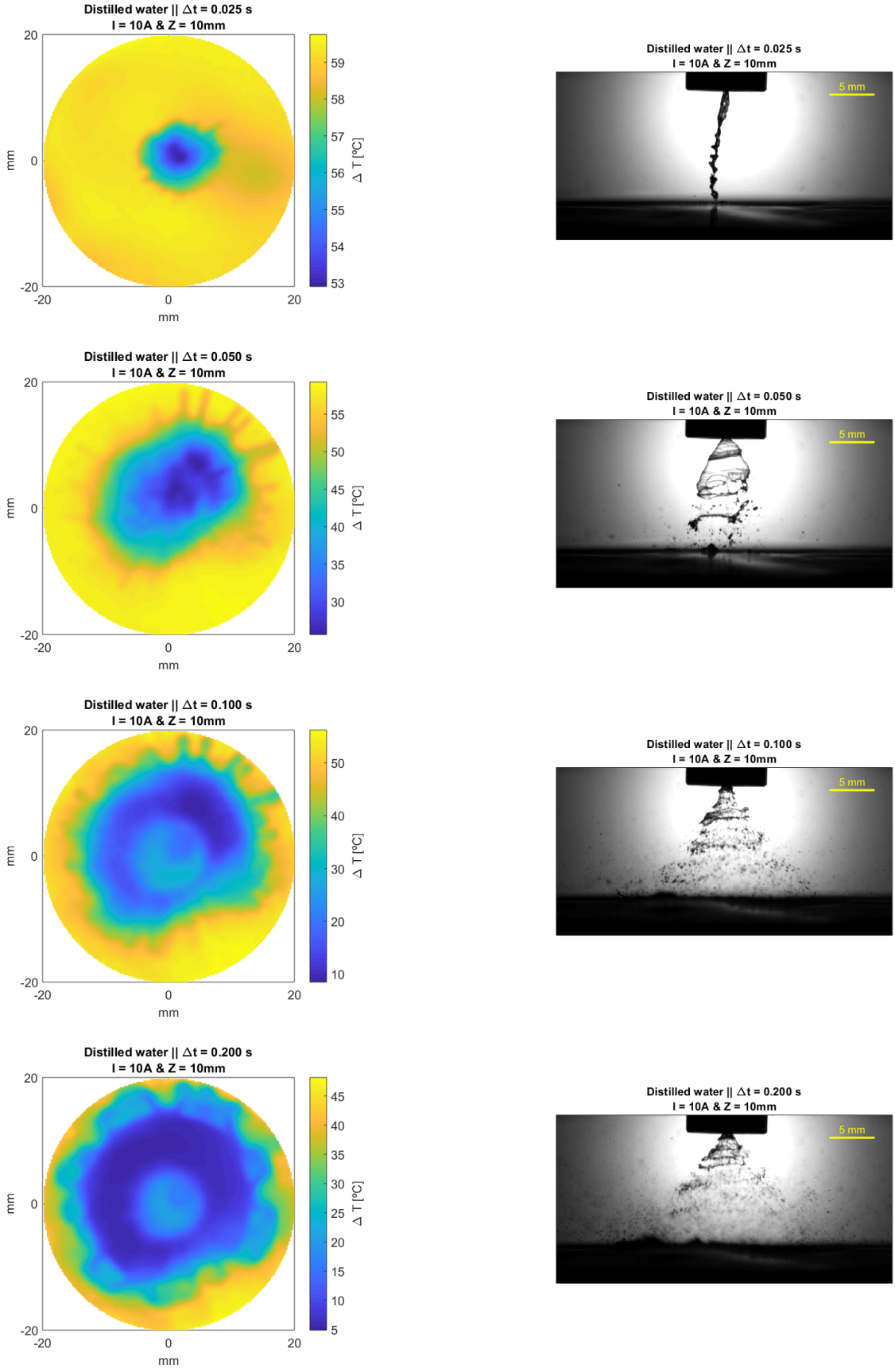

Figure 4.5: Transient regime thermographic and high-speed images for distilled water spray, with an applied current of 10 A and atomizer height of 10 mm for instants $\Delta t \in \{0.025, 0.050, 0.100, 0.200\}$ s.

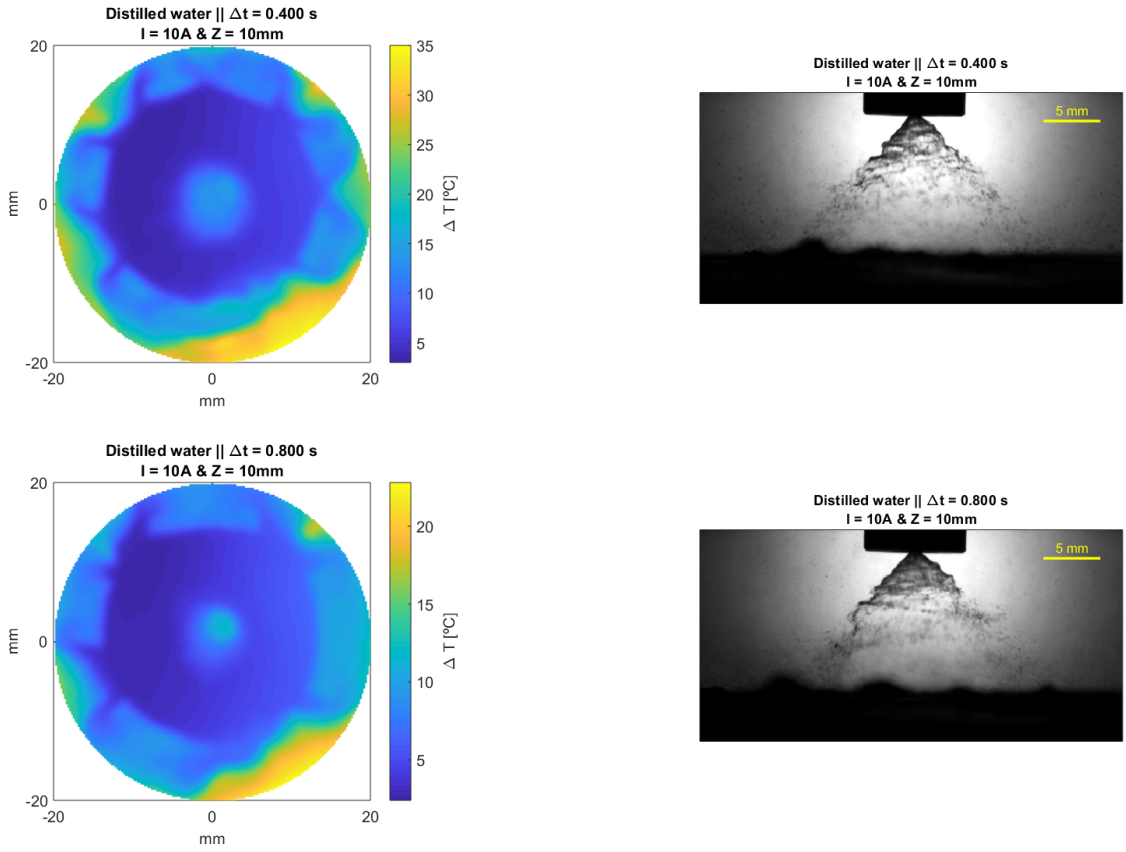

Figure 4.6: Transient regime thermographic and high-speed images for distilled water spray, with an applied current of 10 A and atomizer height of 10 mm for instants $\Delta t \in \{0.400, 0.800\}$ s.

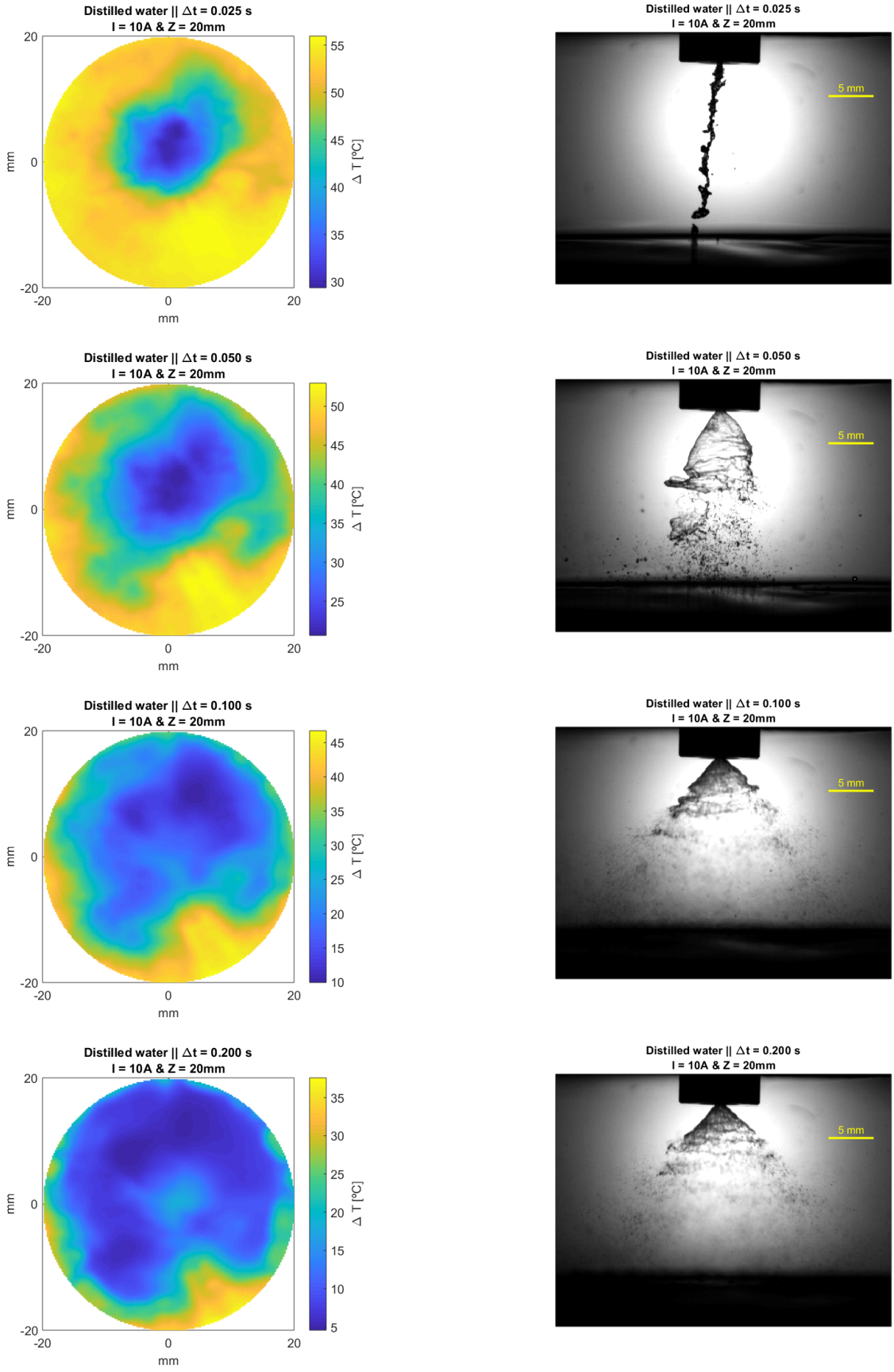

Figure 4.7: Transient regime thermographic and high-speed images for distilled water spray, with an applied current of 10 A and atomizer height of 20 mm for instants $\Delta t \in \{0.025, 0.050, 0.100, 0.200\}$ s.

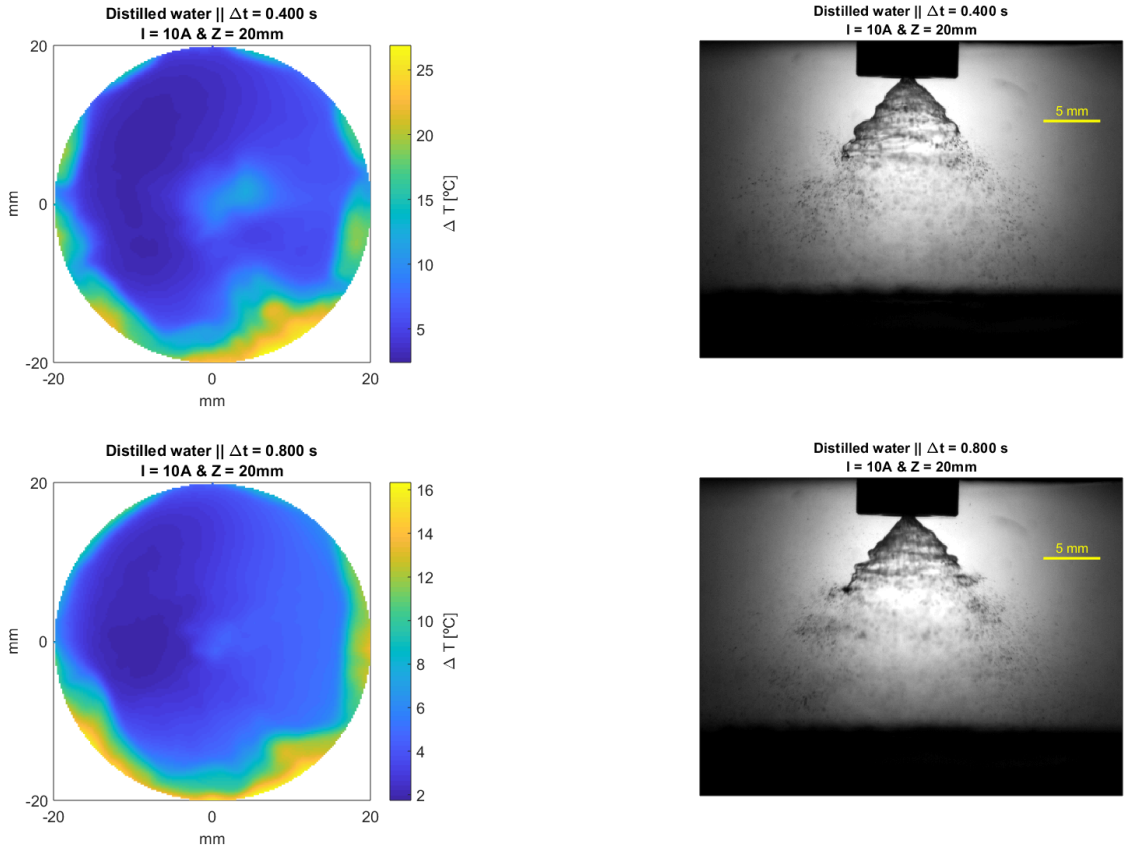

Figure 4.8: Transient regime thermographic and high-speed images for distilled water spray, with an applied current of 10 A and atomizer height of 20 mm for instants $\Delta t \in \{0.400, 0.800\}$ s.

From the high-speed images presented in the previous Figures, it can be observed that the spray takes approximately 0.800 s to become fully developed. It starts with a liquid jet impacting on the middle of the foil ($\Delta t = 0.025$ s). Thereafter, the hollow-cone shape liquid film starts to form at $\Delta t = 0.050$ s. For this instant, there can still be seen large continuous ligaments of liquid being released from the film. From $\Delta t = 0.100$ s, the spray acquires its final shape and finer droplets can already be seen. However, although the spray is fully developed, the thermographic footprints show that the foil temperature distribution has not stopped evolving. In fact, the temperatures continue to drop and the area with lower temperatures (coloured in dark blue) continues to increase. For the last instant presented of $\Delta t = 0.800$ s, it is noticeable how close the foil is in the $Z = 10$ mm case to the first break-up moment or the continuous ligaments of liquid, when compared to $Z = 20$ mm.

When comparing the high-speed images for instant $\Delta t = 0.800$ s, the spray shape does not seem to be affected by the height of the atomizer in relation to the foil. However, some significant changes can be seen in the thermographic footprints. These show that, when $Z = 20$ mm, the foil becomes wet faster than for $Z = 10$ mm. This has to do with the fact that, by placing the atomizer higher, the impact of the initial liquid jet will be much stronger, thus resulting in a faster spreading of liquid on the surface. Furthermore, for the subsequent instants, as the spray atomizer is placed higher, the spray cone is much more open when impacting the foil, resulting in a higher wetting area. These are the reasons why, as seen in Figures 4.3 and 4.4, the transient regime for $Z = 20$ mm is shorter than for $Z = 10$ mm.

For $Z = 10$ mm and starting at $\Delta t = 0.100$ s, a circular shape area with higher temperature can be seen in the middle of the foil. This area is a result of the hollow-cone shape of the spray and decreases in size in the subsequent instants. Whereas, for $Z = 20$ mm this area of higher-temperature area is only visible between $\Delta t = 0.200$ s and $\Delta t = 0.800$ s, where it is already hardly noticeable. Again, due to the hollow-cone shape and keeping in mind that, the further the atomizer is from the foil, higher the level of atomization, thus more small droplets which will move to the center area of the spray. This is why the center zone existence is much shorter in the $Z = 20$ mm case.

For an imposed current $I = 15$ A, the transient regimes for varying atomizer height are very similar to those obtained for $I = 10$ A. However, as will be seen in the steady-state analysis, for $I = 15$ A and $Z = 10$ A, the circular shape area with high temperature will not disappear. Figure 4.9 depicts the thermal footprint for distilled water spray at instant $\Delta t = 0.800$ s for an applied current of $I = 15$ A and a vertical distance of $Z = 10$ mm. The reason why for these specific conditions, the temperature in the center is higher, may be related with the high imposed heat flux and initial temperatures, which vaporizes the liquid in this area.

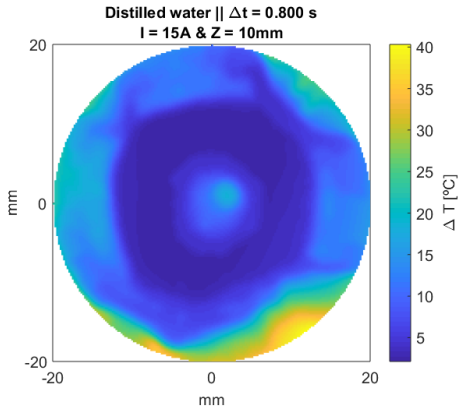

Figure 4.9: Thermographic footprint of distilled water spray at $\Delta t = 0.800$ s for an applied current of $I = 15$ A and a vertical distance of $Z = 10$ mm.

Distilled water spray: steady-state regime

Steady-state regime is characterized by no variation of the system properties with time. Figure 4.10 shows the thermographic footprints of the distilled water sprays in the different working conditions, defined in the beginning of this Chapter and in steady-state.

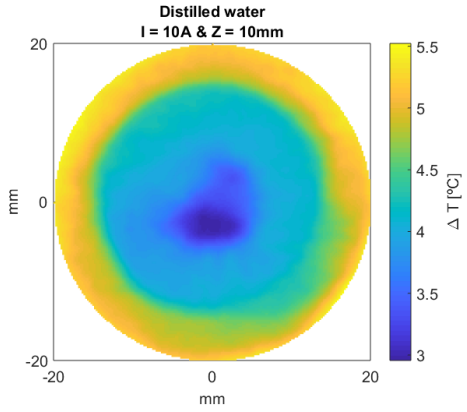

(a) Imposed current of $I = 10$ A and nozzle at $Z = 10$ mm.

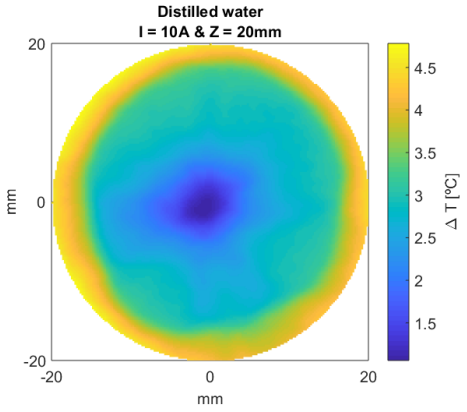

(b) Imposed current of $I = 10$ A and nozzle at $Z = 20$ mm.

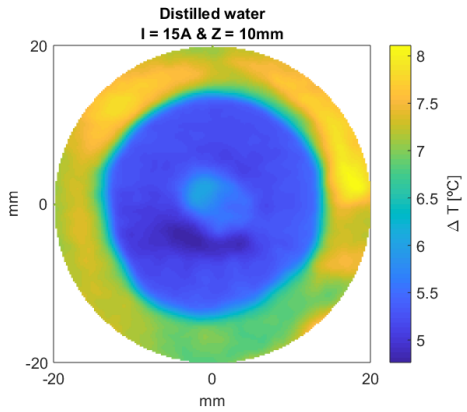

(c) Imposed current of $I = 15$ A and nozzle at $Z = 10$ mm.

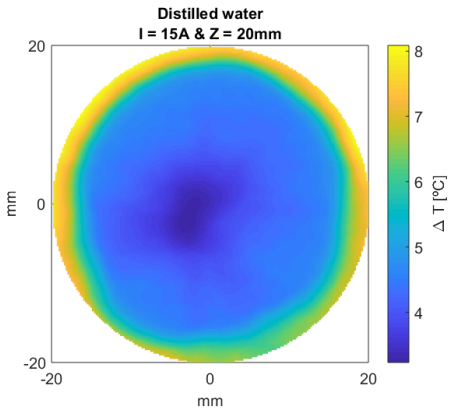

(d) Imposed current of $I = 15$ A and nozzle at $Z = 20$ mm.

Figure 4.10: Steady-state thermal footprints of distilled water sprays for the different working conditions.

Again, similarly to what was seen in the end of the transient regime, Figure 4.10 shows that, when $Z = 10$ mm, the spray impact area, corresponding to the area where the temperatures are lower which is represented in blue, is smaller than when $Z = 20$ mm. Furthermore, this area is not a perfect circle as one could expect, nor the temperature profile for constant radial distance is strictly constant with time. These irregularities are a result of imperfections in the spray droplet cloud and some undesired, but inevitable, wrinkles in the metallic foil. For this reason, the radial temperature profiles which will be presented in this analysis will be all computed as the mean of the profiles for eight radial directions (for azimuth angles of $\Phi \in \{0, 45, 90, 135, 180, 225, 270, 315\}^\circ$).

In Figure 4.11 the radial foil temperature profiles relative to the initial fluid temperature for distilled water sprays are combined according to the vertical distance between the spray nozzle and the foil Z namely: on the left side, for $Z = 10$ mm, and on the right side, for $Z = 20$ mm.

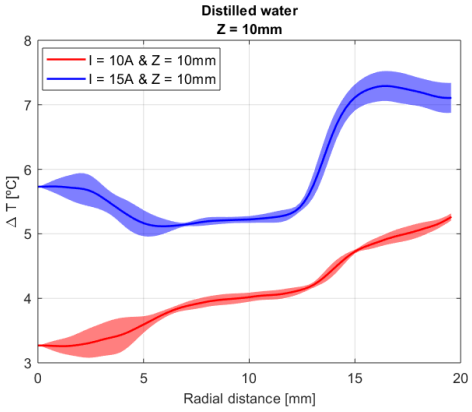

(a) Atomizer height $Z = 10$ mm.

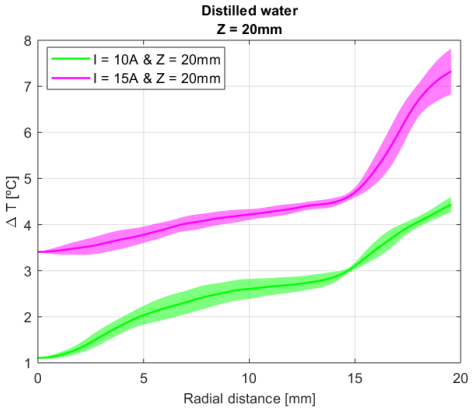

(b) Atomizer height $Z = 20$ mm.

Figure 4.11: Steady-state radial foil temperature profiles for distilled water sprays at same distance from the nozzle to the foil and varying imposed current.

The profiles for $I = 15$ A result in higher temperatures when comparing to the $I = 10$ A at the same height. The two curves on the right side, corresponding to $Z = 20$ mm, are similar, just a higher increase in temperature in the periphery is seen for $I = 15$ A as a result of the higher imposed heat flux. However, when comparing the curves for $Z = 10$ mm, $I = 10$ A and $I = 15$ A have no longer the same shape. For $Z = 10$ mm and $I = 10$ A, ΔT is not an increasing monotone function with the radial distance r and the minimum temperature of the profile doesn't occur at the center. The higher temperature in the center of foil for $Z = 10$ mm and $I = 15$ A is a result of the initial transient regime, as explained before, where the droplets impact a surface at 140 °C, which is well above water boiling point. These droplets bounce off the center of the foil due to boiling at the liquid-solid interface. At a distance of $Z = 10$ mm from the spray nozzle and due to its hollow-cone shape, the droplet cloud in the center is very sparse and the droplet velocity is, overall, dominated by the outwards radial component. As a result, the temperature at the center of the foil is higher in this case.

The limit of the spray impact area can be identified by the sudden increase in the temperature gradient and is more noticeable for the higher imposed heat flux cases. When $Z = 10$ mm, the limit is at approximately $r = 12$ mm and for $Z = 20$ mm, the spray impact area is larger, with the limit at approximately $r = 15$ mm.

In Figure 4.12 the radial foil temperature profiles for distilled water sprays are combined according to the input current I. On the left side, the cases with $I = 10$ A, and on the right side, the cases with $I = 15$ A.

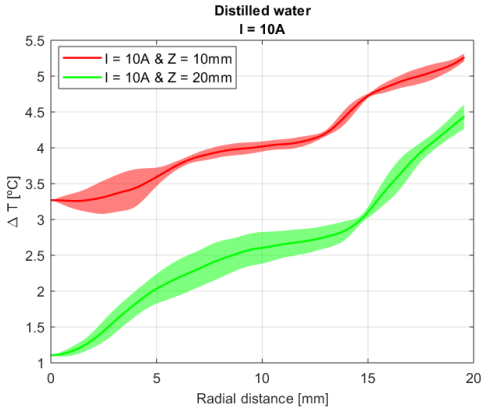

(a) Same imposed current $I = 10$ A.

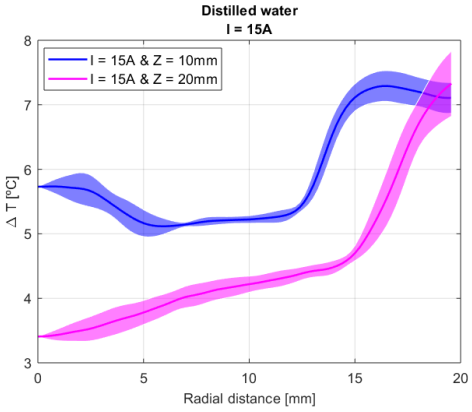

(b) Same imposed current $I = 15$ A.

Figure 4.12: Radial temperature profiles for distilled water sprays at same imposed current and varying distance from the nozzle to the foil.

Figure 4.12 shows that, for the same imposed current, the lower temperature profiles correspond to the situations of $Z = 20$ mm. When comparing $Z = 10$ mm with $Z = 20$ mm at same imposed heat flux, the maximum difference between the temperature profiles occurs at the center (for $r = 0$ mm) and is approximately 2 °C.

Table 4.1 shows, for distilled water spray in the different working conditions, the mean steady-state values for dissipated heat flux q''_{diss}, mean surface temperature relative to the reference temperature $\overline{\Delta T}$ and heat transfer coefficient h. The mean and standard deviation values are obtained from a circle with center in the axis of the spray and a radius 20 mm.

Table 4.1: Dissipated heat flux and heat transfer coefficient for water sprays in the different working conditions.

I [A]	Z [mm]	q''_{diss} [W/m^2]	$\overline{\Delta T}$ [°C]	h [W/(m^2.°C)]
10	10	895.71 ± 6.16	26.19 ± 0.03	34.20 ± 0.24
	20	903.98 ± 3.18	24.98 ± 0.01	36.18 ± 0.13
15	10	2010.14 ± 7.89	27.86 ± 0.05	72.14 ± 0.31
	20	2024.10 ± 6.33	27.29 ± 0.05	74.16 ± 0.27

Previous Table shows that the dissipated heat flux and relative mean surface temperature values are slightly higher for $Z = 10$ mm, in relation to the values for $Z = 20$ mm. As a consequence, the heat transfer coefficients for $Z = 20$ mm are higher, thus resulting in higher thermal performance.

4.2 Steady-state regime analysis

In this Section the steady-state regime for the different fluids is compared in terms of radial foil temperature profiles, as well as values of dissipated heat flux q''_{diss}, mean surface temperature in relation to the

reference temperature $\overline{\Delta T}$ and heat transfer coefficient h. These results are presented following the order of preparation of the nanofluids, with the objective of isolating the contributions of each component. Furthermore, the nanofluid analysis will be made comparing nanofluids with different concentrations of the same nanoparticle material (Section 4.2.2), different particle shapes (Section 4.2.3) and different substances but same mass concentration (Section 4.2.4).

4.2.1 Effect of adding CTAB

To understand the impact of adding cetyltrimethylammonium bromide (CTAB) to distilled water, this Section will focus on comparing distilled water with the base fluid spray (distilled water with 0.05% (m/m) CTAB).

In Figure 4.13, the surface temperature in relation to the reference temperature $\Delta T = T_{\mathrm{w}} - T_{\mathrm{ref}}$ is plotted as a function of radial distance to the center of the spray, for the base fluid and distilled water.

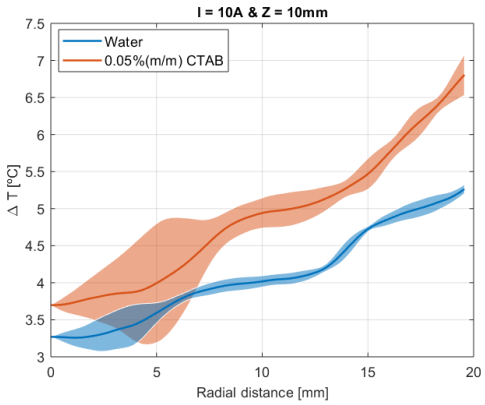

(a) Imposed current of $I = 10$ A and nozzle at $Z = 10$ mm.

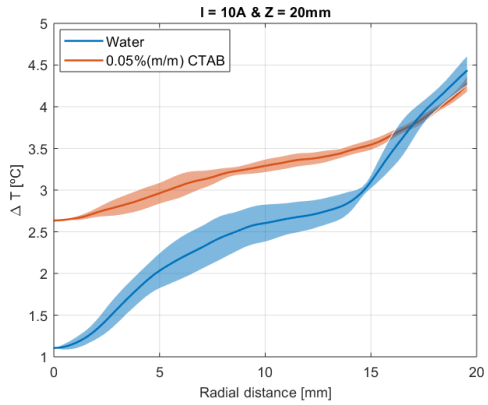

(b) Imposed current of $I = 10$ A and nozzle at $Z = 20$ mm.

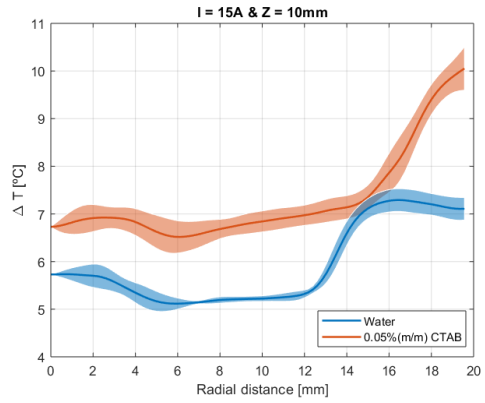

(c) Imposed current of $I = 15$ A and nozzle at $Z = 10$ mm.

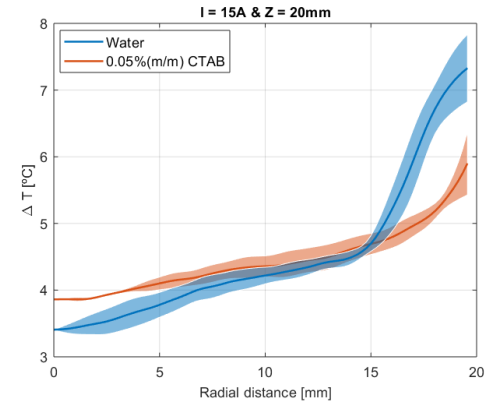

(d) Imposed current of $I = 15$ A and nozzle at $Z = 20$ mm.

Figure 4.13: Comparison of radial foil temperature profiles for distilled water spray and 0.05% (m/m) CTAB base fluid sprays.

Figure 4.13 shows that adding surfactant results in an increase of surface temperatures. For $Z = 10$ mm this increase is of about $1\ ^{\circ}\mathrm{C}$ in the center region of the spray, however in the periphery the

increase is higher, reaching $3\ ^{\circ}\mathrm{C}$. Considering now the situation with $I = 15$ A and $Z = 10$ mm, the maximum temperature difference from the base fluid to the water occurs at the center of the spray and, with the increase in radial distance, the temperature difference decreases. For the maximum working conditions, for $I = 15$ A and $Z = 20$ mm, the temperature increase is very small with the addition of CTAB.

The radial temperature plots also show that with CTAB, the increase in temperature which was verified at the limit of the spray impact area for water sprays (at approximately $r = 13$ mm for $Z = 10$ mm and $r = 15$ mm for $Z = 20$ mm) increases by 2 mm for $Z = 10$ mm and by 3 mm for $Z = 20$ mm with the addition of CTAB. This is a result of the increased wettability of the base fluid in relation to water, as a result of the lower contact angle (Table 3.11).

Table 4.2 are the mean steady-state regime values for the dissipated heat flux q''_{diss}, mean surface temperature in relation to the reference temperature $\overline{\Delta T}$ and the heat transfer coefficient h, for the 0.05% (m/m) CTAB base fluid.

Table 4.2: Steady-state mean dissipated heat flux q''_{diss}, mean surface temperature in relation to the reference temperature $\overline{\Delta T}$ and the heat transfer coefficient h for the base fluid.

I [A]	Z [mm]	q''_{diss} [W/m^2]	$\overline{\Delta T}$ [°C]	h [W/(m^2.°C)]
10	10	909.23 ± 3.35	27.08 ± 0.03	33.50 ± 0.13
	20	906.71 ± 5.33	25.69 ± 0.01	35.28 ± 0.21
15	10	2038.00 ± 7.16	29.77 ± 0.08	68.50 ± 0.30
	20	2034.33 ± 8.73	26.67 ± 0.03	76.16 ± 0.34

The values of dissipated heat flux q''_{diss} and heat transfer coefficient h in the different working conditions are plotted for water and base fluid in Figure 4.14.

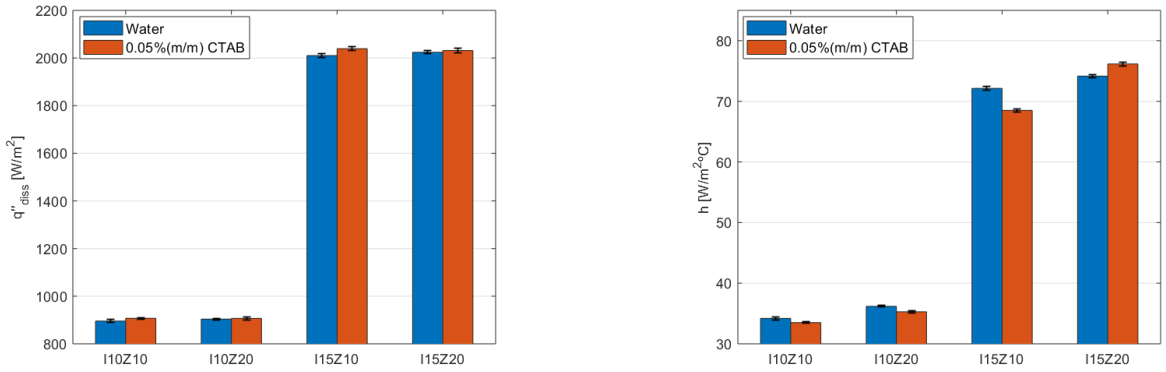

(a) Dissipated heat flux q''_{diss}.

(b) Heat transfer coefficient h.

Figure 4.14: Dissipated heat flux and heat transfer coefficient for water and base fluid sprays in the different working conditions.

Comparing values from Tables 4.1 and 4.2, as well as the plots in Figure 4.14, it can be seen that

adding CTAB results in an increase of the dissipated heat flux, of about 1.3% for $Z = 10$ mm and of 0.35% for $Z = 20$ mm. Furthermore, when comparing the relative mean temperature $\overline{\Delta T}$, it increases with CTAB for all situations, except for the maximum working conditions ($I = 15$ A and $Z = 20$ mm). The maximum increase occurs when $I = 15$ A and $Z = 10$ mm and is of approximately 6.9%. Finally, similarly to the temperature difference, the heat transfer coefficient decreases with the addition of CTAB, except for the maximum working conditions, where an increase of 2.7% is verified. The maximum decrease happens for $I = 15$ A and $Z = 10$ mm and is of approximately 5.1%.

The change in foil radial temperature profile shape with the addition of CTAB may be related with the increased wettability, which enhances the wetting over the foil. On the other hand, the increase in mean surface temperatures $\overline{\Delta T}$ is related with deterioration of thermophysical properties from the addition of the surfactant, namely thermal conductivity k and specific heat capacity c_p, as stated in Al-Waeli et al. [23], and increased dynamic viscosity μ (Table 3.10), which further deteriorates heat transfer by convection.

4.2.2 Effect of adding alumina nanoparticles

To study the difference, in terms of thermal characteristics of the spray with the variation of nanoparticle concentration, in this Section the base fluid is compared to the suspensions of water with CTAB and alumina (Al_2O_3) nanoparticles for mass concentrations of 0.5, 1 and 2% (m/m).

In Figure 4.15 the radial foil temperature profiles are presented for the base fluid and for the alumina nanofluids. In the vertical axis, the surface temperature is given in relation to the reference temperature ($\Delta T = T_{\mathrm{w}} - T_{\mathrm{ref}}$, $T_{\mathrm{ref}} = 21.82$ °C).

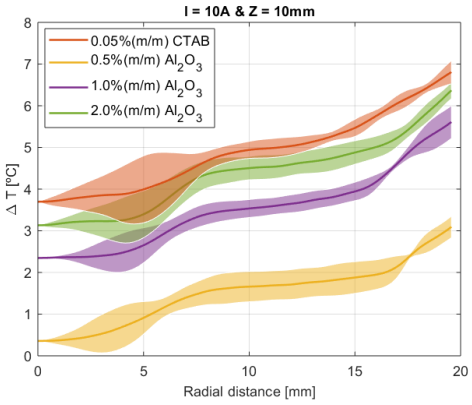

(a) Imposed current of $I = 10$ A and nozzle at $Z = 10$ mm.

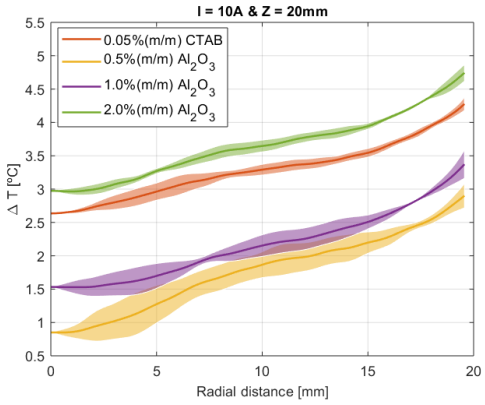

(b) Imposed current of $I = 10$ A and nozzle at $Z = 20$ mm.

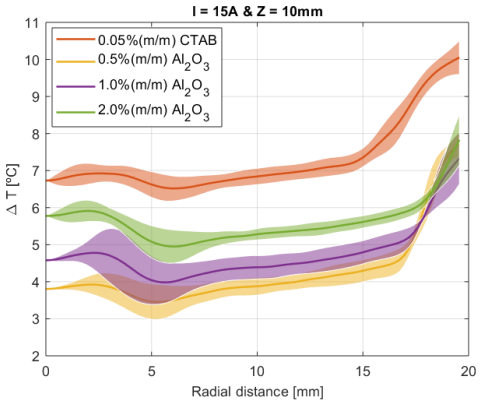

(c) Imposed current of $I = 15$ A and nozzle at $Z = 10$ mm.

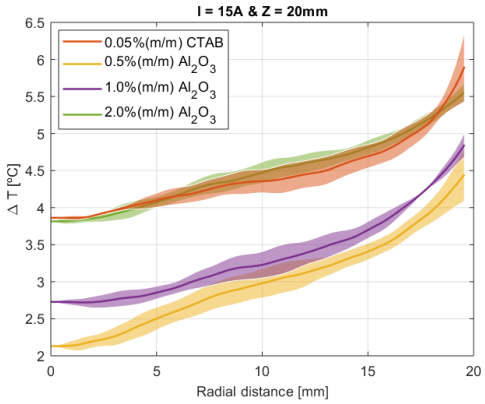

(d) Imposed current of $I = 15$ A and nozzle at $Z = 20$ mm.

Figure 4.15: Comparison of radial foil temperature profiles for the base fluid and the different alumina nanofluid sprays.

It is clear, from comparing the different temperature profiles in Figure 4.15, that the alumina 0.5% (m/m) nanofluid results, for all conditions, in lower ΔT. The highest temperatures are obtained for the base fluid or, when $I = 10$ A and $Z = 20$ mm, it is the alumina 2.0% (m/m) nanofluid which presents the highest temperatures. The increase of alumina nanoparticle concentration results in the displacement of the temperature profiles to higher temperatures.

Furthermore, it is worth noting that the shape of these profiles does not change with the addition of nanoparticles to the base fluid. The shape of the profiles is constant and only a vertical displacement in the ΔT axis is verified. This suggests that by adding the alumina nanoparticles, the dynamic properties of the spray are not greatly impacted, as could be expected from the negligible variations in surface tension and static contact angles with addition of these nanoparticles, seen in Table 3.10.

Table 4.3 are the mean steady-state values of dissipated heat flux q''_{diss}, mean surface temperature in relation to the reference temperature $\overline{\Delta T}$ and the heat transfer coefficient h for the alumina nanofluids.

Table 4.3: Steady-state mean dissipated heat flux q''_{diss}, mean surface temperature in relation to the reference temperature $\overline{\Delta T}$ and the heat transfer coefficient h for the alumina nanofluids.

I [A]	Z [mm]	Alumina content [%(m/m)]	q''_{diss} [W/m^2]	$\overline{\Delta T}$ [°C]	h [W/(m^2.°C)]
10	10	0.5	907.16 ± 3.50	24.23 ± 0.01	37.45 ± 0.15
		1	909.25 ± 3.95	25.83 ± 0.01	35.20 ± 0.15
		2	910.82 ± 3.80	26.75 ± 0.02	34.05 ± 0.14
	20	0.5	902.81 ± 3.95	23.81 ± 0.01	37.92 ± 0.17
		1	903.57 ± 4.09	24.44 ± 0.01	36.96 ± 0.17
		2	902.87 ± 4.02	25.56 ± 0.01	35.33 ± 0.16
15	10	0.5	2046.67 ± 7.04	26.57 ± 0.04	77.40 ± 0.29
		1	2042.88 ± 5.96	27.31 ± 0.03	74.81 ± 0.23
		2	2042.11 ± 7.84	27.65 ± 0.02	73.87 ± 0.29
	20	0.5	2019.65 ± 4.48	24.99 ± 0.01	80.81 ± 0.18
		1	2025.39 ± 4.55	25.40 ± 0.01	79.75 ± 0.18
		2	2022.01 ± 4.65	26.62 ± 0.01	75.95 ± 0.18

Figure 4.16 depicts the dissipated heat flux q''_{diss} and the heat transfer coefficients h obtained from the impact of the alumina nanofluid sprays which were summarized in Table 4.3, as well as, for the base fluid, from Table 4.2. These are plotted for the different working conditions.

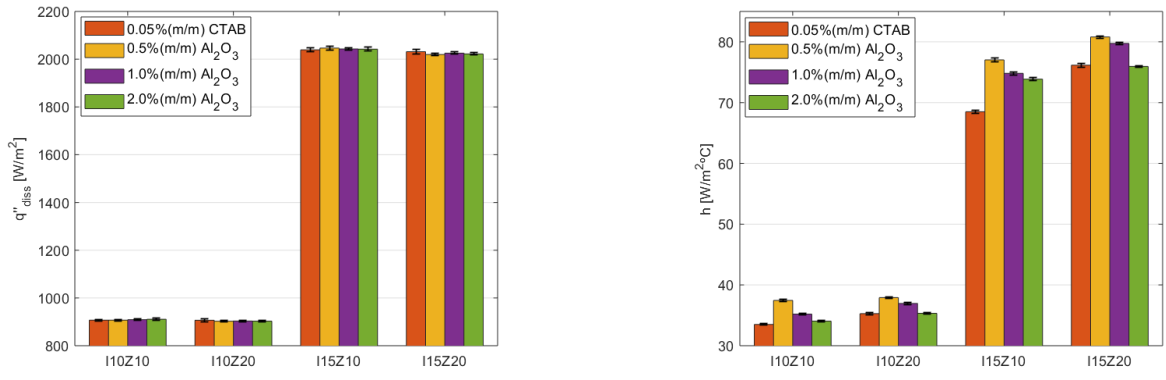

(a) Dissipated heat flux q''_{diss}.

(b) Heat transfer coefficient h.

Figure 4.16: Dissipated heat flux and heat transfer coefficient for alumina nanofluids and base fluid sprays in the different working conditions.

From both Table 4.3 and Figure 4.16.a it can be observed that there is not a monotone variation of the dissipated heat flux q''_{diss} with the nanoparticles concentration. For the $Z = 20$ mm conditions the maximum q''_{diss} is obtained for concentration 1% (m/m). For the $Z = 10$ mm and $I = 10$ mm the dissipated

heat flux increases with the increase of nanoparticle concentration, whereas for the maximum conditions ($Z = 20$ mm and $I = 15$ mm) the opposite occurs, i.e. with an increase of concentration, q''_{diss} decreases.

The mean surface temperature from Table 4.3 is in agreement with the results presented in the $\Delta T(r)$ plots from Figure 4.15. For all working conditions, with the increase of nanoparticle concentration, an increase in $\overline{\Delta T}$ is observed. These results show a very high positive correlation with the thermal conductivity (between 91.9% and 99.9%) and high negative correlation with the specific heat capacity (between -85.6% and -99.9%).

To better visualize the variation of the heat transfer coefficient h with alumina nanoparticle concentration, Figure 4.17 are the waterfall charts for each working condition. Green bars correspond to positive variations and red ones are negative variations. The blue bar at 0% (m/m) Alumina represents the heat transfer coefficient obtained for the base fluid (distilled water with 0.05% (m/m) CTAB).

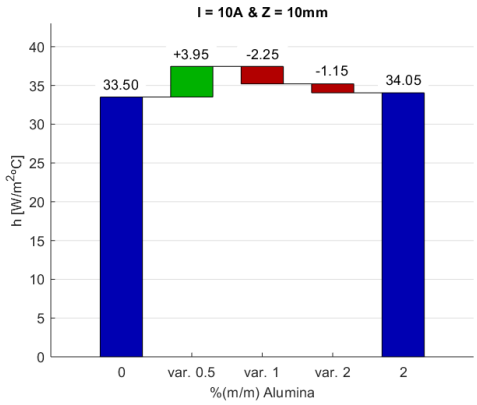

(a) Imposed current of $I = 10$ A and nozzle at $Z = 10$ mm.

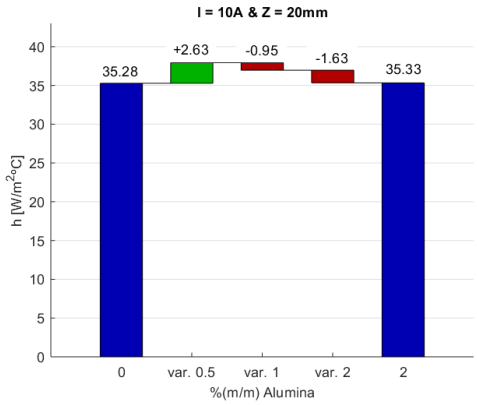

(b) Imposed current of $I = 10$ A and nozzle at $Z = 20$ mm.

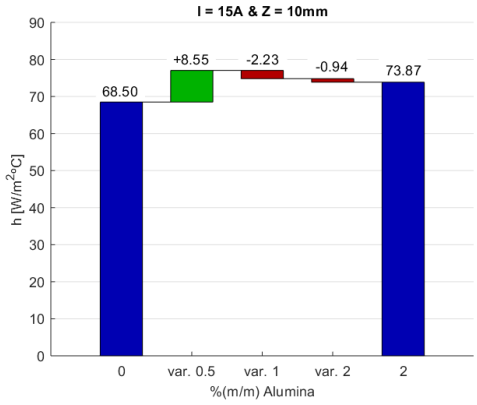

(c) Imposed current of $I = 15$ A and nozzle at $Z = 10$ mm.

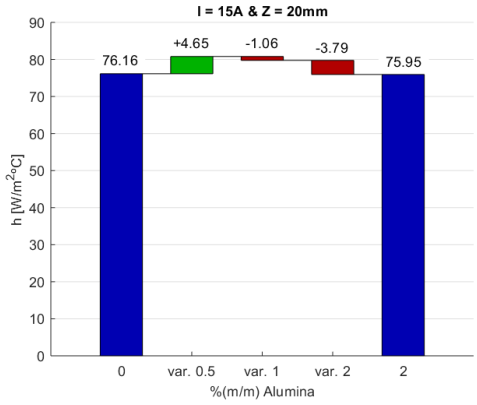

(d) Imposed current of $I = 15$ A and nozzle at $Z = 20$ mm.

Figure 4.17: Heat transfer coefficient h waterfall chart for varying alumina concentration.

Figure 4.17 shows that the heat transfer coefficient h increases in approximately 12% for $Z = 10$ mm and 6% for $Z = 20$ mm from the base fluid to the Alumina 0.5% (m/m). With the increase of alumina content, h tends to decrease and for both $Z = 20$ mm cases, h of alumina 2% (m/m) is very close to the one of the base fluid. Moreover, for $Z = 10$ mm the decrease in h from an alumina concentration of 0.5%

to 1% is twice the one from 1% to 2%. On the other hand, for $Z = 20$ mm, the decrease in h is higher from 1% to 2% than from 0.5% to 1%.

As a consequence of the correlations verified for $\overline{\Delta T}$ and given the fact that h is inversely proportional to $\overline{\Delta T}$, a strong negative correlation of h is observed with thermal conductivity (with correlation coefficients between -91.0% and -99.9%) and a strong positive correlation with specific heat capacity (from 84.5% to 99.9%). These correlations are stronger when $Z = 20$ mm than when $Z = 10$ mm.

4.2.3 Effect of adding silver nanoparticles

To compare the behavior of two different particle shapes of the same material, silver (Ag) spherical and triangular nanofluids were prepared. In this Section, the results for the silver nanofluids will be compared with the base fluid (distilled water with 0.05% (m/m) CTAB).

Figure 4.18 shows the radial foil temperature profiles for silver nanofluids and the base fluid in the different working conditions. The temperatures ΔT are plotted in the vertical axis and are relative to the reference fluid temperature ($\Delta T = T_{\mathrm{w}} - T_{\mathrm{ref}}$, where $T_{\mathrm{ref}} = 21.82\ ^{\circ}\mathrm{C}$).

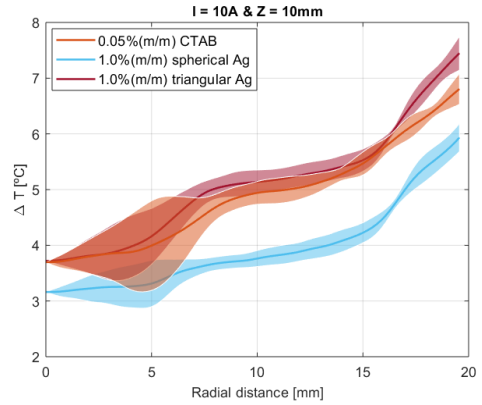

(a) Imposed current of $I = 10$ A and nozzle at $Z = 10$ mm.

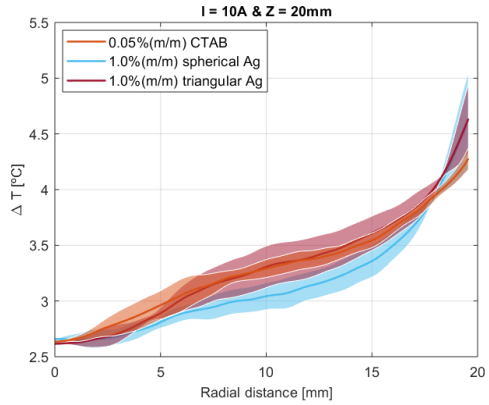

(b) Imposed current of $I = 10$ A and nozzle at $Z = 20$ mm.

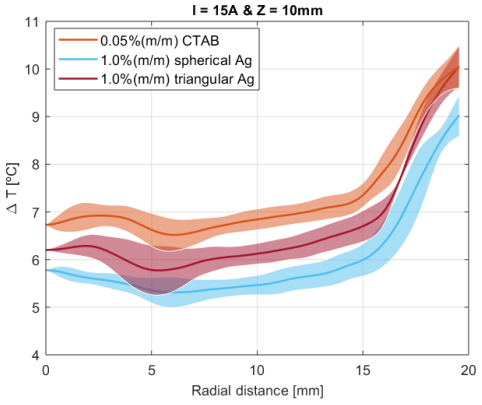

(c) Imposed current of $I = 15$ A and nozzle at $Z = 10$ mm.

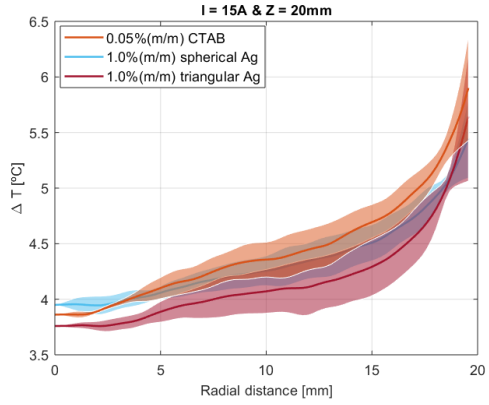

(d) Imposed current of $I = 15$ A and nozzle at $Z = 20$ mm.

Figure 4.18: Comparison of radial surface temperature profiles relative to reference fluid temperature for 0.05% (m/m) CTAB base fluid and the different silver nanofluid sprays.

In general, the base fluid has the highest temperatures. However, for the $I = 10$ A conditions, the surface temperatures obtained at the impact of triangular particle nanofluid spray overlap with those obtained for the base fluid spray impact. It is very clear that, when $Z = 10$ mm, the surface temperatures obtained for the spherical particle nanofluids are the lowest.

As was observed for the alumina nanofluids, adding the silver nanoparticles does not impact the shape of the temperature profiles, thus results only in a vertical displacement in the ΔT axis.

Table 4.4 shows the mean values in steady-state of dissipated heat flux q''_{diss}, mean surface temperature in relation to the reference temperature ΔT and the heat transfer coefficient h for the silver nanofluids in the different working conditions.

Table 4.4: Steady-state mean dissipated heat flux q''_{diss}, mean surface temperature in relation to the reference temperature $\overline{\Delta T}$ and the heat transfer coefficient h for the silver nanofluids.

I [A]	Z [mm]	Nanoparticle shape	q''_{diss} [W/m^2]	$\overline{\Delta T}$ [°C]	h [W/(m^2.°C)]
10	10	Spherical	909.05 ± 5.75	26.16 ± 0.02	34.75 ± 0.22
		Triangular	910.11 ± 4.55	27.26 ± 0.02	33.39 ± 0.17
	20	Spherical	907.55 ± 3.18	25.38 ± 0.02	35.75 ± 0.13
		Triangular	907.58 ± 5.54	25.71 ± 0.01	35.31 ± 0.22
15	10	Spherical	2035.34 ± 7.23	27.99 ± 0.07	72.72 ± 0.32
		Triangular	2037.43 ± 7.91	28.99 ± 0.07	70.28 ± 0.32
	20	Spherical	2029.24 ± 6.62	26.57 ± 0.04	76.36 ± 0.27
		Triangular	2026.31 ± 4.61	26.55 ± 0.01	76.31 ± 0.18

The values of the dissipated heat flux q''_{diss} and heat transfer coefficient h are plotted in Figure 4.19 for the silver nanofluids and for the base fluid sprays impacting on the smooth stainless steel surface.

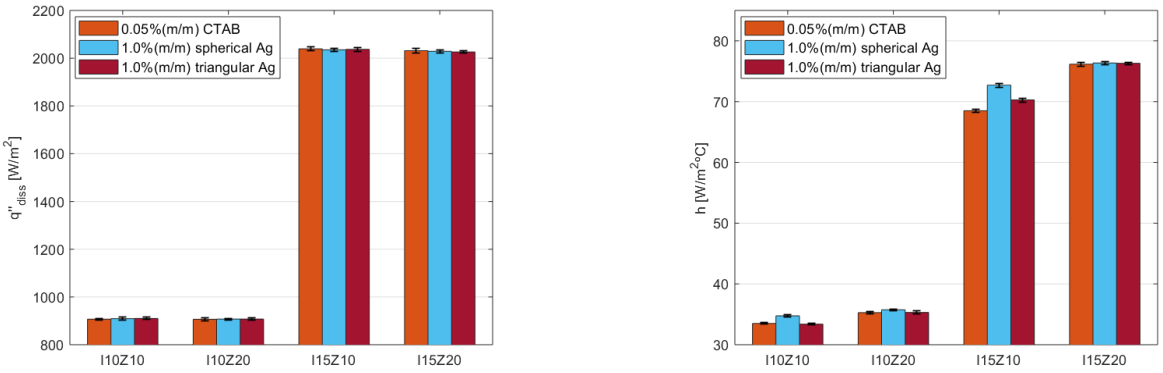

(a) Dissipated heat flux q''_{diss}.

(b) Heat transfer coefficient h.

Figure 4.19: Dissipated heat flux and heat transfer coefficient for silver nanofluids and base fluid sprays in the different working conditions.

Comparing the results for the dissipated heat flux q''_{diss} with the base fluid, from Table 4.2, and with the silver nanofluids, from Table 4.4, an increase is observed for dissipated heat flux for the silver nanofluids when $I = 10$ A and a decrease when $I = 15$ A.

From Figure 4.19.b it can be observed that, in all working conditions, the spherical silver nanofluid leads to the highest heat transfer coefficients. This is more notorious for $Z = 10$ mm cases than for $Z = 20$ mm.

4.2.4 Comparison of different nanofluids at same nanoparticle concentration

In this Section, the analysis will focus on the comparison of the nanofluids which were prepared using the same nanoparticle concentration of 1% (m/m). Thus, the results for the alumina 1% (m/m) and the two silver nanofluids will be compared and discussed.

Figure 4.20 are the radial foil temperature profiles, in terms of surface temperature relative to the reference fluid temperature, for the alumina 1% (m/m) nanofluid and for both silver nanofluids, in the different working conditions.

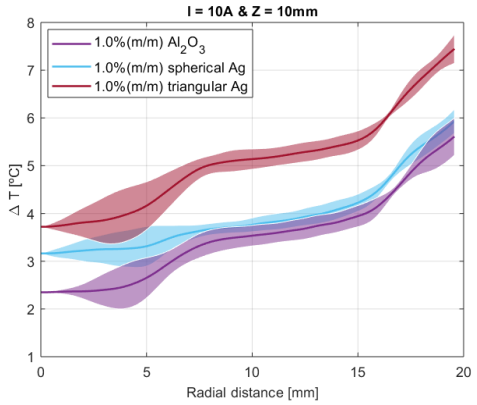

(a) Imposed current of $I = 10$ A and nozzle at $Z = 10$ mm.

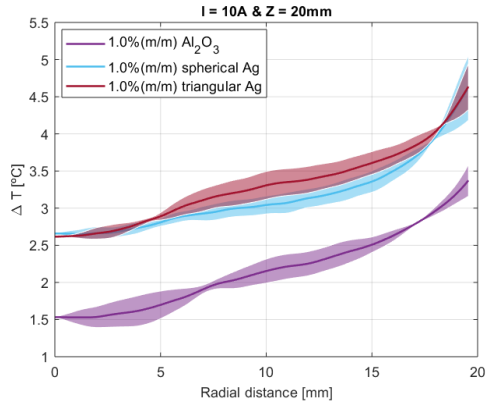

(b) Imposed current of $I = 10$ A and nozzle at $Z = 20$ mm.

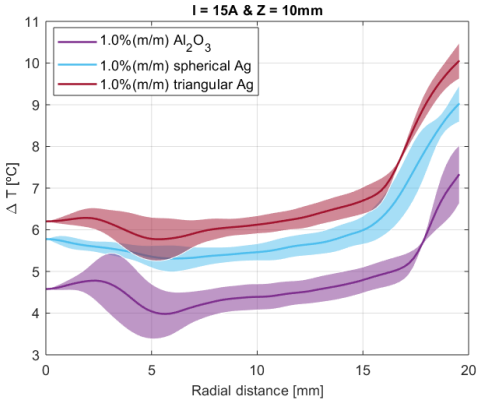

(c) Imposed current of $I = 15$ A and nozzle at $Z = 10$ mm.

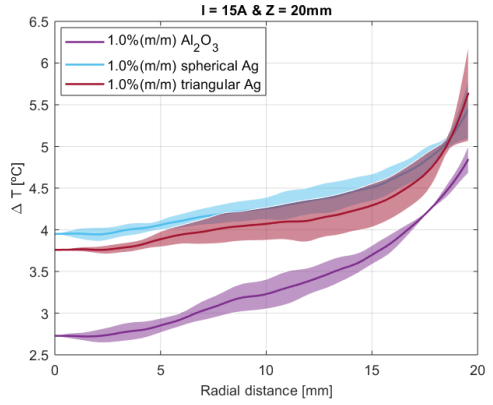

(d) Imposed current of $I = 15$ A and nozzle at $Z = 20$ mm.

Figure 4.20: Comparison of radial temperature profiles for the nanofluid sprays at 1% (m/m) concentration.

The previous Figure shows that the lowest temperatures are always verified for the alumina nanofluid, whereas, in general, the triangular silver nanofluid spray leads to the highest surface temperatures. When $Z = 20$ mm, the surface temperatures obtained at the impact of the alumina nanofluids are approximately 1 °C lower than those obtained with the silver nanofluids. The poorer performance of the silver nanofluids may be related with the much higher dynamic viscosity of these fluids compared to alumina nanofluid, Table 3.10.

4.2.5 Overall comparison of the different fluids

In this Section all fluids are considered and a global comparison is made. Figure 4.21 are the radial foil temperature profiles relative to the reference temperature for all fluids.

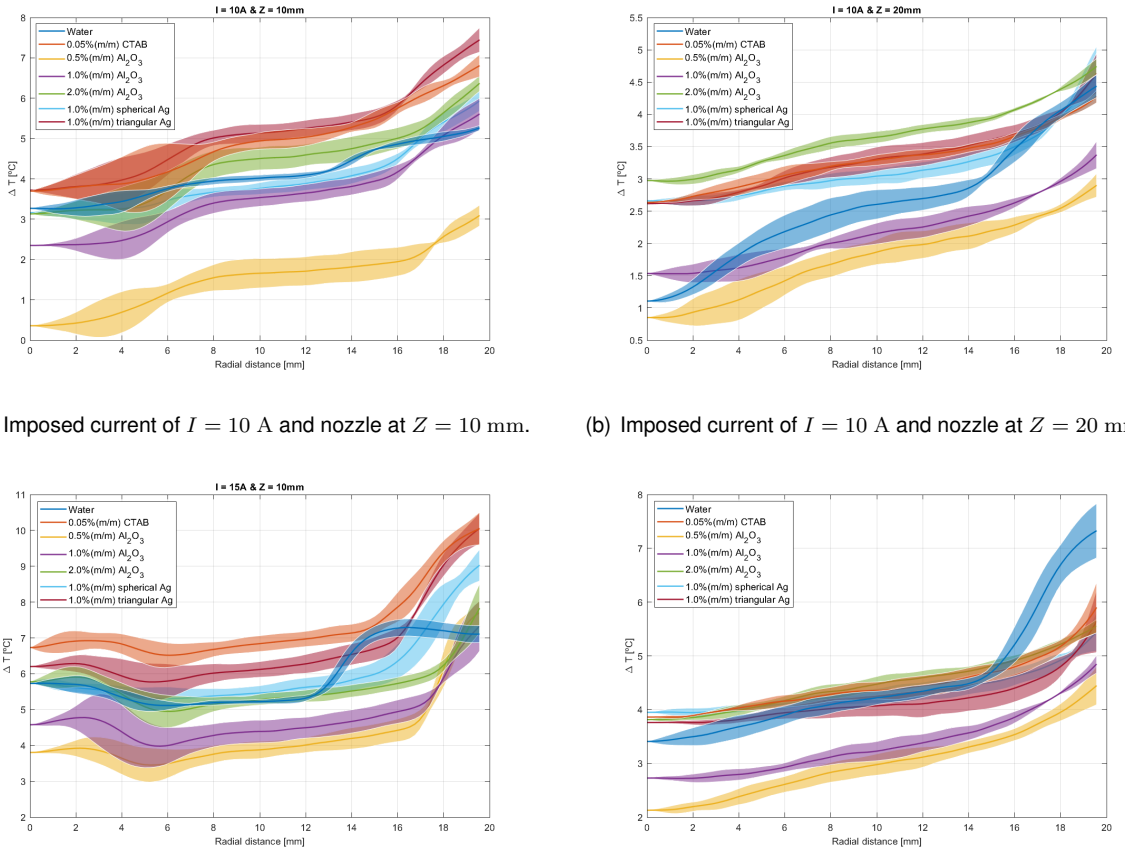

(a) Imposed current of $I = 10$ A and nozzle at $Z = 10$ mm.

(b) Imposed current of $I = 10$ A and nozzle at $Z = 20$ mm.

(c) Imposed current of $I = 15$ A and nozzle at $Z = 10$ mm.

(d) Imposed current of $I = 15$ A and nozzle at $Z = 20$ mm.

Figure 4.21: Radial foil temperature profiles relative to reference temperature for all fluids.

From the previous Figure it can be observed that the alumina 0.5% (m/m) nanofluid leads to the lowest surface temperatures for all working conditions. For $I = 10$ A and $Z = 10$ mm, the difference to the fluid leading to the second lowest temperature profile, which is the alumina 1% (m/m), is of 2 °C. The highest surface temperatures are generally obtained for the base fluid, triangular silver nanofluid, 2% (m/m) alumina or water, depending on the working conditions.

In general, the alumina nanofluids lead to lower surface temperature profiles than those obtained for

the silver nanofluid sprays. Temperatures lower than those observed with water tend to occur only for 0.5% and 1% (m/m) alumina and for spherical silver nanofluids.

The following Figures 4.22, 4.23 and 4.24 correspond to the plots of heat transfer coefficient h, as a function of nanofluid properties, respectively, specific heat capacity c_p, thermal conductivity k and dynamic viscosity μ.

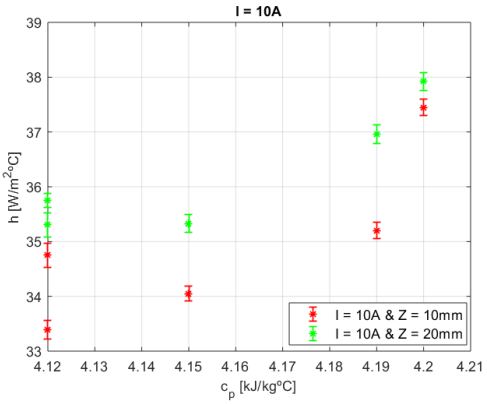

(a) $I = 10$ A.

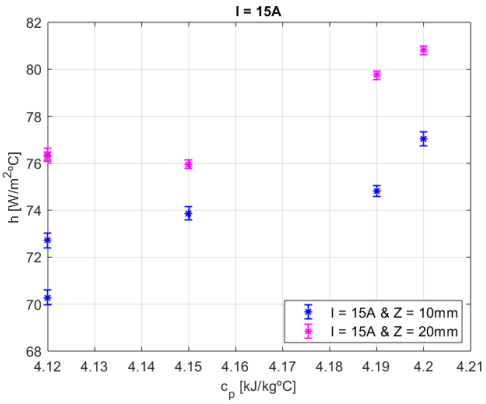

(b) $I = 15$ A.

Figure 4.22: Heat transfer coefficient h as a function of specific heat capacity c_p of the nanofluids.

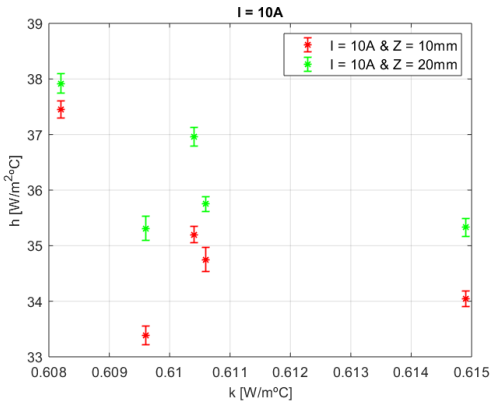

(a) $I = 10$ A.

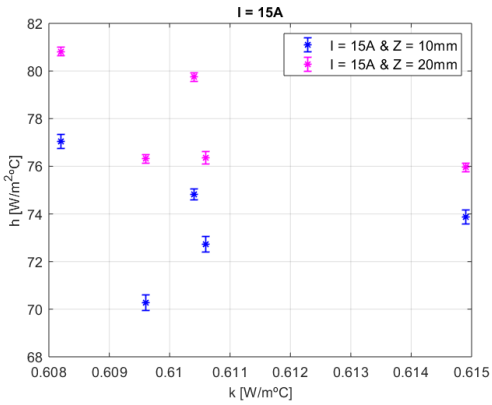

(b) $I = 15$ A.

Figure 4.23: Heat transfer coefficient h as a function of thermal conductivity k of the nanofluids.

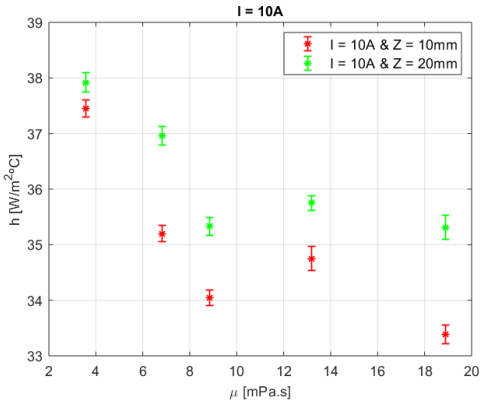

(a) $I = 10$ A.

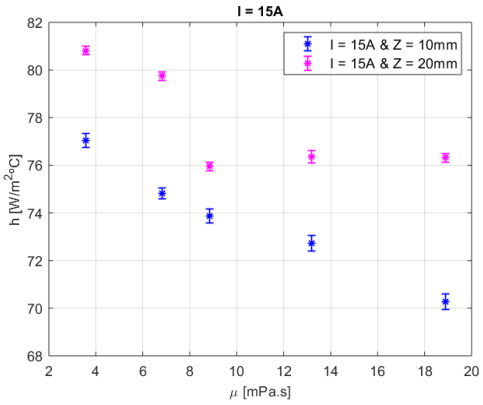

(b) $I = 15$ A.

Figure 4.24: Heat transfer coefficient h as a function of dynamic viscosity μ of the nanofluids.

Figure 4.22 shows a high positive correlation of the heat transfer coefficient h with the specific heat capacity c_p of the fluids, i.e. as the specific heat capacity increases, the heat transfer coefficient tends to increase. However, when considering the heat transfer coefficient as a function of thermal conductivity k of the fluid, Figure 4.23, these show some negative correlation. As seen in Table 3.8, for the fluids considered in this study, as the specific heat capacity increases, the thermal conductivity decreases, thus the optimal fluids in terms of heat transfer coefficient, tend to be those with high specific heat capacity and low thermal conductivity. Consequently, for the working conditions considered in this study, the dominant heat transfer mechanism is convection.

Figure 4.24 shows that, as the dynamic viscosity μ increases, the thermal performance decreases. Increased viscosity of the fluids hampers convection heat transfer, as well as, fluid flow on the surface.

4.3 Nanofluid stability

In practical engineering applications of spray cooling, to consider the implementation of nanofluids, thermal performance is not the only concern. Nanofluid stability is important to keep the cooling systems operating under constant conditions and avoid clogging. For that, in this Section, the results of a simple visual inspection of the nanofluids is presented. This analysis consisted of periodic visual inspections of the nanofluids since preparation, left at rest, inside small closed containers.

Figure 4.25 correspond to photographs of the alumina and silver nanofluids immediately after preparation.

(a) Alumina 0.5% (m/m).

(b) Alumina 1.0% (m/m).

(c) Alumina 2.0% (m/m).

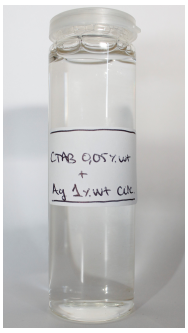

(d) Silver spherical 1.0% (m/m).

(e) Silver triangular 1.0% (m/m).

Figure 4.25: Nanofluids immediately after preparation.

The nanoparticles of silver, once prepared and in contact with air, start immediately oxidizing, thus resulting in the formation of silver oxide which starts to precipitate, as can be seen in Figure 4.26. This reaction is faster if the nanofluid is stored in a place with strong light and high temperatures.

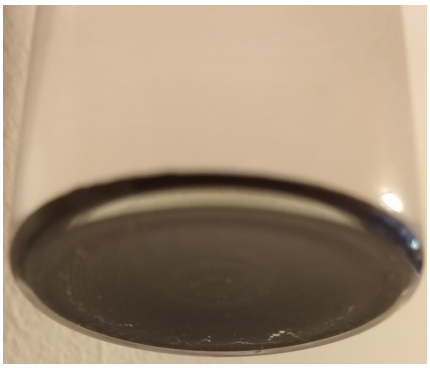

Figure 4.26: Precipitate of silver oxide in the silver nanofluids.

Alumina nanofluids are chemically stable. Only gravitational precipitation of the particles is observed for times at rest greater than 48 hours. Figure 4.27 are the alumina nanofluids after 48 hours at rest.

Figure 4.27: Precipitate in alumina nanofluids after 48 hours at rest.

Chapter 5

Conclusions

5.1 Final remarks

The aim of this work was to study the use of nanofluids in spray cooling of solid heated surfaces. Nanofluids were compared in terms of particle mass concentration, particle shape and particle material, with plain water and then with the base fluid (water with 0.05% (m/m) cetyltrimethylammonium bromide (CTAB)). Moreover, the impact of adding the surfactant, in this case CTAB, was isolated and identified.

Characterization of nanofluid thermophysical properties showed an increase in thermal conductivity and dynamic viscosity with the addition of more nanoparticles. On the other hand, the specific heat capacity decreased with the increase in nanoparticles concentration. Addition of the surfactant drastically reduced the surface tension to half the one of water. With the addition of nanoparticles the surface tension increased slightly. Similarly to the surface tension, the contact angle of the base fluid was half the one of water, revealing significantly better wettability. The contact angle with nanoparticles increases slightly when compared to the base fluid. These changes in fluid properties were seen to have negligible impact on the spray atomization, but high impact on the dynamics of the fluid over the foil and heat transfer performance.

For the two atomizer heights Z studied ($Z = 10\ \mathrm{mm}$ and $Z = 20\ \mathrm{mm}$) was seen that the most effective is the highest, i.e. $Z = 20\ \mathrm{mm}$. For both input currents, $Z = 20\ \mathrm{mm}$ resulted in higher dissipated heat fluxes, of approximately $10\ \mathrm{W/m^2}$ for water, and lower temperatures. This resulted in a heat transfer coefficient increase, from $Z = 10\ \mathrm{mm}$ to $Z = 20\ \mathrm{mm}$, of about $2\ \mathrm{W/(m^2.^\circ C)}$ for water spray.

When isolating the effect of adding the surfactant, in this case cetyltrimethylammonium bromide (CTAB), the thermal performance decreased. This trend was mostly observed by an increase in radial temperatures with the addition of CTAB. Except for the maximum working conditions, of $Z = 20\ \mathrm{mm}$ and $I = 15\ \mathrm{A}$, the heat transfer coefficient of water was higher than the one of the base fluid. Due to lack of data on thermophysical properties of CTAB, the thermal conductivity and specific heat capacity of the base fluid were not calculated. However, these results show good agreement with the data available in literature where surfactants are said to reduce thermal performance. Moreover, a notorious change in the shape of radial temperatures profiles can be observed. This has to do with the enhanced wettability

from decrease in contact angles.

Adding alumina (Al_2O_3) nanoparticles was seen to increase the thermal performance of the spray cooling system. However, contrarily to the results suggested in the literature, for the range of concentrations used, the increase of nanoparticle concentration resulted in worse thermal performance. In fact, the highest heat transfer coefficients were observed for the smallest alumina nanoparticle concentration of 0.5% (m/m) and, for both $Z = 20$ mm conditions, the heat transfer coefficient of 2% (m/m) alumina nanofluid was very close to the one of the base fluid. This result contradicts the increase in thermal conductivity, which is given in literature as main cause for the heat transfer enhancement of nanofluids. The decrease in thermal performance is coincident with the decrease in specific heat capacity of the fluid. Hence, for the conditions of this work and assuming that the thermal performance is a monotone function with the thermophysical properties of the nanofluids, the optimal mass concentration of alumina is expected to be lower or equal than 0.5% (m/m).

When considering different nanoparticle shapes, in this case studied by comparing two silver nanofluids, one of spherical and the other of triangular nanoparticles, was observed that it does not have a great impact on heat transfer performance. Both nanofluids showed smaller temperatures than the base fluid. However, for $Z = 10$ mm conditions, the fluid with spherical nanoparticles had a 2 W/(m^2.°C) higher heat transfer coefficient. Apart from the higher thermal conductivity of the spherical nanoparticles, this result may also be a consequence of the interaction between the particles and the foil, resulting in higher depositions.

For the 1% (m/m) nanofluids, alumina was the one which depicted better thermal performance. For $Z = 20$ mm this difference was the most notorious, as the temperature differences were of approximately 1 °C. This result is again contrary to the thermal conductivity increase, as the thermal conductivity of silver is higher than that of alumina. Dynamic viscosity of the silver nanofluids was twice the one of the 1% (m/m) alumina nanofluid, which may explain these differences. Moreover, even though the experiments were performed inside the supposed stability time interval after preparation of the silver nanofluids, these fluids deteriorate very fast under certain conditions, which may have further contributed to such differences.

Table 5.1 shows a summary of the properties and obtained heat transfer coefficients for each fluid. Overall, the 0.5% (m/m) alumina nanofluid was the one with highest heat transfer coefficients for all working conditions. For the conditions of $I = 10$ A and for $I = 15$ mm and $Z = 10$ mm, the obtained values of heat transfer coefficient are very similar. However, for $I = 15$ mm and $Z = 20$ mm showed an 8% increase of the heat transfer coefficient from water to 0.5% (m/m) alumina. For these conditions all nanofluids had heat transfer coefficients higher than that of water.

Alumina nanofluids were found to be very stable for the concentrations used and the amount of CTAB in the base fluid. Precipitation of the nanoparticles was just observed for times at rest longer than 48 hours. After this, with some ultrasonic sonication the homogeneity is restored and the fluid is ready to use again. In a practical application, most probably the fluid would be circulating in some closed loop which would by itself guarantee the homogeneity of the alumina emulsions. On the other hand, silver nanoparticles are chemically very unstable and react to form silver oxide. This problem, added to the

fact that silver is very expensive, is a big restriction for real applications of this kind of nanofluids.

Nanofluids have proved to enhance the heat transfer performance of spray cooling and, for the operating conditions used in this study, convection was identified as the main heat transfer mechanism. Increasing nanoparticle concentrations above certain value has a negative impact on thermal performance, with specific heat capacity decrease and dynamic viscosity increase being the main contributing parameters.

Infrared thermography (IR) was found to be an extremely powerful data acquisition system with high spatial and temporal resolution. It allowed to visualize the phenomena in great detail, as 2D distributions of temperatures and heat fluxes, in a way that thermocouples would not allow.

This work was submitted to the 2021 ICLASS conference (International Conference on Liquid Atomization and Spray Systems).

5.2 Future Work

For future developments in this area, the support system of the foil should be redesigned. Due to the differences in thermal expansion coefficients between copper of the electrical contacts and steel of the foil, big wrinkles were observed in the heated foil. These wrinkles were a result, not only of the different thermal expansion coefficients, but also of the contraction of the weld after welding the contacts. During the development of this dissertation a new prototype of the support system was built, using springs, which gave the foil a degree of freedom in expansion. However, the use of high-temperature silicone to glue the foil to the support was not effective, thus was reverted to the design of Figueiredo [56]. New support designs and ways of connecting the electrical contacts (which could involve the use of clamps) should be investigated.

All nanofluids in this study were prepared using mass concentration, which compared to the same volume concentration, result in lower nanoparticle content. This was due to frequent clogging of the atomizer for high nanoparticle concentration fluids. However, concentrations in literature are many times referred in volume base. Similarly to what was done in this dissertation when comparing nanofluids with same mass concentration but different nanoparticle materials, in future works the same could be done comparing nanofluids with the same volume concentration and different materials.

Quantitative studies of nanofluid stability should be performed, to further characterize the nanofluids. These studies should be performed with the aim of determining the time frame of stability of the different nanofluids, which is very relevant for practical applications of spray cooling. Moreover, as seen for the silver nanofluids, these are subjected to high oxidation which deteriorates the fluid. Therefore, the use of anti-corrosive additives could be explored as a way of stopping corrosion of these fluids.

Given the disagreement in the increase of alumina nanoparticle concentration and thermal performance, the optimal mass concentration of alumina should be explored. As the tendency is of thermal performance decrease with increasing nanoparticle concentrations, new experiments should be performed for low mass concentrations (assuming non-linear relationship of thermal performance with nanoparticle concentration, alumina concentrations lower than 1.0% (m/m) should be tested).

As seen in Table 5.1, for higher input currents the differences between fluids tend to be higher. Moreover, the results obtained in this work suggest that having the nozzle at an higher height results in significantly better thermal performance. In this context, future studies should consider the use of higher input currents and higher nozzle heights to further understand these dependencies and optimize this parameters.

Finally, deposits of nanoparticles on the test surface after spraying should be looked for, using Transmission Electron Microscopy (TEM), and their location compared with dissipated heat maps obtained from thermography. Many authors in literature have explored these deposits and they may be an additional mechanism of heat transfer in nanofluid spray cooling.

Table 5.1: Overall comparison of the properties of the fluids and heat transfer coefficients. Where ρ is the fluid density, c_p is the fluid specific heat capacity, k is the fluid thermal conductivity, μ is the dynamic viscosity, σ is the surface tension, θ is the static contact angle, h is the heat transfer coefficient, Z is the height of the atomizer relative to the surface and I is the input current.

Fluid	ρ [g/cm^3]	c_p [kJ/(kg.K)]	k [W/(m.K)]	μ [mPa.s]	σ [mN/m]	θ [°]	h [W/(m^2.°C)]			
							$I = 10$ A		$I = 15$ A	
							$Z = 10$ mm	$Z = 20$ mm	$Z = 10$ mm	$Z = 20$ mm
Water	0.9982	4.22	0.6060	1.009	74.5980 ± 2.2223	86.4741 ± 6.4139	34.20 ± 0.24	36.18 ± 0.13	72.14 ± 0.31	74.16 ± 0.27
Base fluid	0.9987	*	*	1.291	35.9201 ± 0.9189	53.5818 ± 6.3270	33.50 ± 0.13	35.28 ± 0.21	68.50 ± 0.30	76.16 ± 0.34
0.5% (m/m) Al_2O_3	1.0024	4.20	0.6082	3.572	39.0268 ± 1.2679	61.8037 ± 2.8827	37.45 ± 0.15	37.92 ± 0.17	77.40 ± 0.29	80.81 ± 0.18
1.0% (m/m) Al_2O_3	1.0062	4.19	0.6104	6.815	40.1761 ± 2.6986	59.8934 ± 2.6986	35.20 ± 0.15	36.96 ± 0.17	74.81 ± 0.23	79.75 ± 0.18
2.0% (m/m) Al_2O_3	1.0108	4.15	0.6149	8.835	40.2364 ± 0.8586	57.8884 ± 11.2754	34.05 ± 0.14	35.33 ± 0.16	73.87 ± 0.29	75.95 ± 0.18
1.0% (m/m) Ag sph.	1.0229	4.12	0.6106	13.175	40.0111 ± 0.4168	51.0925 ± 3.4547	34.75 ± 0.22	35.75 ± 0.13	72.72 ± 0.32	76.36 ± 0.27
1.0% (m/m) Ag tri.	1.0229	4.12	0.6096	18.903	43.0687 ± 0.3641	47.3165 ± 6.3033	33.39 ± 0.17	35.31 ± 0.22	70.28 ± 0.32	76.31 ± 0.18

Bibliography

[1] B. S. Glassman. Spray cooling for land, sea, air and space based applications, a fluid management system for multiple nozzle spray cooling and a guide to high heat flux heater design. Master's thesis, Department of Mechanical, Materials and Aerospace Engineering, University of Central Florida, 2005.

[2] I. Mudawar. Assessment of high-heat flux thermal management schemes. *IEEE Transactions on Components and Packaging Technologies*, 24(2):122–141, 2001.

[3] K. Azar. Advanced cooling concepts and their challenges. Advanced Thermal Solutions Inc., www.qats.com, 2002.

[4] K. N. Rainey, S. M. You, and S. Lee. Effect of pressure, subcooling and dissolved gas on pool boiling heat transfer from microporous, square pin-finned surfaces in FC-72. *International Journal of Heat and Mass Transfer*, 46:23–35, 2003a.

[5] M. R. Pais, L. C. Chow, and E. T. Mahefkey. Surface roughness and its effect on the heat transfer mechanism in spray cooling. *Journal of Heat Transfer*, 114:211–219, 1992.

[6] M. R. Overholt, A. McCandless, K. W. Kelly, C. J. Becnel, and S. Motakef. Micro-jet arrays for cooling of electronic equipment. *3rd International Conference on Microchannels and Minichannels*, Part B:249–252, 2005.

[7] Z. Yan. Spray cooling. *Two Phase Flow, Phase Change and Numerical Modeling*, 13:285–310, 2011.

[8] A. Bar-Cohen, G. Sherwood, M. Hodes, and G. Solbreken. Gas-assisted evaporative cooling of high density electronic modules. *IEEE Transactions on Components, Packaging and Manufacturing Technology*, 18 Part A(3):502–509, 1995.

[9] D. E. Tilton, C. L. Tilton, C. J. Moore, and R. E. Ackerman. Spray cooling for the 3-D cube computer. In *Intersociety Conference on Thermal Phenomena in Electronic Systems*, Washington, DC, USA, 1994.

[10] J. Yang, L. C. Chow, and M. R. Pais. Nucleate boiling heat transfer in spray cooling. *Journal of Heat Transfer*, 188:668–671, 1996.

[11] D. P. Rini, R. H. Chen, and L. C. Chow. Bubble behaviour and nucleate boiling heat transfer in saturated FC-72 spray cooling. *Journal of Heat Transfer*, 124:63–72, 2002.

[12] A. L. N. Moreira, A. S. Moita, and M. R. Panão. Advances and challenges in explaining fuel spray impingement: How much of a single droplet impact research is useful. *Progress in Energy and Combustion Science*, 36:554–580, 2010.

[13] A. S. Moita and A. L. N. Moreira. Drop impact onto cold and heated rigid surfaces: morphological comparisons, disintegration limits and secondary atomization. *International Journal of Heat and Fluid Flow*, 28(4):735–772, 2007.

[14] A. Moita. *Thermal and Fluid Dynamics of Droplet Wall Interaction*. PhD thesis, Department of Mechanical Engineering, Instituto Superior Técnico, Lisbon, 2009.

[15] C. Mundo, M. Sommerfeld, and C. Tropea. Droplet-wall collisions: experimental studies of the deformation and breakup process. *International Journal Multiphase flow*, 21(2):151–173, 1995.

[16] S. U. Choi and J. A. Eastman. Enhancing thermal conductivity of fluids with nanoparticles. Technical report, Argonne National Lab., IL (United States), 1995.

[17] J. C. Maxwell. *A Treatise on Electricity and Magnetism*. 1873.

[18] Y. Xuan and Q. Li. Heat transfer enhancement of nanofluids. *International Journal of Heat and Fluid Flow*, 21:58–64, 2000.

[19] H. S. Aybar, M. Sharifpur, M. R. Azizian, M. Mehrabi, and J. P. Meyer. A review of thermal conductivity models for nanofluids. *Heat Transfer Engineering*, 2015.

[20] S. Z. Heris, S. G. Etemad, and M. N. Esfahany. Experimental investigation of oxide nanofluids laminar flow convective heat transfer. *International Communications in Heat and Mass Transfer*, 33 (4):529–535, 2006.

[21] N. Putra, W. Roetzel, and S. K. Das. Natural convection of nano-fluids. *Heat and Mass Transfer*, 39(8-9):775–784, 2003.

[22] R. A. Taylor and P. E. Phelan. Pool boiling of nanofluids: Comprehensive review of existing data and limited new data. *International Journal of Heat and Mass Trasnfer*, 52:5339–5347, 2009.

[23] A. H. A. Al-Waeli, M. T. Chaichan, H. A. Kazem, and K. Sopian. Evaluation and analysis of nanofluid and surfactant impact on photovoltaic-thermal systems. *Case Studies in Thermal Engineering*, 13, 2019.

[24] Y. R. Sekhar, K. V. Sharma, R. T. Karupparaj, and C. Chiranjeevi. Heat transfer enhancement with Al_2O_3 nanofluids and twisted tapes in a pipe for solar thermal applications. *Procedia Engineering*, 64:1474–1484, 2013.

[25] D. K. Devendiran and V. A. Amirtham. A review on preparation, characterization, properties and applications of nanofluids. *Renewable and Sustainable Energy Reviews*, 60:21–40, 2016.

[26] R. Saidur, K. Y. Leong, and H. A. Mohammad. A review on applications and challenges of nanofluids. *Renewable and Sustainable Energy Reviews*, 15(3):1646–1668, 2011.

[27] R. H. Chen, T. Phuoc, and D. Martello. Effects of nanoparticles on nanofluid droplet evaporation. *International Journal of Heat and Mass Transfer*, 53:3677–3682, 2010.

[28] S. S. Hsieh, S. Y. Leu, and H. H. Liu. Spray cooling characteristics of nanofluids for electronic power devices. *Nanoscale Research Letters*, 10, 2015.

[29] S. V. Ravikumar, K. Haldar, J. M. Jha, S. Chakraborty, I. Sarkar, S. K. Pal, and S. Chakraborty. Heat transfer enhancement using air-atomized spray cooling with water-Al_2O_3 nanofluid. *International Journal of Thermal Sciences*, 96:85–93, 2015.

[30] R. Sankaralingam, F. Musthafa, S. Ismail, and V. Gopal. Experimental studies on premixed charge compression ignition (PCCI) engine using port injection of heated Diesel. *Journal of Engineering Science and Technology*, 13:3457–3472, 2018.

[31] V. Bertola. Introduction to fluid mechanics of liquid interfaces: Basic equations, Navier-Stokes equations for capillary flows, liquid jet break-up. In *Eighth International Advanced Course on Liquid Interfaces, Drops and Sprays (LIDESP)*, July 2020.

[32] J. Naber and P. Farrell. Hydrodynamics of droplet impingement on a heated surface. *AE Technical Paper*, 930919, 1993.

[33] R. Rioboo, M. Marengo, and C. Tropea. Outcomes from a drop impact on solid surfaces. *Atomization and Sprays*, 11:155–165, 2001.

[34] C. D. Stow and M. G. Hadfield. An experimental investigation of fluid flow resulting from the impact of a water drop with an unyielding dry surface. *Proceedings of the Royal Society London*, 373: 419–441, 1981.

[35] Z. Wu. *Modélisation et calcul implicite multidomaine d'écoulments diphasiques gas-gouttelettes*. PhD thesis, Univesité Pierre et Marie Curie, Paris, Francel, 1992.

[36] C. X. Bai and A. D. Gosman. Development of methodology for spray impingement simulation. In *SAE Technical Paper*. SAE International, 1995.

[37] M. Gavaises, A. Theodorakakos, and G. Bergeles. Modelling wall impaction of diesel sprays. *International Journal of Heat and Fluid Flow*, 17(2):130–138, 1992.

[38] L. Randy, G. V. Wall, G. M. Berger, and S. D. Mozes. The combined influence of a rough surface and thin fluid film upon the splashing threshold and splash dynamics of a droplet impacting onto them. *Experimental Fluids*, 40:23–32, 2006.

[39] I. V. Roisman, K. Horvat, and C. Tropea. Spray impact: rim transverse instability initiating fingering and splash, and description of a secondary spray. *Physics of Fluids*, 18(10):102104, 2006.

[40] D. Ribeiro, A. Silva, and M. Panão. Insights into single droplet impact models upon liquid films using alternative fuels for aero-engines. *Applied Sciences*, 10, 2020.

[41] R. L. V. Wal, G. M. Berger, and S. D. Mozes. The splash/non-splash boundary upon a dry surface and thin fluid film. *Experiments in fluids*, 40:53–59, 2006.

[42] R. Mesler and G. Mailen. Nucleate boiling in thin liquid films. *AIChE Journal*, 23:954–957, 1977.

[43] R. Zhao, W. I. Cheng, Q. N. Liu, and H. I. Fan. Study on heat transfer performance of spray cooling: model and analysis. *Heat and Mass Transfer*, 46:821–829, 2010.

[44] W. L. Cheng, F. Y. Han, Q. N. Liu, and H. L. Fan. Spray characteristics and spray cooling heat transfer in the non-boiling regime. *Energy*, 36:3399–3405, 2011.

[45] W. L. Cheng, W. W. Zhang, and L. Hu. Spray cooling and flash evaporation cooling: The current development and application. *Renewable and Sustainable Energy Reviews*, 55:614–628, 2016.

[46] S. S. Hsieh, T. C. Fan, and H. H. Thai. Spray cooling characteristics of water and R-134a. Part I: nucleate boiling. *International Journal of Heat and Mass Transfer*, 47:5703–5712, 2004.

[47] S. S. Hsieh, T. C. Fan, and H. H. Thai. Spray cooling characteristics of water and R-134a. Part II: transient regime. *International Journal of Heat and Mass Transfer*, 47:5713–5724, 2004.

[48] L. Lin and R. Ponnappan. Heat transfer characteristics of spray cooling in a closed loop. *International Journal of Heat and Mass Transfer*, 46:3737–3746, 2003.

[49] M. Visaria and I. Mudawar. Effects of high subcooling on two-phase spray cooling and critical heat flux. *International Journal of Heat and Mass Transfer*, 51:5269–5278, 2008.

[50] M. Visaria and I. Mudawar. Application of two-phase spray cooling for thermal management of electronic devices. *IEEE Transactions on Components and Packaging Technologies*, 32:784–793, 2009.

[51] Babita, S. K. Sharma, and S. M. Gupta. Preparation and evaluation of stable nanofluids for heat transfer application: A review. *Experimental Thermal and Fluid Science*, 79:202–212, 2016.

[52] K. V. Sharma, P. K. Sarma, W. H. Azmi, R. Mamat, and K. Kadirgama. Correlations to predict friction and forced convection heat transfer coefficients of water based nanofluids for turbulent flow in a tube. *The International Journal of Microscale and Nanoscale Thermal and Fluid Transport*, 3 (4), 2012.

[53] F. J. Wasp. Solid-liquid flow slurry pipeline transportation. *Trans. Tech. Publications*, 1977.

[54] R. L. Hamilton and O. K. Crosser. Thermal conductivity of heterogeneous two-component systems. *Industrial Engineering Chemistry Fundamentals*, 1:182–191, 1962.

[55] W. H. Qi, M. P. Wang, and Q. H. Liu. Shape factor of non-spherical nanoparticles. *Journal of Materials Science*, 40:2737–2739, 2005.

[56] M. Figueiredo. Nanofluid spray cooling characterization combining phase doppler anemometry with high-speed visualization and thermography. Master's thesis, Instituto Superior Técnico, University of Lisbon, 2020.

[57] P. Pontes. Thermographical analysis of interface heat transfer mechanisms, with high temporal resolution. Master's thesis, Instituto Superior Técnico, University of Lisbon, 2016.

[58] C. Y. Ho and T. K. Chu. Electrical resistivity and thermal conductivity of nice selected AISI Stainless Steels. Prepared by Center for Information and Numerical Data Analysis and Synthesis, Purdue University, 1977.

[59] W. H. McAdams. *Heat Transmission*, chapter 7. McGraw-Hill, New York, 3^{rd} edition, 1954.

[60] R. J. Goldstein, E. M. Sparrow, and D. C. Jones. Natural convection mass transfer adjacent to horizontal plates. *International Journal of Heat and Mass Transfer*, 16(5):1025–1035, 1973.

[61] J. R. Lloyd and W. R. Moran. Natural convection adjacent to horizontal surfaces of various planforms. *ASME Paper*, 74-WA/HT-66, 1974.

[62] A. Sielaff. *Experimental Investigation of Single Bubbles and Bubble Interactions in Nucleate Boiling*. PhD thesis, Technische Universität Darmstadt, 2014.

[63] F. P. Incropera, D. P. DeWitt, T. L. Bergman, and A. S. Lavine. *Fundamentals of Heat and Mass Transfer*. Wiley, 6^{th} edition, 2007.

[64] M. Palmer. Propagation of uncertainty through mathematical operations. http://web.mit.edu/fluids-modules/www/exper_techniques/2.Propagation_of_Uncertaint.pdf.

[65] M. A. Farooque and J. S. Rohankar. Survey on various noises and techniques for denoising the color image. *International Journal of Application or Innovation in Engineering and Management*, 2: 217–221, 2013.

[66] R. Vardasca, J. Gabriel, P. Plassmann, and F. Ring. Comparison of different image enhancing techniques for medical thermal images. *Journal of Medical Imaging and Health Informatics*, 5, 2015.

[67] M. Malý, A. S. Moita, J. Jedelsky, A. P. C. Ribeiro, and A. L. N. Moreira. Effect of nanoparticle concentration on the characteristics of nanofluid sprays for cooling applications. *Journal of Thermal Analysis and Calorimetry*, pages 1–12, 2018.

[68] J. S. Suh, D. P. DiLella, and M. Moskovits. Surface-enhanced raman spectroscopy of colloidal metal systems: a two-dimensional phase equilibrium in p-aminobenzoic acid adsorbed on silver. *Journal of Physical Chemistry*, 87:1540–1544, 1983.

[69] J. A. Creighton, C. G. Blatchford, and M. G. Albrecht. Plasma resonance enhancement of Raman scattering by pyridine adsorbed on silver or gold sol particles of size comparable to the excitation wavelength. *Journal of the Chemical Society Faraday Transactions II*, 75:790–798, 1979.

[70] Attension. *THETA optical tensiometer manual*.

[71] Xenics Infrared Solutions. *Xenics' Onca-MWIR-InSb-320 documentation*. Available at: https://pdf.directindustry.com/pdf/xenics/onca-mwir-insb-320/54398-176770.html.

Appendix A

High-speed camera setup and recording

A.1 Introduction

In this appendix, an overview of the setup and recording procedures of the *Vision Research Phantom v4.2* high-speed camera is given. The name of the camera software is *Phantom 640*.

A.2 Setup

A.2.1 Hardware setup

To use the high-speed camera, two cables should be connected to it: the power supply cable and the data cable. The data cable should be connected to the acquisition computer. The camera turns on immediately after connecting the power cable.

A.2.2 Software setup

1. Open the *Phantom 640* software;
2. Go to Acquisition, Setup & recording;
3. Set the *Acquisition rate* (in FPS);
4. Set the number of frames to be recorded after the *Trigger*;
5. Set the Exposure time and EDR exposure to 10 µs;
6. Select the image size depending on the vertical distance between the nozzle and the test surface:
    a. If vertical distance 10 mm, use 512×256 px.
    b. If vertical distance 20 mm, use 512×384 px.

7. Now the camera setup is complete.

A.3 Recording

1. When ready to record, click on *Capture*;
2. Click on *Trigger* to start recording the frames of interest.

A.4 Saving results

When the recording has ended, click *Ok*. A new window will open. Select frame zero and click on *Mark begin*. When ready, press *Ok* and choose the name of the file to be saved. The video will be saved in *.cin* format. The video should then be exported using the steps presented in Section A.5.

A.5 Exporting the results to *.avi* format

The videos can be exported to *.avi* format by going to the *Phantom 640* software and then on the file *File* tab click on *Convert .cin to...*. A new dialog will open where the *.cin* files to be exported can be selected.

Appendix B

Thermographic camera setup and recording

B.1 Introduction

In this appendix, an overview of the setup and recording procedures of the *Xenics' Onca-MWIR-InSb-320* thermographic camera is given. The name of the camera software is *Xeneth64*.

B.2 Camera properties

Table B.1: *Xenics' Onca-MWIR-InSb-320* thermographic camera properties (Xenics Infrared Solutions [71]).

Camera characteristics		Optical system		Image characteristics	
Sensor	InSb (MWIR)	Focal lens	13 mm	Video rate	60 Hz
Spectral sensibility	3,5 – 5 µs	Optics material	Germanium	Max FPS	3000 fps
Spatial resolution	320 $\times$ 256 px			Min pixels (ROI)	15 $\times$ 5 px
Thermal sensibility	$<$ 17 mk			Exposition	$>$ 1 µs

B.3 Setup

B.3.1 Hardware setup

To use the thermographic camera, two cables should be connected to it: the power supply cable and the data cable. The data cable should be connected to the acquisition computer. The camera turns on immediately after connecting the power supply cable. After connecting the power supply cable the camera fan turns on to cool the sensor. The fan spins fast until the sensor is at the correct temperature. Only then it is possible to setup the camera software.

B.3.2 Software setup

1. Open the *Xeneth64* software;
2. Select *1009-TrueNuc-FilterD* calibration data;
3. Focus on the area of interest;
4. Go to *Settings* and set the integration time to 200 us;
5. Right-click over *Maximize FPS* and then click on *Unlock property*;
6. Set maximum FPS to 40.
7. Put the black card over the camera lens;
8. Go to *Calibration* and then *Calibrate camera*;
9. In the menu select: *Recalibrate offset*;
10. Set the following values: 100, 300%, 300%;
11. Select *Filter D*;
12. Press the button to calibrate;
    a. If *Averaging frame...* message appears, press *Finish*, *Not save* and continue to step 12.
    b. Else, repeat step 11.
13. Under the *Recording* tab, write the path and name of the file to be recorded;
14. Set the number of frames to be recorded;
15. When ready to record, select *Minimize CPU usage* in the *Recording* tab;
16. Now the camera setup is complete.

B.4 Recording

To start the recording press on *Record*. The green progress bar will show the current status of the recording.

B.5 Saving results

The videos are automatically saved in *.xvi* format, with the chosen name and in the selected path. These videos should then be converted to *.avi* using the procedure presented in Section B.6.

B.6 Exporting the results to *.avi* format

To convert a *.xvi* file to *.avi*, double click on the *.xvi* file. Select the range of frames to be exported. Under the *View* file, select *Scale*. Now the ADU scale will be displayed on the right side. Set the colormap to *8bit grayscale*. Select the range of ADU to be used. Take note of the ADU scale and FPS. When ready, press *Export*. Choose a name for the video and press *Ok*.

Appendix C

MATLAB code

C.1 Introduction

The purpose of this MATLAB code is to process the thermographic videos, which were exported using the procedure presented in Appendix B. At first, the Analog to Digital unit (ADU) scale must be converted to temperatures. Then the background is removed and a Gaussian filter is applied to each frame. Finally, the temporal evolution of the dissipated heat flux is computed. The original code was developed Pontes [57], but some improvements have been made.

The code is divided in a main script (`thermoScript.m`), where input variables are defined, and three sub-scripts. The results of each sub-script is saved in a `.mat` variable. The three sub-scripts are:

- `ADUtoTemp.m` – Convert ADU scale to temperature in $^{\circ}\mathrm{C}$. The calibration obtained by Pontes [57] is applied to each pixel and temperatures obtained by applying the Stefan-Boltzmann law, Equation 3.12;

- `backgroundAndFilter.m` – Remove frame background and apply Gaussian noise filter. The background is removed by function `backgroundRemoval.m`. For the transient regime video, `*_t.avi`, the background is estimated from the first frame of the video. For the steady-state regime video, `*_e.avi`, the background is estimated from the first frame of the initial video, `*_i.avi`. Thereafter, a Gaussian filter with standard deviation 2 and 9×9 kernel is applied;

- `heatfluxCalculation.m` – Calculate temporal evolution of dissipated heat power and heat flux, in W and $\mathrm{W/m^2}$, respectively. Pixel energy balances are performed, from where the dissipated power is calculated.

C.2 Inputs

Table C.1: Thermographic camera video post-processing MATLAB script inputs.

Variable	Format	Unit
Videos .avi	For each test, should be three .avi files: steady-state (`*_e.avi`), transient (`*_t.avi`) and initial (`*_i.avi`).	–
Center of area of interest	Insert values in `thermoScript.m`.	pixel
Radius of area of interest	Insert value in `thermoScript.m`.	pixel
Ambient temperature	Insert value in `thermoScript.m`.	°C
Current	Insert values in `thermoScript.m`.	A
Estimated emissivity	Insert value in `thermoScript.m`.	–
ADU scale	Two column matrix, first column is ADU minimum and second column is maximum, saved as `ADUscale.mat`.	–
FPS	Column array saved as `videoFPS.mat`.	s^{-1}
Pixel scale	Insert value in `thermoScript.m`.	m/pixel
Specific heat capacity	Insert value in `thermoScript.m`.	J/(kg.K)
Area	Insert value in `thermoScript.m`.	m^2
Thickness	Insert value in `thermoScript.m`.	m
Density	Insert value in `thermoScript.m`.	kg/m^3

C.3 Code

C.3.1 thermoScript.m

```
% thermoScript.m
%
% Thermographic camera video post-processing script.
%
% Developed by: Miguel Sanches (miguel.sanches@tecnico.ulisboa.pt)
% September 2020
% Calibration credits: Pedro Pontes (November 2016)

%% Inputs
clear;clc;
% -> Write ADU scale and FPS in the correct .mat files

% -> Interest area center and radius
center = [160,135];
radius = 90;

% -> Ambient temperature [ C ]
Tamb = 26.7;

% -> Current [A]
I = [15];
```

```
% -> Material and sheet properties
e = 0.96; % Estimated emissivity
cp = 477; % Specific heat capacity [J.kg-1.K-1]
th = 20*10^-6; % Thickness [m]
rho = 7880; % Density [kg.m-3]
area = (0.06*0.09); % Area [m^2]

% -> Pixel scale [m/px]
dx = (50/230)*10^(-3);

%% 1   Convert ADU to temperature
ADUtoTemp;

%% 2   Remove background and filter video
backgroundAndFilter;

%% 3   Get heatfluxes
heatfluxCalculation;
```

C.3.2 ADUtoTemp.m script and associated calibration.m function

```
%% ADUtoTemp.m
% Convert ADU values to temperature in  C.
% Save a .mat file with temperature video in  C.
%
% Developed by: Miguel Sanches (September 2020).
% Calibration credits: Pedro Pontes (November 2016).

%% Script
load ADUscale
files = dir(fullfile('*.avi'));

for k = 1:size(files,1)
    ADUmin = ADUscale(k, 1);
    ADUmax = ADUscale(k, 2);

    videoObj = VideoReader(files(k).name);
    vid = read(videoObj);

    frames = videoObj.NumberOfFrames;

    for i = 1:frames
        videoMat(:,:,i) = im2double(vid(:,:,1,i))*(ADUmax-ADUmin)+ADUmin;
    end

    % Apply calibration
```

```
    videoMat = calibration(videoMat, Tamb, e);

    save(strcat(files(k).name, '.mat'), 'videoMat', 'ADUmin', 'ADUmax', 'e', 'Tamb')

    clear videoMat frames vid vidObj
end
```

```
function videoMat = calibration(videoMat, Tamb, e)
%% calibration.m
% Apply calibration developed by Pedro Pontes (November 2016).
% Find, for each value of ADU, the corresponding temperature in  C.
%
% Developed by: Miguel Sanches (September 2020).
% Calibration credits: Pedro Pontes (November 2016).
%% Inputs:
% -> videoMat -> 3D matrix of ADU values.
% -> Tamb -> Ambient temperature in  C.
% -> e -> Estimated emissivity.
%
%% Outputs:
% -> videoMat -> 3D matrix with temperature values in  C.
%
%% Convert ADU to temperature [in  C ]
x = 600; % Initialization

for t = 1:size(videoMat, 3) % Frames
    for j = 1:size(videoMat, 2) % y direction
        for i = 1:size(videoMat, 1) % x direction
            ADU = videoMat(i,j,t);
            if ADU < 1000 % Exclude dead pixels
                videoMat(i,j,t) = 450;
            else
                % Find Wtot for the ADU value of each pixel
                r = roots([-1.4901E-6 8.4705E-3 -3.268533 1574.11-ADU]);
                l = 1;
                % Filter solutions
                while l < 4
                    fi = r(l);
                    if fi ≥ 300 && fi ≤ 2500
                        Wtot = fi;
                    end
                    l = l+1;
                end
            end
            % Calculate temperature
            videoMat(i,j,t) = (nthroot((Wtot/5.67E-8-0.05*(Tamb+273)^4)/e,4)-273);
        end
    end
```

```
    fprintf('ADUtoTemp || %i of %i \n', t, size(videoMat, 3))
end
```

C.3.3 backgroundAndFilter.m script and associated backgroundRemoval.m function

```
%% backgroundAndFilter.m
% Remove background and filter video.
% Save a .mat file with treated video.
%
% Developed by: Miguel Sanches (September 2020).

%% Script
clearvars -except center radius I Tamb e cp k th rho area dx

files_e = dir(fullfile('*_e.avi.mat'));
files_t = dir(fullfile('*_t.avi.mat'));
files_i = dir(fullfile('*_i.avi.mat'));

% Treat steady-state regime videos
for k = 1:size(files_e,1)
    % Get frame from before heating video to be used to compute background
    load(files_i(k).name)
    avbackground = videoMat(:,:,1);

    clear ADUmax ADUmin frames videoMat

    load(files_e(k).name)
    noBackgroundVideo = backgroundRemoval(videoMat, avbackground, center, radius);
    for t = 1:size(noBackgroundVideo, 3)
        % Apply Gaussian filter with sigma = 2
        finalVideo(:,:,t) = imgaussfilt(noBackgroundVideo(:,:,t), 2);
        fprintf('Filter || %i of %i \n', t, size(noBackgroundVideo, 3))
    end

    save(strcat(files_e(k).name, '_final.mat'), 'finalVideo')

    clear finalVideo noBackgroundVideo
end

% Treat transient regime videos
for k = 1:size(files_t,1)
    load(files_t(k).name)
    % Get first frame of transient regime video to compute background
    avbackground = videoMat(:,:,1);
```

```
    noBackgroundVideo = backgroundRemoval(videoMat, avbackground, center, radius);
    for t = 1:frames
        % Apply Gaussian filter with sigma = 2
        finalVideo(:,:,t) = imgaussfilt(noBackgroundVideo(:,:,t), 2);
        fprintf('Filter || %i of %i \n', t, size(noBackgroundVideo, 3))
    end

    save(strcat(files_t(k).name, '_final.mat'), 'finalVideo')

    clear finalVideo noBackgroundVideo
end
```

```
function finalVideo = backgroundRemoval(videoMat, background, center, radius)
%% backgroundRemoval.m
% Remove frame background.
%
% Developed by: Miguel Sanches (September 2020).
%% Inputs:
% -> video -> 3D matrix with temperature values in  C.
% -> background -> Frame where background will be computed.
% -> center -> Center x and y coordinates of area of interest.
% -> radius -> Radius of area of interest.
%
%% Outputs:
% -> finalVideo -> Video without background.

%% Calculate mean temperature of area of interest
 n = 1;
 backTemperature = 0;
for i = 1:length(videoMat(:,1,1))
    for k = 1:length(videoMat(1,:,1))
        if ((center(1,2)-i)^2+(center(1,1)-k)^2 <= radius^2)
            backTemperature = backTemperature+videoMat(i,k,1);
            n = n+1;
        end
    end
end
backTemperature=backTemperature/n;

%% Calculate and remove background
for t = 1:size(videoMat,3)
    for x = 1:size(videoMat,1)
        for y = 1:size(videoMat,2)
            finalVideo(x,y,t) = ...
                backTemperature-(background(x,y)-videoMat(x,y,t))/background(x,y)*backTemperature;
        end
    end
end
```

C.3.4 heatfluxCalculation.m script and associated heatflux.m function

```
%% heatfluxCalculation.m
% Calculate dissipated heat flux in the area of interest.
% Save a .mat file with the results.
%
% Developed by: Miguel Sanches (September 2020).
% Original code developed by: Pedro Pontes (November 2016).

%% Script
files = dir(fullfile('*_final.mat'));
load videoFPS

for i = 1:size(files,1)
    load(files(i).name)

    [interestArea, dissFlux, space, time, q, qin] = heatflux(finalVideo, videoFPS(i), ...
        I(i), center, radius, cp, th, rho, area, dx);

    I_i = I(i);
    fr_i = videoFPS(i);

    dissFlux_smooth = smooth(dissFlux(2:length(dissFlux)-2), 0.1, 'rloess');
    mean_dissFlux_smooth = mean(dissFlux_smooth);
    std_dissFlux_smooth = std(dissFlux_smooth);

    save(strcat(files(i).name,'_hf.mat'),'interestArea', 'dissFlux', 'dissFlux_smooth', ...
        'mean_dissFlux_smooth', 'std_dissFlux_smooth', 'fr_i', 'I_i', 'finalVideo', 'q')

    clear interestArea dissFlux dissFlux_smooth mean_dissFlux_smooth std_dissFlux_smooth ...
        finalVideo space time q qin
end
```

```
function [interestArea, dissFlux, space, time, q, qin] = heatflux(mat, fr, I, center, ...
    radius, cp, th, rho, area, dx)
%% heatflux.m
% Calculate dissipated heat flux in [W/m^2] by applying an energy balance.
%
% Developed by: Miguel Sanches (September 2020).
% Original code developed by: Pedro Pontes (November 2016).
%% Inputs:
% -> mat -> Thermographic video.
% -> fr -> FPS.
```

```
% -> I -> Current [A].
% -> center -> Center of the interest area.
% -> radius -> Radius of the interest area.
% -> cp -> Specific heat capacity [J.kg-1.K].
% -> th -> Thickness [m].
% -> rho -> Density [kg.m-3].
% -> area -> Area [m^2].
% -> dx -> Pixel scale [m/px].
%
%% Outputs:
% -> interestArea -> Temperatures of the area of interest, else is NaN.
% -> dissFlux -> Temporal evolution of the dissipated heat flux [W/m^2].
% -> space -> Space contribution to dissipated heat flux [W/m^2].
% -> time -> Transient contribution to dissipated heat flux [W/m^2].
% -> q -> Spatial dissipated heat flux maps [W/m^2].
% -> qin -> Spatial input heat flux maps [W/m^2].
%
%% Variable initialization

% Get size of the video (1 - pixels in x direction, 2 - pixels in y direction, 3 - number ...
    of frames)
videoSize = size(mat);

% Matrix space alocation
q = zeros(videoSize);
space = zeros(videoSize);
time = zeros(videoSize);

% Time scale
dt = 1/fr; % [s]

%% Calculate mean temperature in area of interest
for t = 1:videoSize(3)
    for i = 1:videoSize(1)
        for j = 1:videoSize(2)
            if (j-center(1))^2+(i-center(2))^2 > radius^2
                interestArea_T(i,j,t) = NaN;
            else
                interestArea_T(i,j,t) = mat(i,j,t);
            end
        end
    end
    mean_T(t) = nanmean(nanmean(interestArea_T(:,:,t)));
end

%% Coeficients for linear approximation to the derivative. (upwind second order approximation)
a1 = 0;         %-2
a2 = -1;        %-1
a3 = 1;         %0
```

```
a4 = 0;         %+1
a5 = 0;         %+2

%% Calculate heat flux
for t = 1:videoSize(3)-2
    % Determine thermal conductivity of the sheet using mean temperature
    k = 0.0171*mean_T(t)+14.425; % [W/(m.K)]
    % Determine resistance of the sheet using mean temperature
    r = 2*10^(-5)*mean_T(t)+0.0477; % [ohm]
    % Determine input heat
    qi = r*I^2/area; % [W.m-2]
    for x = 1:videoSize(1)-2
        for y = 1:videoSize(2)-2
            qin(x,y,t) = qi;
            if t == 1
                A1 = 0; A2 = 0; A3 = mat(x,y,t)*a3; A4 = mat(x,y,t+1)*a4; A5 = ...
                    mat(x,y,t+2)*a5;
            elseif t == 2
                A1 = 0; A2 = mat(x,y,t-1)*a2; A3 = mat(x,y,t)*a3 ;A4 = mat(x,y,t+1)*a4; A5 ...
                    = mat(x,y,t+2)*a5;
            else
                A1 = mat(x,y,t-2)*a1; A2 = mat(x,y,t-1)*a2; A3 = mat(x,y,t)*a3; A4 = ...
                    mat(x,y,t+1)*a4; A5 = mat(x,y,t+2)*a5;
            end
            if t == 1
                q(x,y,t) = 0;
            elseif x == 1 || y == 1
                q(x,y,t) = qi-rho*cp*th*(A1+A2+A3+A4)/dt;
            elseif x == 2 || y == 2
                q(x,y,t) = qi-rho*cp*th*(A1+A2+A3+A4)/dt;
            else
                space(x,y,t) = k*th*(mat(x-1,y,t)-2*mat(x,y,t)+mat(x+1,y,t)+...
                    mat(x,y-1,t)-2*mat(x,y,t)+mat(x,y+1,t))/dx^2;
                time(x,y,t) = -rho*cp*th*(A1+A2+A3+A4)/dt;
                q(x,y,t) = qi+time(x,y,t)+space(x,y,t);
            end
        end
    end
end

%% Restraining to the wanted circular area
for t = 1:videoSize(3)
    for i = 1:videoSize(1)
        for j = 1:videoSize(2)
            if (j-center(1))^2+(i-center(2))^2 > radius^2
                interestArea(i,j,t) = 0;
            else
                interestArea(i,j,t) = q(i,j,t);
            end
```

```
        end
    end
end

%% Calculate dissipated power [W] and heat flux [W/m^2]
dissPower(:) = trapz(trapz(interestArea));
dissPower = dissPower(:)'*dx^2;
dissFlux = dissPower/(pi()*(radius*dx)^2);
```

Appendix D

Preparation of the specimen

D.1 Introduction

In this appendix, the methodology of preparation of the specimen is presented.

D.2 Support for the metallic foil

The support for the metallic foil was designed by Figueiredo [56]. It serves two purposes:

- Secure the metallic foil in place;
- Collect the used fluid and direct it to the collector tube.

The support has two main parts: an aluminium plate where the metallic foil is fixed, Figure D.1, and a steel support where the plate is fixed with screws, Figure D.2. Both parts have a $50\ \mathrm{mm}$ hole in the center, under which the thermographic camera lens is placed. The foil support has a smaller threaded hole, where the fluid collector tube is connected.

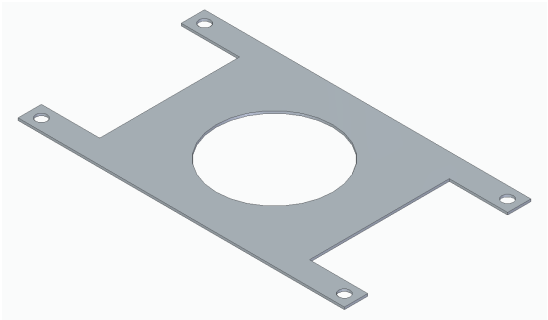

Figure D.1: Foil support plate.

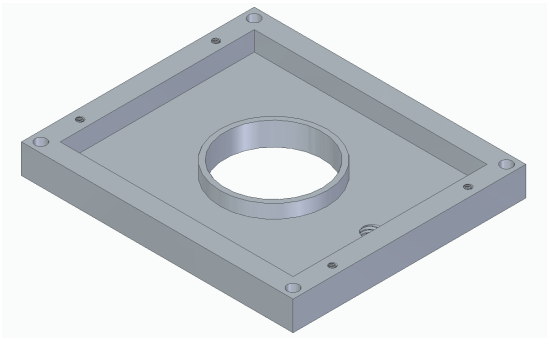

Figure D.2: Foil support.

D.3 Preparation of AISI 304 stainless steel specimen

1. Both sides of the metallic foil support (Figure D.1) were painted using high-temperature black spray paint;
2. A rectangle of 80×90 mm of 1 mm thick rubber was cut;
3. In the center of the rubber rectangle, a circle of 50 mm in diameter was cut;
4. The rubber was glued to the metallic support using high-temperature resistant silicone;
5. A rectangle of 60×90 mm of AISI 304 stainless steel was cut;
6. The electrical contacts were welded to each side of the AISI 304 stainless steel rectangle, using 60% tin/38% lead/2% copper (with SW32 flux) weld, as suggested in Figure D.3;
7. The AISI 304 stainless steel rectangle was fixed to the metallic support using tape;
8. The bottom side of the AISI 304 stainless steel rectangle was painted using high-temperature black spray paint, Figure D.4.

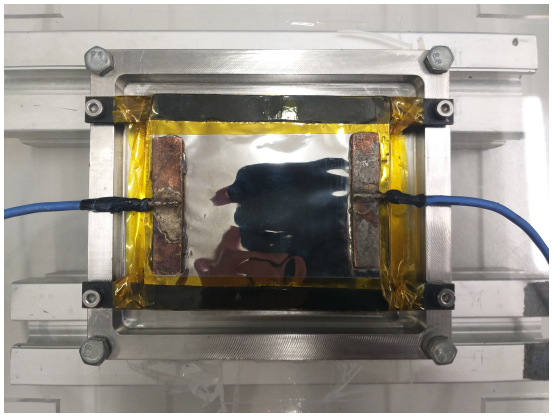

Figure D.3: Top view of the metallic foil support.

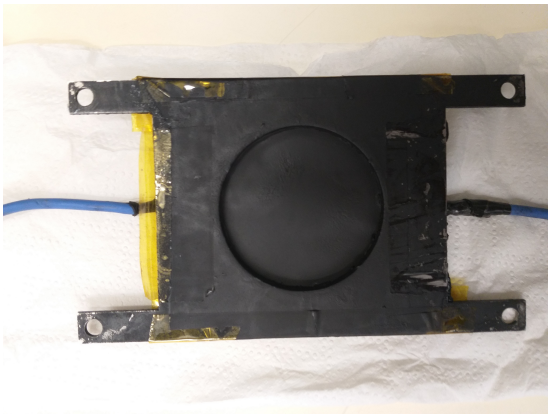

Figure D.4: Bottom view of the metallic foil support.